MICROSTRUCTURAL INSTABILITIES IN NICKEL-BASED SINGLE CRYSTAL SUPERALLOYS

A Dissertation

by

HARIKRISHNAN RAJENDRAN

Submitted to the Office of Graduate and Professional Studies of
Texas A&M University
in partial fulfillment of the requirements for the degree of

DOCTOR OF PHILOSOPHY

Chair of Committee,	Jean-Briac le Graverend
Committee Members,	Amine Benzerga
	Alan Needleman
	Ibrahim Karaman
Head of Department,	Srinivas Rao Vadali

May 2021

Major Subject: Aerospace Engineering

ABSTRACT

Single crystal superalloys, mostly Nickel-based, have been, so far, the material of choice for high-temperature applications, such as gas turbine blades. Single crystalline turbine blades are usually cast in the $<001>$ direction, providing the best combination of properties. While misorientations up to 15° are within accepted tolerance, the elastic/viscoplastic response of the bi-phased $\gamma/\gamma^{'}$ microstructure in superalloys is highly sensitive towards the crystalline orientation. Further, multiaxial stress states create microstructural gradients and alter the performance of the material. As the microstructure stability dictates the blade's structural integrity, it is necessary to understand the microstructural state as a function of the crystallographic orientation and multiaxial stress state to quantify the creep performance.

The lifetime of Ni-based single crystal superalloys is connected to the integrity of the strengthening phase, $\gamma^{'}$. During high-temperature thermomechanical loading, the cuboidal shaped $\gamma^{'}$ phase coalesces, directionally coarsens(rafting), and is finally topologically inverted, viz. surrounds the γ phase and acts as the matrix. The topological inversion comes along with an increase in the plastic strain rate known as the tertiary creep. X-ray tomography experiment has recently revealed that the tertiary creep initiates before the expected increase in the volume fraction of pores. Thus, the initiation of the tertiary creep stage might also be due to the destabilization of the $\gamma/\gamma^{'}$ interfacial dislocation network leading to the massive shearing of $\gamma^{'}$ rafts concomitantly resulting in topological inversion. Simultaneously, the strain-hardening and the void growth in these viscoplastic single crystals lead to the ductile fracture. Hence, for a fundamental understanding of the microstructural instability and to improve lifetime predictions, it is necessary to consider the interplay of orientation-specific microstructural evolutions, the destabilization of the interfacial network, and subsequent shearing of $\gamma^{'}$ particles, as well as dislocation, creep and void growth to fully explain what triggers the increase of the plastic strain rate in the tertiary creep stage leading to failure.

This dissertation aims to elucidate the microstructural instabilities in Ni-based single crystal superalloys through a multi-scale microstructure-sensitive thermo-mechanically coupled damage model in a finite-element crystal plasticity framework through the integration of high-temperature multiaxial creep experiments, advanced characterization techniques, and high fidelity computational tools. To that end, a phase-field model was extended to account for microstructural destabilization and damage. For the first time, topological inversion during creep was predicted using a phase-field model. Further, macroscale finite-element calculations were carried out using the realistic 3D microstructures derived from the phase-field model. A viscoplastic description of 3D rafting predicted the channel evolution irrespective of the loading conditions and crystallographic orientation. Results from this work will elucidate the effects of microstructural degradation, crystallography, and multiaxial stresses towards rupture in Ni-based single crystal superalloy subjected to high-temperature/low stress creep conditions.

ACKNOWLEDGMENTS

First and foremost, I would like to thank my advisor, Dr. Jean-Briac le Graverend, and the Department of Aerospace Engineering, Texas A&M University, for offering me the opportunity to work on a very exciting research topic. My advisor gave me the freedom to define the problem statements and work independently to develop various numerical models used in this dissertation. I am thankful for the financial support I received from AFOSR and the Department of Aerospace Engineering.

I am most grateful to Dr. Vaitla Laxman for opening a world of possibilities through his motivation. I express my deepest gratitude to my research advisors at IIT Kanpur, Drs. P.M. Mohite, and C.S. Upadhyay, for instilling in me an aptitude for research and encouraging me to pursue a doctoral study.

Next, I would like to thank Dr. Amine Benzerga, Dr. Ibrahim Karaman, and Dr. Alan Needleman for agreeing to be a part of my dissertation committee and for the support of my Ph.D. candidature. I am humbled to have exemplary leaders like them in my committee, and their valuable comments helped fine-tune the scope of my research objectives. I am also very fortunate to get trained very early on, thanks to Dr. Benzerga, in critically analyzing journal articles and participate in the peer-review process, which later helped write this dissertation and journal articles.

The advanced coursework from both Texas A&M University and IIT Kanpur helped me immensely in deriving the theoretical formulations used in this work. I have taken multiple courses offered by Dr. Benzerga that were helpful and gave clarity to the damage modeling approach. I was fortunate to be selected for the summer workshop at Okinawa Institute of Science and Technology (OIST), Japan, which gave me the first theoretical exposure to phase-field modeling. I also thank Drs. Ingo Steinbach and Oleg Shchyglo (Ruhr University Bochum) for the *OpenPhase* phase-field solvers. I thank Dr. George Pharr for the opportunity to participate in the NSF NanoCamp. The encouragement from Dr. Lagoudas and his group during our occasional group meetings and project

presentations helped build confidence. I thank Dr. Lagoudas for giving me the opportunity to pitch my idea that later went on to became a fruitful collaboration.

I very much appreciate the care and advice from the graduate advisors, especially Gail Rowe, throughout this study. Special thanks to Dr. Moble Benedict and Rincy for the encouraging discussions. I also want to thank profusely for the timely help received from Dr. Lisa Perez in setting up the libraries and helping me install the numerical codes in the HPRC.

The most challenging yet fulfilling experience in this dissertation was performing high-temperature creep experiments. I enjoyed the time working closely with my colleagues, Seungyun, and Pawan. I am very thankful for the time and effort Pawan and Seungyun had invested in troubleshooting problems whenever we run into issues with the experimental set-up. I also acknowledge Mr. Rodney Inmon, who helped us with his practical suggestions. I had fruitful discussions with Ph.D. students who I met at EuroSuperalloys and TMS conferences. Among them, I want to particularly thank Caspar Schwalbe (University of Cambridge, UK) and Satoshi Utada (ENSMA, France) for taking time out to discuss and provide suggestions to some of the issues with the creep testing.

Souls close to my heart needs no mention. I want to thank all my friends for their kindness and for going out of the way to support me during challenging times. My close friends in Texas A&M have made life so much easier, and my stay at College Station very memorable. I owe all my success to my loving family. It is a privilege for me to thank everyone who supported and inspired me to contribute a small drop to science in the form of this dissertation. It has been a rewarding experience and a step towards my journey of obliterating the boundaries of my limited identities.

CONTRIBUTORS AND FUNDING SOURCES

Contributors

This work was supported by a dissertation committee consisting of Professor Jean-Briac le Graverend (advisor) and Professor Amine Benzerga of the Department of Aerospace Engineering and Professor(s) Ibrahim Karaman and Alan Needleman of the Department of Material Science and Engineering.

The Finite-Element Crystal Plasticity codes used in this work were calibrated by Professor le Graverend. The numerical simulations were performed using the computing resources from the Laboratory for Molecular Simulation (LMS) and High-Performance Research Computing (HPRC) at Texas A&M University.

The scanning electron microscopy images of MC2 and CMSX-4 used in this work were generously provided by Professor Jonathan Cormier (Institut Pprime, France) and Dr. Adriana Mattiello (Institut Pprime, France). These images were used in Chapters 3 and 5. Mr. Seungyun Lee contributed to the implementation of the high-temperature creep-bench experimental setup. Mr. Pawan Chaugule assisted in the creep testing of MC2 single crystal superalloys.

All other work conducted for the dissertation was completed by the student independently under the supervision of Professor le Graverend.

Funding Sources

Graduate study and research was supported through a AFOSR YIP grant FA9550-17-1-0233.

TABLE OF CONTENTS

Page

LIST OF FIGURES

FIGURE Page

LIST OF TABLES

TABLE Page

1. INTRODUCTION

1.1 Microstructural Instabilities in Ni-based single crystal superalloys: An overview

High-pressure turbine blades are the most critical component of an aero-engine that aides in the most sophisticated and intricate energy-conversion process. The highly compressed hot gases from the combustion chamber expand through the turbine, thereby exerting an aerodynamic force that rotates the blades. The turbine blades, in turn, drives the compressor, thereby drawing more pressurized air into the combustion section. Turbine blades are, therefore, incredibly critical to the safe-operation of aero-engines while being subjected to the peak of material limits: temperatures close to the melting point; prolonged multi-axial stresses due to blade curvature; isothermal and non-isothermal thermo-mechanical loading; lattice rotation; thermal gradients induced by the internal cooling channels. According to the laws of thermodynamics, gas turbine thermal efficiency increases with increasing inlet turbine temperatures. Therefore, the only practical limitation to unprecedented efficiency is the ability of the blade material to endure such an extreme environment. Single crystal superalloys, mostly Nickel-based, has been so far the material of choice for such high-temperature applications offering better efficiency, and consequently reducing emissions [6, 7]. Absence of grain boundaries eliminates the need of including grain boundary strengthening elements and thereby improving the temperature tolerance of these single crystal superalloys. In fact,every unique feature present in the microstructure of single crystal superalloys influences their exceptional mechanical properties at elevated temperatures.

Ni-based single crystal superalloys, an exemplar of modern-day material design brilliance, met with a new challenge with the emergence of extreme operating conditions for the turbine blades of twin-engine helicopters, known as One Engine Inoperative (OEI). This condition is met in an emergency when one of the two engines stops. The second engine, which is still running, requires additional power leading to both a rapid increase in temperature at the turbine inlet (usually,1050°C to 1200°C in 5 seconds at the blades) and an increase in the rotation speed of the blades. Therefore,

these exceptional materials, however, still need to be rigorously evaluated for estimating safety factors for design loading.

For certification, Ni-based single crystal superalloys are severely scrutinized to perform in the visco-plastic regime as well as under severe loading paths, including temperature surge and rapidly repeated overheating for testing the One Engine Inoperative events. These OEI regimes can be introduced at various times during certification tests (early, mid-life, end life) and repeated. As the lifetime of superalloys is mainly governed by the coherence of their bi-phased $\gamma/\gamma^{'}$ microstructure, a more fundamental understanding of microstructural instabilities would help in incorporating the loading rate and the history dependence of the material response in the constitutive relations. An accurate numerical prediction of material degradation in severe in-service conditions, and extreme certification conditions are, in fact, of both industrial concern and academic curiosity.

The physical behaviour of these single crystal superalloys are still not yet fully understood as there are many processing-microstructure-property relations which makes the material design space rich with variables that are also functions of operating conditions and crystal growth direction.

	Cr	Co	Mo	W	Al	Ti	Ta	Re	Hf	Ni
CMSX-4	6.5	9	0.6	6.5	5.6	1.0	6.5	3.0	0.1	Bal

Table 1.1: Chemical composition (in weight $\%$) of the Ni-based single crystal superalloy(CMSX-4)

In the design of a superalloy, different quantities of alloying elements (listed in Table 1.1), having various beneficial properties, are added. Subsequently, due to differential partitioning, these alloying elements preferentially forms two phases during the microstructure formation, namely, the $\gamma^{'}$ precipitates and the γ matrix. This unique microstructure, therefore, consists of harder $\gamma^{'}$ precipitates of ordered intermetallic Ni_3Al phase embedded in a disordered face-centered cubic (FCC) γ phase (solid solution of nickel) [7]. The low diffusion rates of the refractory elements

give the exceptional resistance of Ni-based single crystal superalloys to creep deformation [8]. The alloy element Re has the lowest mobility and, thus, effectively controls the phase transformation. Most of the commercially used superalloys have a negative natural lattice misfit between the phases [9]. Their unprecedented creep properties are critically dependent on alloy composition (elastic anisotropy, natural lattice misfit), heat treatments ($\gamma/\gamma^{'}$ size), operating conditions (temperature and stress), and crystalline orientation. While it is true that much of the attractive high-temperature properties of these Ni-based single crystal superalloys boils down to the coherent bi-phased γ/γ' microstructure and the stability of their interfacial dislocation network, the strong processing-microstructure-property relation with regards to the crystallographic orientation of the single-crystal turbine blades is often overlooked.

A typical standard heat treated Ni-based single crystal superalloy sample has a distinct bi-phased $\gamma/\gamma^{'}$ microstructure [7]. The precipitation of a high volume fraction (close to 70 $\%$) of the long-range ordered $L1_2$ $\gamma^{'}$ phase appears as cubes coherently embedded in a face-centered cubic (fcc) solid solution γ matrix [10]. The ordered crystal structure of the $\gamma^{'}$ phase restricts the motion of dislocations to the softer γ phase. At high temperature/low stress, the $\gamma^{'}$ precipitates directionally coarsen, phenomenon known as rafting[11]. The morphology and kinetics of rafting are mainly dependent on the sign and magnitude of the applied stress [12], the lattice misfit [11, 13] as well as the elastic inhomogeneity [14] and anisotropy between the phases [15, 16].

The natural lattice misfit is defined as:

$$\delta = 2\frac{a_{\gamma'} - a_{\gamma}}{a_{\gamma'} + a_{\gamma}} \tag{1.1.1}$$

where, $a_{\gamma'}$ and a_{γ} are the free lattice parameters of the $\gamma^{'}$ and γ phases, respectively. A negative misfit alloy has $a_{\gamma'}$ less than a_{γ}.

The performance of Ni-based single-crystal superalloys is highly correlated with their microstructures. The magnitude and sign of the natural lattice misfit between the γ and $\gamma^{'}$ phases plays the most important role to establish a controlled size, shape, and distribution of $\gamma^{'}$ precipitates during heat treatments as well as define the direction of the rafting, viz. the directional

coalescence of $\gamma^{'}$ precipitates. During high-temperature thermo-mechanical loading, the $\gamma^{'}$ phase coalesces, directionally coarsens, and is finally topologically inverted, viz. surrounds the γ phase and acts as the matrix. The lifetime of Ni-based single crystal superalloys is indeed connected to the integrity of the strengthening phase, $\gamma^{'}$. Hence, fundamentally understanding and predicting how the mechanical behavior of the $\gamma^{'}$ phase softens with the evolution of damage is essential to improve their lifetime predictions. For alloy certification, Ni-based single crystal superalloys are severely scrutinized to perform in the visco-plastic regime as well as under severe loading paths, including temperature surge and rapidly repeated overheating. An accurate numerical prediction of material degradation in severe in-service conditions and extreme certification conditions are, in fact, of both industrial concern and academic curiosity.

During the grain selection process for manufacturing single-crystalline superalloys, $<001>$ direction being the easiest solidification path for casting (and having the lowest stiffness of all directions) is chosen as the preferred crystallographic growth direction for the best combination of properties when designed along with cuboidal $\gamma^{'}$ precipitates having a size of 450-500 nm and volume fraction of 60-70$\%$. Turbine blades also exhibit strong material anisotropy. The differences in the crystal anisotropy axis orientation, therefore, lead to a significant scatter in properties resulting in a mistuned-bladed assembly inside the aircraft engine. In a $<001>$ oriented specimen, depending on the sign of natural lattice misfit and applied stress, the rafts are formed either perpendicular (negative misfit/positive stress and positive misfit/negative stress) or parallel (negative misfit/negative stress and positive misfit/positive stress) to the loading axis. However, the orientation of precipitates and directional coarsening is at 45° to the applied stress axis in $<011>$ as compared to $<001>$. Despite knowing that different orientations have different rafting characteristics in Ni-based single crystal superalloys, not many studies were dedicated to understand the sensitivity of microstructural evolution due to variation in crystallographic orientations.

1.2 Background and Literature Review

A Ni-based single crystal superalloy was used in the manufacturing of the turbine blade of jet engines from the late 1970s. Since then, there has been much promising development in making

the superalloy stronger and last longer by tweaking the composition of the alloying elements. The first significant development was the introduction of the refractory element rhenium (Re), which introduced significant creep advantages due to the solid solution strengthening effects [17]. Since Re is a heavy earth element with lower mobilities and diffusion rate, the thermally activated mechanisms controlling the high-temperature deformation and damage mechanisms are naturally slowed down, thus, improving creep life. However, with the addition of Re, the castability issues and formation of deleterious TCP phases became a significant problem. Depending on the content of Re, the Ni-based single crystal superalloys have been classified into the first generation (having 0 wt$\%$ Re), second-generation (with 3 wt$\%$ Re) and third-generation single crystal superalloys containing about 6 wt$\%$ Re. However, third-generation superalloys,despite their excellent creep strength at high temperatures, have not been commercially used due to blade casting issues, poor oxidation resistance at high-temperature and poor phase-stability due to the TCP phases [18]. Fourth, fifth, and even sixth generation superalloys have also been developed with the addition of ruthenium making them commercially expensive than the previous generations.

Rafted microstructures make the high-temperature creep mechanism involving dislocation climb around the $\gamma^{'}$ precipitates difficult [19]. The interfacial dislocation networks formed with 60° segments of 1/2$\langle 110 \rangle$ dislocations [20] inhibit dislocation glide up to the $\gamma/\gamma^{'}$ interface and interfere with the shearing mechanism by obstructing the dislocation glide through the channels and the formation of superdislocations [21]. While rafting occurs during the primary creep stage and is stable during the secondary one [22], the transition between the secondary and tertiary creep stages comes with a topological inversion, viz. the $\gamma^{'}$ phase is now surrounding the γ phase [23, 24, 12, 25]. This phenomenon comes with a destabilization of the interfacial network allowing dislocations to enter into the $\gamma^{'}$ phase, which is considered as a damaging process since it leads to an increase in the plastic strain rate occurring in the tertiary creep stage [26, 27]. During service, the loss of coherence of the $\gamma/\gamma^{'}$ microstructure, therefore, triggers untoward events such as destabilization of interfacial dislocation network and topological inversion leading to insidious turbine blade failure [25].

Alloying elements also have a major role in this process by providing the $\gamma^{'}$ precipitates with a higher APB energy [17] and preventing the inversion as long as the APB energy is higher than twice of the $\gamma/\gamma^{'}$ interfacial energy [28]. The addition of refractory elements such as Ru prolonged the secondary creep stage and, therefore, delays the onset of topological inversion [22]. For instance, the addition of 3 wt$\%$ Ru reduces the $\gamma^{'}$ volume fraction and lead to more perfectly shaped $\gamma^{'}$ lamellae. Furthermore, the regularity of the $\gamma^{'}$ lamellae helps in resisting dislocation cutting [22]. Fredholm and Strudel first noticed the role of alloying elements and the $\gamma^{'}$ volume fraction on the topological inversion phenomenon by evaluating the microstructures of Alloy 221 and 211 [23]. Caron et al. [25] underlined the above analysis and validated it using several experimental tests and showed that there was a strong co-relation between $\gamma^{'}$ volume fraction and topological inversion: there is less chance of $\gamma/\gamma^{'}$ topological inversion for $\gamma^{'}$ volume fraction less than 50%. It is due to a minimization of the total $\gamma/\gamma^{'}$ interfacial area (and in turn the total interfacial energy) resulting in a topological inversion of the phases for volume fractions higher than 50%. Furthermore, Caron et al. stated that topological inversion induces a higher dislocation activity in both phases leading to an acceleration in the plastic strain rate [25]. Goerler et al. [29] showed that topological inversion occurs in the interdendritic regions (where $\gamma^{'}$ volume fraction is around 65%) but not in the dendritic ones ($\gamma^{'}$ volume fraction less than 50%). Here, in this study, we are not considering the inhomogeneity of the material. A study predicted an elastic stress-driven phase inversion using phase-field simulations in elastically inhomogeneous binary alloy system see [30]. However, the scope was limited to quantitative estimation of the dependence of phase inversion on modulus mismatch and elastic anisotropy.

Topological inversion of the microstructure takes place even under the absence of an applied load during long-term aging processes [25]. Recently, in the study by Goerler et al. [29], topological inversion was predicted for long-term aging processes using a phase-field model. Topological inversion was simulated by artificially lowering the eigenstrain and strength of the wetting condition over time so that the effect of the reduction of misfit effect due to dislocation activity and the loss of coherency at the $\gamma/\gamma^{'}$ interfaces can be modeled. In the present study, the attention

is on damaging mechanisms during in-service conditions. Therefore, the focus will be on investigating factors responsible for the topological inversion during high-temperature/low stress creep conditions. Zhou et al. [28] have shown using phase-field simulations that it is possible to predict precipitate-matrix inversion by removing the eigenstrain caused by the lattice misfit between the phases and the antiphase domain boundary effect. However, the grid resolution and the presence of APB domains made the characterization of topological inversion challenging. A comprehensive phase-field study on the microstructural degradation, including topological inversion, during creep in Ni-based single crystal superalloys, is missing in the literature, in the best of authors' knowledge. Here study, neither the reduction of misfit nor explicitly examining the effect of plastic strains is considered. In fact, Cottura et al. [16] showed that a plastic energy density function is not necessary to predict rafting while it was confirmed that the inhomogeneity of the shear modulus plays a primary role on the microstructural evolution. Moreover, in the following, the softening effect during secondary and tertiary creep will be implicitly taken care by a damage variable to predict various creep deformations.

Turbine blades also exhibit strong material anisotropy. The differences in the crystal anisotropy axis orientation, therefore, lead to a significant scatter in properties resulting in a mistuned-bladed assembly inside the aircraft engine[31, 32]. Further, the microstructural evolution is different in different crystal orientations. Commercially used Ni-based SX superalloys are aged optimally to cuboidal shaped γ' precipitates with a size of around 450-500 nm and high γ' volume fraction [6]. For a $\gamma^{'}$ size in the range 350-500 nm, the highest creep strength is obtained near <001> [33]. However, due to the anisotropy in the mechanical properties, the creep properties of Ni-based SX superalloys do not hold the same for all orientations and all precipitate sizes. To be specific, Caron et al. found that a precipitate size of 500 nm, known to yield an optimum creep life for <001>-orientation, drastically reduces the stress-rupture life in the case of <111>-oriented specimens [33]. On the other hand, γ' precipitates with 200 nm significantly improved the strength of <111>-oriented specimens. Therefore, the anisotropy in the creep properties between <001> and <111> can be minimized by appropriate precipitate heat treatments that are tailored for the

component's operating temperature.

The pattern and orientation of γ' precipitates in the cuboidal state are different in different crystallographic orientations. During high-temperature/low-stress creep, the γ' precipitates directionally coarsen, known as γ' rafting. In a $<001>$ oriented specimen, depending on the sign of natural lattice misfit and applied stress, the rafts are formed either perpendicular (negative misfit/positive stress and positive misfit/negative stress) or parallel (negative misfit/negative stress and positive misfit/positive stress) to the loading axis [34]. However, the orientation of precipitates and directional coarsening is at 45° to the applied stress axis in $<011>$ as compared to $<001>$ [35]. The plate-like rafts [35] in $<001>$, the 45 degree rod-like rafts [35, 36, 37] in $<011>$, and the irregular coarsening [33, 38] in $<111>$ suggests clearly the sensitivity of microstructural evolution with respect to crystallographic orientations and their direct effect on the mechanical properties [37]. Despite knowing that different orientations have different type of rafting in Ni-based single crystal superalloys, not many studies were dedicated to understand the sensitivity of microstructural evolution due to variation in crystallographic orientations.

Studies in the past showed that there was a significant deterioration of mechanical properties in DD6 single crystal superalloys when the misorientation exceeds about 10° [39, 40]. Sass et al. reported that even a small misorientation from the $[001]$-$[011]$ boundary of the stereographic triangle promotes extensive: single-slip on $\{111\}$ $<112>$ systems or coplanar-slip on $\{111\}$ $<110>$ systems resulting in higher primary creep strain and creep rates [41]. They also reported that the creep properties resulting due to small misorientations from $[001]$ and $[011]$ depends strongly on the direction of deviation[41], i.e., the specimens with orientations near $[001]$-$[011]$ were found to have better creep strength compared to those with orientations closer to the $[001]$-$[\bar{1}11]$ or $[011]$-$[\bar{1}11]$ boundaries of the standard stereographic triangle [41, 42]. Moreover, the orientations near the $[011]$-$[111]$ boundary exhibited very short creep lives [33, 41]. Another experimental study [43] reported that orientations closer to the $<100>$-$<111>$ boundary display high primary creep, high ductility and low rupture life. In short, even a slight crystallographic misorientation or misalignment of load axis can cause significant deviations from the expected microstructural evolution in

Ni-based SX superalloys. As the stability of the microstructure dictates the structural integrity of the blades, it is vital to consider misorientations and quantify their effect on the creep performance. Though there have been many experimental studies on the effect of crystallographic orientations [33, 37, 44], very little has been studied on the effect of misorientations on the microstructural evolution in Ni-based SX superalloys[41, 45]. Hence, it is of prime importance to study the effect of misorientations on directional coarsening of Ni-based SX superalloys.

The dependence of the yield stress at 0.2% in tension has been observed by many authors[46, 47, 48, 49]. Shah et al. have studied this phenomenon in more detail since they coupled the dependence of the yield stress to the orientation and the tension/compression asymmetry in the case of the monocrystalline superalloy PWA 1480 at 593°. A strong tension/compression asymmetry is effective at this temperature level and is explained by a difference in the critical resolved shear stress (CRSS) between tension and compression on the octahedral slip systems [50, 51]. The same authors evidenced that the size of the γ' precipitates has an effect on the yield stress for $\langle 001 \rangle$ and $\langle 111 \rangle$. The γ' precipitates with a characteristic size about 300 nm allow to improve the yield strength for $\langle 111 \rangle$. This result is in accordance with what was found by Caron et al. [33] for creep. The asymmetry tension/compression decreases with the temperature: only 10 MPa at 950° for $\langle 001 \rangle$ on the AM1 alloy while it was 166 MPa [52] at 593° for $\langle 001 \rangle$ on the PWA 1480 alloy.

Just like the precipitate morphology, the associated dislocation configurations are also different in various crystallographic orientations [37]. For instance, when the crystallographic orientation changes from $[001]$ to $[111]$, the number of active slip systems evolves from 8 octahedral slip systems (Schmid factor = $\frac{1}{\sqrt{6}}$) to 6 octahedral slip systems (Schmid factor = $\frac{3}{2\sqrt{6}}$), respectively [53]. In terms of mechanical properties, specimens closer to $[111]$-orientation showed a lower creep strength than $[001]$ specimens [41, 37] even though the Schmid factors of the primary octahedral system are higher in $[001]$ than in the $[111]$ orientations [54]. While, in $[011]$ orientation, the γ' phase is observed to be sheared by the stacking-fault mechanisms in the primary creep stage itself [37], however, that isn't the case in $[001]$. It was reported in [44] that during creep tests, the $<011>$-oriented specimens shows poor creep ductility and crystallographic fractures along one of

the $\{111\}$ planes. Cracking along $\{111\}$ is reasonable considering the maximum shear stresses in the octahedral planes [49].

The difference in the lattice parameters of the two phases induces an elastic coherency strain, a vital factor in the alloy strengthening process [55]. Here, the sign and magnitude of the natural lattice misfit between the γ and $\gamma^{'}$ phases plays the most important role in establishing a controlled shape and size of $\gamma^{'}$ precipitates[6], their distribution [56] and coarsening during heat treatments[57] as well as the distribution of internal stresses in the non-deformed state [58]. The lattice misfit creates in-homogeneous elastic internal stresses that are concentrated in the γ phase. The microstructure concomitantly gets relaxed upon creating screw dislocations on $\{111\}$ planes in the γ and further leading to the formation of 60° dislocation segments located in the $\gamma/\gamma^{'}$ interfaces. In order to compensate the misfit, these 60° dislocations climb into edge positions and build interfacial dislocation networks [59] that are critical to the stability of the microstructure.

1.3 Motivation for the study

During high-temperature thermomechanical loading, the cuboidal shaped $\gamma^{'}$ phase coalesces, directionally coarsens, and is finally topologically inverted, viz. surrounds the γ phase and acts as the matrix. However, the orientation of γ' precipitates in the cuboidal state is different in different crystallographic orientations. During high-temperature/low-stress creep, the γ' precipitates directionally coarsen, known as γ' rafting. In a $<001>$ oriented specimen, depending on the sign of natural lattice misfit and applied stress, the rafts are formed either perpendicular or parallel to the loading axis. However, the orientation of precipitates and directional coarsening is at 45° to the applied stress axis in $<011>$. The plate-like rafts in $<001>$, the 45 degree rod-like rafts in $<011>$, and the irregular coarsening in $<111>$ suggest clearly the sensitivity of microstructural evolution with respect to crystallographic orientations and their direct effect on the mechanical properties. Further, any slight misorientations within a blade result in anomalies in the microstructural evolution under load, thereby, generating anisotropy in the bladed assembly. As the stability of the microstructure dictates the structural integrity of the blade, it is essential to understand the microstructural state as a function of the crystallographic orientation and also quantify the effect

of misorientations on the creep performance.

The performance of Ni-based single crystal superalloys is highly correlated with the integrity of the $\gamma/\gamma^{'}$ microstructure. Hence, fundamentally understanding and predicting how the mechanical behavior of the $\gamma^{'}$ phase softens with the evolution of damage is essential to improve their lifetime predictions. The complete destabilization of microstructure, otherwise known as the topological inversion, comes along with an increase in the plastic strain rate known as the tertiary creep. X-ray tomography experiment has recently revealed that the tertiary creep initiates before the expected increase in the volume fraction of pores. Thus, the initiation of the tertiary creep stage might also be due to the destabilization of the $\gamma/\gamma^{'}$ interfacial dislocation network leading to the massive shearing of $\gamma^{'}$ rafts concomitantly resulting in topological inversion. To understand the damaging mechanisms separately in superalloys, it was necessary to isolate the effect of voids and precipitate softening. Therefore, to account for microstructural degradation as damage, macroscopic damage was embedded into the elasticity formulation in phase-field, which will then explicitly model the precipitate softening while implicitly accounting for plasticity dependent mechanisms in the tertiary creep. Phase-field simulations with a wide range of high-temperature/low-stress creep conditions will be studied to understand the microstructural degradation mechanisms leading to failure. The topological state of the microstructures from this creep-damage phase-field model (CDPF) will be characterized by calculating the termination densities of the γ and $\gamma^{'}$ phases.

1.4 Objectives of the Present Work

1. From a recent experimental study, it was found that the tertiary creep in Ni-based single crystal superalloys initiated before the expected increase in the volume fraction of pores. Therefore, it can be speculated that the initiation of the tertiary creep stage might be due to the destabilization of the $\gamma/\gamma^{'}$ interfacial dislocation network leading to the massive shearing of $\gamma^{'}$ rafts concomitantly resulting in topological inversion. We adopted a simplistic mechanistic approach of considering microstructural degradations through explicitly modeling the precipitate softening alone and, thereby, implicitly accounting for plasticity dependent mechanisms in the tertiary creep. For this, a generalized elasticity formulation was adopted

in the phase-field framework, which would help predict microstructural degradations during high-temperature/low-stress creep experiments. Here, the focus is on isolating the effect of voids from the current analysis and explain why it is also essential to consider microstructural degradation, if not critical, as an important damaging mechanism. The multi phase-field model, even though adept at predicting the aging and directional coarsening under the influence of external loads observed, failed to capture the loss of coherence of the microstructure during the secondary and tertiary creep stages. Therefore, it was deemed unfit for the prediction of complete microstructural evolution during high-temperature/ low-stress creep.

Therefore, the first objective in this dissertation course is to establish the right physics and phenomenological evolutionary laws in the otherwise generalized phase-field models to accurately predict the complete microstructural evolution in Ni-based single crystal superalloys during high-temperature/low-stress creep. The goal is to track the microstructural evolution (including microstructural destabilization in the secondary and tertiary creep) along a macroscopically obtained strain trajectory during a high-temperature/low-stress creep.

2. As established in the first objective, the changes in the microstructure play a prominent role in the macroscopic performance of the superalloys. Most macroscopic models, including finite-element crystal plasticity, so far have been using idealized or even homogenized microstructures to carry out macroscopic calculations. We tried to address this drawback by exporting <001>-oriented 3D Phase-Field microstructures into a finite-element crystal plasticity framework as statistical volume elements(SVE). This approach, in turn, helped in carrying out strain-controlled tensile tests to better understand the effect of the microstructural state on macro-scale performance [2]. Building up on this work, a micromechanics-based crystal plasticity model was further refined to account for the natural and constrained lattice misfits.

3. The microstructural evolution takes a different character depending on the crystalline growth direction. Therefore, the strong microstructure-property relation with regards to the crystal-

lographic orientation of the single-crystal turbine blades should not be overlooked. The third objective is to understand the effect of crystallographic orientations on the microstructural evolution and mechanical response of superalloys. To date, there has not been any numerical model, let alone phase-field models, that could capture the microstructural state as a function of the given crystallographic orientation. To address this deficit, a crystallographic-sensitive phase-field model capable of predicting the complete microstructural evolution at any given point on the standard stereographic triangle was developed. To assess the relative performance of the various perfectly-orientated and misoriented crystals, realistic phase-field simulations would be exported as SVE realizations, with which, strain-controlled tensile tests can be carried out using the model developed in objective 2.

4. Multi-axial stress states create microstructural gradients that alters the performance of the turbine blades. Therefore, it is interesting to understand how multiaxial stress states trigger microstructural instabilities such as lattice rotations during creep. Such instabilities could be studied by means of laboratory experiments using notched specimens. The fourth objective, therefore, is to perform multi-axial creep experiments using notched specimens coupled with microstructural characterizations to understand the kinetics of microstructural evolution and stress redistribution mechanisms depending on the initial anisotropy, the stress level and the stress triaxiality. Ultimately, lattice rotation due to the stress triaxiality will also be characterized through EBSD.

2. METHODOLOGY *

2.1 Introduction

Phase-field is a mesoscale model that solves interface problems with a diffuse-interface approach. Unlike the sharp interface models, here the explicit interface tracking is not required. To unravel the crystallographic sensitive microstructural evolution in Ni-based single crystal superalloys, a multi-phase field was extended to be crystallographic-sensitive as well as to capture the damage evolution during a high-temperature/low-stress creep test. Further, if these 3D phase-field simulations were to be exported as SVEs in to a finite-element crystal plasticity framework, then a realistic microstructure-sensitive macroscale modeling could be possible. This phase-field informed FE crystal plasticity approach could then quantify the effect of the microstructural state on the macroscale performance of the single crystal superalloys. In this chapter, the details of this modeling approach and the formulations will be discussed.

2.2 Phase-Field Method

Phase-field models have become a method of choice for the simulation of microstructural evolutions under various driving forces such as chemical, interfacial, elastic, etc. It describes the microstructure with a set of field variables that are continuous across the interfacial region. The model is based on defining a mesoscopic free energy functional given by the Landau theory [60] and providing the nexus between the microstructure, namely the concentration field c_i described by the conserved Cahn-Hilliard equation [61] and the order parameter field η_i described by the Allen-Cahn equation [62], and the total free energy. The aim of the phase-field modeling is, therefore, to describe the microstructure of the material at the mesoscopic scale using continuous fields. The

*Portions of this section are adapted from two journal articles[1, 3]

evolution of these fields is governed by both elastic, chemical and plastic driving forces [63, 64]. However, plastic driving force is not considered in this study. For the sake of completeness, a general formulation of the present phase-field model is explained in the next subsection.

A multi-phase field model, named OpenPhase, developed by I. Steinbach et. al. is utilized to simulate microstructural evolution [65, 66, 67]. The free energy formalism of this framework has multicomponent multiphase systems capable of predicting microstructural evolution on realistic length scales [68]. In this model, a continuous diffuse interface between phases is introduced using functions (here, the phase field parameter ϕ_α) which takes values between 0 and 1 under the condition

$$\sum_{\alpha=1}^{N} \phi_\alpha = 1 \tag{2.2.1}$$

$N = N(x)$ is the local number of phases. $\phi_\alpha(x)$ = 1 represents the bulk phase α and is, therefore, equal to zero in other bulk phases and has a smooth transition in the interfaces related to α. The evolution of these functions (see, [69]) is given by

$$\dot{\phi}_\alpha = \frac{\partial}{\partial t}\phi_\alpha(x,t) = -\sum_{\beta=1}^{N} \frac{\pi^2 M_{\alpha\beta}}{8\eta N} \left[\frac{\delta F}{\delta \phi_\alpha} - \frac{\delta F}{\delta \phi_\beta} \right] \tag{2.2.2}$$

where, η is the interface width, $M_{\alpha\beta}$ is the interface mobility between phases α and β and F is the free energy functional which includes the terms describing the interfacial f^{Intf}, chemical f^{Chem}, and elastic energy $f^{Elastic}$ over the domain Ω as given below

$$F = \int_\Omega (f^{Intf} + f^{Chem} + f^{Elastic}) dV \tag{2.2.3}$$

The process of phase transformation is hence driven by the minimization of this total free energy functional[70]. The interfacial free energy density is given by

$$f^{Intf} = \sum_{\alpha,\beta=1,\alpha>\beta}^{N} \frac{4\sigma_{\alpha\beta}}{\eta} \left[-\frac{\eta^2}{\pi^2} \nabla\phi_\alpha \cdot \nabla\phi_\beta + \phi_\alpha \phi_\beta \right] \tag{2.2.4}$$

where the interface width η is equal for all pairs of phases and $\sigma_{\alpha\beta}$ is the energy of the interface between phases α and β. The model assumes that a steady phase field contour along the interface normal is maintained at all times during the simulation which also ensures a constant η. This is important for the correct consideration of the interface properties and the resulting interface kinetics [66].

The chemical free energy is based on the bulk free energies of the individual phases $f_\alpha(c_\alpha)$ which depend on the phase concentrations c_α.

$$f^{Chem} = \sum_{\alpha=1}^{N} \phi_\alpha f_\alpha(c_\alpha) + \lambda \left[c - \sum_{\alpha=1}^{N} \phi_\alpha c_\alpha \right] \tag{2.2.5}$$

Here, the vector c is the overall concentrations in a mixture and λ is the generalized chemical potential vector, introduced as a Lagrange multiplier to conserve the mass balance between the phases as given below [66]

$$c = \sum_{\alpha=1}^{N} \phi_\alpha c_\alpha \tag{2.2.6}$$

Also, the generalized chemical potential is taken to be equal in all phases in interfaces and junctions. The evolution equation for concentration is given by the famous Cahn-Hlliard nonlinear diffusion equation [61, 71] given by:

$$\dot{c} = \nabla \left(\sum_{\alpha=1}^{N} M \nabla \frac{\delta F}{\delta c} \right) = \nabla \left(\sum_{\alpha=1}^{N} \phi_\alpha D_\alpha \nabla c_\alpha \right) \tag{2.2.7}$$

Here, $M = \sum_{\alpha=1}^{N} \phi_\alpha M_\alpha$ is the chemical mobility matrix that is related to the diffusion matrices, $D_\alpha^{ij} = M^{ik} \frac{\partial^2 F}{\partial c^k \partial c^j}$ in the individual phases comprising of multiple components, cross effects between the components and diffusion in all phases.

The elastic energy of phase mixture has the form:

$$f^{Elastic} = \frac{1}{2} \left\{ \sum_{\alpha=1}^{N} \phi_\alpha \left(\varepsilon_\alpha^{ij} - \varepsilon_\alpha^{*ij} \right) C_\alpha^{ijkl} \left(\varepsilon_\alpha^{kl} - \varepsilon_\alpha^{*kl} \right) \right\} \tag{2.2.8}$$

where, ε_α^{ij} are the components of the linear strain tensor for the phase α, ε_α^{*ij} are the eigenstrains

of the phase α, and C_α^{ijkl} are the elastic moduli of the phase α. Here, mechanical equilibrium between the phases is enforced, i.e., it is assumed to have stress continuity in the interfaces. With this, an effective stiffness matrix (known as the Reuss limit, see [72, 73]) and effective strain can be deduced as

$$C^{ijkl} = \left[\sum_{\alpha=1}^{N} \phi_\alpha [C_\alpha^{ijkl}]^{-1}\right]^{-1} \tag{2.2.9}$$

$$\varepsilon_\alpha^{ij} - \varepsilon_\alpha^{*ij} = \sum_{\alpha=1}^{N} \phi_\alpha [\varepsilon_\alpha^{ij} - \varepsilon_\alpha^{*ij}] \tag{2.2.10}$$

Now, the Eq. 2.2.8 becomes simple form which is no longer a linear function of ϕ_α [73]

$$f^{Elastic} = \frac{1}{2}\left(\varepsilon_\alpha^{ij} - \varepsilon_\alpha^{*ij}\right) C^{ijkl} \left(\varepsilon_\alpha^{kl} - \varepsilon_\alpha^{*kl}\right) \tag{2.2.11}$$

Finally, the phase field and concentration enter the mechanical equilibrium naturally and can be expressed as

$$0 = \nabla \frac{\delta F}{\delta \varepsilon} = \nabla \sum_{\alpha=1}^{N} \phi_\alpha C(\varepsilon_\alpha - \varepsilon_\alpha^* - c_\alpha^i \varepsilon^i) \tag{2.2.12}$$

In other words, stress distribution is coupled with phase field, and diffusion equations and thereby all the three evolution equations involving phase field, diffusion and elastic equilibrium are coupled [66, 73]. All the material parameters involved in this model are taken from a thermodynamic database, and the details of it's application to the phase-field simulation of Ni-based single crystal superalloy is explained in chapter 5.

2.3 Finite-Element Crystal Plasticity

A viscoplastic crystal plasticity framework with both the octahedral and cubic slip systems has been calibrated and implemented in the commercial software Z-set(Zebulon) [3, 2]. The constitutive model is based on a partitioning of the macroscopic strain into an elastic and a viscoplastic part as well as on a finite strain theoretical setting, as in [74, 75, 76]. The relationships defining the

elasticity are written at the macroscale, whereas the viscoplastic constitutive equations are written at the microscale, viz. at the slip system level. It is, therefore, a micro-macro approach that is, by definition, anisotropic due to the formulation at the slip system level. $\dot{\gamma^s}$ is the viscoplastic shear strain rate on a given slip system s (see Eq. 2.3.1) in which the resolved shear stress τ^s is obtained by the tensorial product between the macroscopic stress tensor σ and the orientation tensor $\underline{\underline{\mathbf{m^s}}}$, calculated knowing the normal to the slip system plane n^s and the slip direction in this plane I^s (see Eq. 2.3.2). The non-linear kinematic x^s (Eq. 2.3.3) and isotropic r^s (Eq. 2.3.4) hardening variables on the system s. They also possess dynamic recovery terms.

$$\dot{\gamma^s} = C_v sinh\left[\left(\frac{\langle|\tau^s - x^s| - r^s\rangle}{K}\right)^n\right] sign(\tau^s - x^s) \tag{2.3.1}$$

$$\tau^s = \underline{\underline{\boldsymbol{\sigma}}} : \underline{\underline{\mathbf{m^s}}} \tag{2.3.2}$$

where, $\underline{\underline{\mathbf{m^s}}}$ is defined as:

$$\underline{\underline{\mathbf{m^s}}} = \frac{1}{2}\left[\underline{\mathbf{n^s}} \otimes \underline{\boldsymbol{l^s}} + \underline{\boldsymbol{l^s}} \otimes \underline{\mathbf{n^s}}\right]$$

$$x^s = C\alpha^s \tag{2.3.3}$$

where,

$$\dot{\alpha^s} = \left[sign(\tau^s - x^s) - D\alpha^s\right]\dot{\gamma^s}$$

$$r^s = r_0^s + r_\delta + r_p^s \tag{2.3.4}$$

where,

$$r_p^s = \sqrt{\frac{2}{3}}\frac{GB}{w} + bQ\sum_{j=1}^{N_{syst}} h_{sj}\rho^j$$

and,

$$\dot{\rho^s} = (1 - b\rho^s)\dot{\gamma^s}$$

Here, C_{visco}, K, n, C, D, b, and Q are temperature-dependent material parameters, r_0^s is the initial radius of the yield curve, i.e., the initial critical resolved shear stress on the slip system s, and ρ^j is the isotropic state variable on the slip system j that models the evolution of the dislocation density on each slip systems and is, therefore, related to dislocation hardening. Here, [h] is the interaction matrix. For the sake of simplicity and also owing to the fact that the contribution of the latent hardening is negligible, all the components of the interaction matrix are taken to be equal to 1. In this model, the shearing of $\gamma^{'}$ precipitates is not considered. The model is restricted in the primary and early stages of secondary creep and therefore the dislocations are not propagating in to the $\gamma^{'}$ phase for the small damage values considered here. Therefore, the Orowan stress will be equal to 0 for the $\gamma^{'}$ phase. Here, the misfit stress affects both the phases. Therefore, in our formulation, r_δ will act on both γ and $\gamma^{'}$ and will take a different form depending on the phase and the microstructural state(cuboidal/rafted). For a load applied in z direction, the r_δ will take the form:

$$r_\delta^\gamma = \frac{1}{\sqrt{6}}\left(\mathbf{C}^\gamma : \underline{\underline{\varepsilon_\delta}} f^\gamma\right) \tag{2.3.5}$$

$$r_\delta^{\gamma'} = \frac{K}{\sqrt{6}}\left(\mathbf{C}^{\gamma'}(\mathbf{S\text{-}I}) : \underline{\underline{\varepsilon_\delta}} f^{\gamma'}\right) \tag{2.3.6}$$

with,

$\underline{\underline{\varepsilon_\delta}} = \begin{pmatrix} \delta_0 & 0 & 0 \\ 0 & \delta_0 & 0 \\ 0 & 0 & \delta_0 \end{pmatrix}$, if the microstructure is cuboidal. If the microstructure is rafted, then:

$\underline{\underline{\varepsilon_\delta}} = \begin{pmatrix} \delta_\perp & 0 & 0 \\ 0 & \delta_\perp & 0 \\ 0 & 0 & \delta_\parallel \end{pmatrix}$,

The lattice misfit value is not phase dependent and is, most of the time, an average of what happens in the volume. It is why its effect on each phase is pondered by the volume fraction of each phase. The γ phase will be considered as a continuous medium while an Eshelby tensor will

be employed for the $\gamma^{'}$ precipitates.

The Eshelby tensor will be that of a spherical inclusion for cuboidal$\gamma^{'}$ precipitates and given by:

$$S_{1111} = S_{2222} = S_{3333} = \frac{7 - 5\nu}{15(1 - \nu)}$$

$$S_{1122} = S_{2233} = S_{3311} = \frac{5\nu - 1}{15(1 - \nu)}$$

$$S_{1212} = S_{2323} = S_{3131} = \frac{4 - 5\nu}{15(1 - \nu)}$$

The Eshelby tensor will take the description of an penny-shape for $\gamma^{'}$ rafts as follows:

$$S_{1111} = S_{2222} = \frac{13 - 8\nu}{32(1 - \nu)}\left(\pi\frac{a_z}{a_x}\right)$$

$$S_{3333} = 1 - \frac{1 - 2\nu}{1 - \nu}\left(\frac{\pi}{4}\frac{a_z}{a_x}\right)$$

$$S_{1122} = S_{2211} = \frac{8\nu - 1}{32(1 - \nu)}\left(\pi\frac{a_z}{a_x}\right)$$

$$S_{2233} = \frac{2\nu - 1}{8(1 - \nu)}\left(\pi\frac{a_z}{a_x}\right)$$

$$S_{3311} = S_{3322} = \frac{\nu}{1 - \nu}\left(1 - \frac{4\nu + 1}{8\nu}\pi\frac{a_z}{a_x}\right)$$

$$S_{1212} = \frac{7 - 8\nu}{32(1 - \nu)}\pi\frac{a_z}{a_x}$$

$$S_{2323} = S_{3131} = \frac{1}{2}\left(1 + \frac{\nu - 2}{1 - \nu}\frac{\pi}{4}\frac{a_z}{a_x}\right)$$

$$S_{kk11} = S_{kk22} = \frac{1-2\nu}{1-\nu}\frac{\pi}{4}\frac{a_z}{a_x} + \frac{\nu}{1-\nu}$$

$$S_{kk33} = 1 - \frac{1-2\nu}{1-\nu}\frac{\pi}{2}\frac{a_z}{a_x} + \frac{\nu}{1-\nu}$$

The parameter K is to ensure the positivity of $(r_\delta)^\gamma$and $(r_\delta)^{\gamma'}$ for positive and negative lattice misfits.

$$K = -\frac{I_3\left(\underline{\underline{\varepsilon_\delta}}\right)}{\left|I_3\left(\underline{\underline{\varepsilon_\delta}}\right)\right|}$$

Here, $I_3\left(\underline{\underline{\varepsilon_\delta}}\right)$ is the third invariant of the strain tensor $\underline{\underline{\varepsilon_\delta}}$.

3. PREDICTING MICROSTRUCTURAL DESTABILIZATION *

3.1 Background

It is well-known that damage and damaging mechanisms manifest in different forms in different materials (see [77] for a review). A comprehensive review of damage mechanics can be found elsewhere [78, 79, 80, 81, 82]. In fact, it has been recently demonstrated by ex situ X-ray tomography that the tertiary creep stage is not only due to an increase in the volume fraction of voids, but can be caused by a massive shearing of the $\gamma^{'}$ phase [83]. This result is in contradiction with the continuum damage mechanics (CDM) theory, which only considers the discontinuity of matter as damage, and, therefore, calls for improved formulations taking into account microstructural degradation as damage. However, it is also important to understand what causes the transition from secondary to tertiary creep stage. To that end, one of the goals here is to introduce a new formulation that considers microstructural degradation as a precursor to full material destabilization and porosity growth in the tertiary creep stage. In our proposed formulation, the dependence of the damage on the microstructure degradation is justified by the fact that it is associated only to the $\gamma^{'}$ phase. Therefore, such a formulation explicitly brings the softening effect of the strengthening $\gamma^{'}$ observed in the elasto-viscoplastic damageable materials. Here, the effect of porosity and fracture mechanisms will not be considered. Eventually, it is necessary to consider the interplay of the destabilization of the interfacial network, shearing of $\gamma^{'}$ particles, microstructural evolutions, void nucleation and growth in the damage models to fully explain what triggers the increase of the plastic strain rate in the tertiary creep stage leading to failure.

3.2 Damage Mechanics Approach

The CDM theory, based on the effective stress concept, considers damage as a discontinuity of matter, namely voids and cracks. In other words, CDM is formulated based on the decrease of

*Portions of this section are reprinted or adapted from [1] Rajendran Harikrishnan and Jean-Briac le Graverend, A Creep-Damage Phase-Field Model:Predicting Topological Inversion in Ni-based Single Crystal Superalloys. Materials & Design, Elsevier 160 (2018): 405-416. Copyright ©2018 by Elsevier Ltd. Reprinted with permission. https://doi.org/10.1016/j.matdes.2018.09.012

the cross-sectional area associated with the increase in the volume fraction of voids. This concept comes from Lemaitre who proposed the strain equivalence principle which allows modification of constitutive equations of an undamaged material to describe a damaged material [84, 85]. This is an extension of the effective stress formulation of Kachanov [78, 86], and Rabotnov [79, 87] who introduced a scalar damage parameter D to represent the loss of a load-carrying cross-section due to the nucleation, growth, and coalescence of microcracks. Ashby and Dyson has cassified damage based on several microstructural features and defined damage as the intrinsic softening of material due to dislocation multiplication and precipitate coarsening [88, 89]. Ashby and Dyson [88] also put across an important point that cavity damage appears only when the tertiary creep is well-established as proved later by the Ex-situ X-ray tomography characterization of porosity during high-temperature creep in a Ni-based single-crystal superalloy [83]. In the same spirit, we adopted a simplistic mechanistic approach by predicting microstructural degradations through explicitly modeling the precipitate softening alone and, thereby, implicitly accounting for plasticity dependent mechanisms in the tertiary creep. Here, the focus is on isolating the effects of voids from the current analysis and explain why it is also essential to consider microstructural degradation, if not critical, as an important damaging mechanism in the present material. In fact, in the present context of Ni-based single crystal superalloys, the idea of CDM theory can be conveniently re-interpreted as loss of effective load carrying area due to the softening and massive shearing of the $\gamma^{'}$ precipitates and hereby introducing the new microstructural damage variable M_D. That is, instead of modeling the effect of the voids, the Rabotnov-Kachanov damage model here is simply taking care of the effects of dislocations entering/shearing into the strengthening $\gamma^{'}$ phase and in turn softening the phase. Thus, such a damage mechanics formulation can be applied to the nanometer scale. The damage density function, M_D, (see Eq.3.2.3) evolving from 0 (undamaged state) to 1 (fully damaged state), can, therefore, be interpreted as the amount/effect of dislocations in the $\gamma^{'}$ phase and not as conventional mechanical damage.

According to the effective stress concept, the constitutive equations of any damaged material can be obtained by replacing the Cauchy stress in the constitutive equations of the correspond-

ing undamaged material with an adequately defined effective stress, $\tilde{\boldsymbol{\sigma}}$, related to the surface that effectively resists the load, namely:

$$\tilde{\boldsymbol{\sigma}} = \frac{\boldsymbol{\sigma}}{1 - M_D} \tag{3.2.1}$$

where $\bar{\bar{\sigma}}$ is the applied stress tensor. By replacing the applied stress by the effective stress, the flow rule for steady creep stage can be extended to the tertiary creep stage. In practice, the damage density function implemented in the phase-field model modifies the γ' stiffness matrix using an effective stress concept i.e., in Eq. 2.2.11, $\mathbf{C}_{\gamma'}^{ijkl}$ is modified as given below

$$\tilde{\mathbf{C}}_{\gamma'}^{ijkl} = \left(\mathbf{C}_{\gamma'}^{ijkl}\right)(1 - M_D) \tag{3.2.2}$$

The rate of damage evolution is given below in Eq. 3.2.3

$$\dot{M}_D = \left(\frac{\chi(\boldsymbol{\sigma})}{A}\right)^r (1 - M_D)^{-k} \tag{3.2.3}$$

where $\chi(\boldsymbol{\sigma})$ is the Hayhurst$^{'}$s equivalent stress [90] given by

$$\chi(\boldsymbol{\sigma}) = \alpha J_0(\boldsymbol{\sigma}) + \beta J_1(\boldsymbol{\sigma}) + (1 - \alpha - \beta) J_2(\boldsymbol{\sigma}) \tag{3.2.4}$$

Here, $r, k,$ and A are temperature-dependent material parameters and in the case of Ni-based single crystal superalloys: α=0 and β = 0.3 [91]. It needs to be noted that accumulation of damage often operates in a non-linear manner, i.e., the higher the stress is, the more abrupt the damage evolution is [92]. This has been modeled by Chaboche using a parameter k that takes the form of a second-order polynomial function depending on the stress [93]. Nonetheless, such function will not be used in the present model.

Further, in the damage formulation, the scalar damage variable, M_D, will only modify the $\gamma^{'}$ elastic parameters as it is assumed that the topological inversion is related to the softening of the $\gamma^{'}$ precipitates. This leads to a modification of the elastic energy which drives the rafting process [16, 94]. When M_D increases the elastic energy coming from the $\gamma^{'}$ phase is, therefore, decreased. In

the creep-damage phase field model, based on the parameters for the temperature/stress conditions, the damage equation gives out a value for M_D for each time step which then modifies the elasticity tensor of the $\gamma^{'}$ phase ($\boldsymbol{C}^{ijkl}_{\gamma'}$) in the elastic free energy function in Eq. 2.8 which subsequently modifies the free energy functional given in Eq. 2.3.

3.3 Creep-Damage Phase Field Model

A multi phase-field model coupled with a classical CDM formulation for creep, viz. a Rabotnov-Kachanov$^{'}$s law, is hereby used to predict the topological inversion and represents a step toward fundamentally understanding what damage is in the present context of Ni-based single crystal superalloys exposed to high-temperature creep loading. In fact, the idea of CDM theory can be re-interpreted here as the loss of effective load carrying area due to the softening and massive shearing of the precipitates. The parameters for the damage formulation used in the present phase-field model is, however, obtained from a macroscopic crystal plasticity framework with a Rabotnov-Kachanov damage formulation [95, 4].

For a computationally feasible simulation of multi-component alloy system like Ni-based single crystal superalloys, we consider a Ni-Al binary system in the phase-field model. Such a binary system further leads to an accelerated diffusion kinetics. The OpenPhase program utilizes accurate thermodynamics descriptions using a thermodynamic database (CALPHAD) to calculate the equivalent binary composition. The $\gamma^{'}$ phase is assumed to be stochiometric due to a narrow phase zone. Hence, the $\gamma^{'}$ phase is at equilibrium with a fixed concentration of 25 at.$\%$ Al while the matrix phase is at 15.4 at.$\%$ Al [96]. From the Ni-Al phase diagram, the uniform initial bulk concentration of Al is obtained for different temperatures, as listed in Table 3.1. The material parameters used in these simulations, for instance, stiffness coefficients, lattice misfit, thermodynamic quantities etc are similar to the ones obtained experimentally for CMSX-4 alloy. A diffusion coefficient (Al in γ matrix) of 6.0 E-15 m/s^2 is used in the simulations. The interfacial energy considered here are 1.5 J/m^2 and 0.5 J/m^2 respectively for $\sigma_{\gamma'/\gamma'}$ and $\sigma_{\gamma/\gamma'}$ (see Eq.2.2.4)[29]. Such a wetting condition would circumvent the numerical limitation of the diffuse interface assumptions in the elasticity formulation [29].

Temp.	Elastic Constants (γ)			Elastic Constants ($\gamma^{'}$)			Al concentration		Volume fraction
	C_{11}	C_{12}	C_{44}	C_{11}	C_{12}	C_{44}			
(° C)	(GPa)	(GPa)	(GPa)	(GPa)	(GPa)	(GPa)	γ Phase	$\gamma^{'}$ Phase	$\gamma^{'}$ Phase
1000	215.5	162.0	77.6	222.7	164.2	85.6	21.8	25	69.0%
1050	202.3	149.8	91.1	234.1	177.2	93.7	21.4	25	59.6%
1100	198.2	148.2	88.9	230.4	174.5	91.9	21.0	25	52.2%
1150	195.1	146.4	86.7	226.3	171.6	90.2	20.4	25	41.2%
1200	191.3	144.6	84.4	222.0	168.4	88.5	19.8	25	28.6%

Table 3.1: Phase-field parameters for different temperatures and the resulting volume fractions

The aging conditions are simulated from explicit seeding of nuclei viz. a quasi-random placement of nucleation sites. Here, in order to optimize the computational cost, a two-dimensional simulation box having 256 by 256 grid size with a grid spacing of 10nm was chosen for the phase-field simulations. Periodic boundary conditions are applied for all the simulations. The precipitate coarsening follows the cube root time law based on LSW theory [97, 98], i.e, the mean particle size increases with the cube root power of the aging time [99].

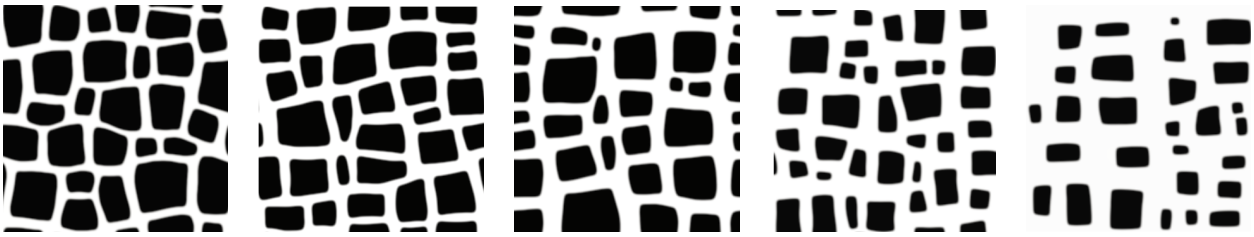

(a) 1000°C (b) 1050°C (c) 1100°C (d) 1150°C (e) 1200°C

Figure 3.1: Cuboidal microstructures obtained by the MPF model for different temperatures. $\gamma^{'}$ phase is shown in black color and γ phase in white transparency. Reprinted with permission from [1]

Elastic anisotropy and elastic inhomogeneity has a strong influence on the formation of cuboidal microstructures and their evolutions [14, 15, 16]. Table 3.1 contains elastic input for CMSX-4 al-

loys at different temperatures obtained from [100]. Here, the elastic inhomegenity parameter as defined in [16] ranges from 7.7% to 12.8%. It is to be noted that there is a strong correlation between unconstrained lattice misfit and the temperature [101, 102, 103]. However, in this study, the lattice misfit between the phases is assumed to be a constant value for all the different temperatures. An unconstrained lattice misfit of -0.3% is used here and it is similar to that of CMSX-4 type alloy in order to arrive at cuboidal facetet microstructures as shown in Fig. 3.1. The resulting microstructures, as shown in Fig. 3.1, will be used for performing the high temperature/low-stress creep conditions discussed in the next sections. Here, care has been taken to make sure that the $\gamma^{'}$ volume fractions of the resulting microstructures are consistent with the experimental values.

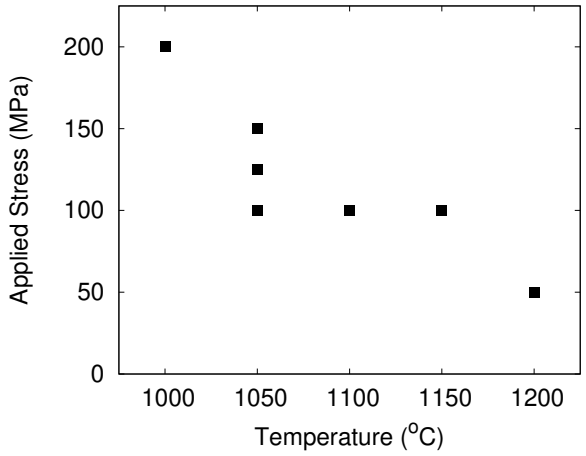

Figure 3.2: High-temperature/low-stress creep conditions analyzed in this study

High-Temperature/Low-Stress Creep Simulations

Once cuboidal precipitates are formed with an optimum average size of 450-500 nm, creep loading is initiated with a constant applied load. This stage of precipitate coarsening has a rather slow growth rate attributed to the formation of rafts[6]. Two phase-field models are considered in this study. One is the regular multi-phase field model (MPF) and second one is the creep-damage model (CDPF) with the damage formulation explained in section 3.2. In both the models, the

strength of the wetting condition is conveniently relaxed as it favours the directional coarsening of γ' precipitates during the creep loading. A range of temperature-stress creep conditions are investigated in order to assess the phase-field models on its ability to predict the complete microstructural evolution; study the effect of volume fraction on topological inversion and the effect of stress and temperature on the kinetics of topological inversion. The conditions for creep simulations are illustrated in Fig. 3.2 using the cuboidal microstructures as shown in Fig. 3.1.

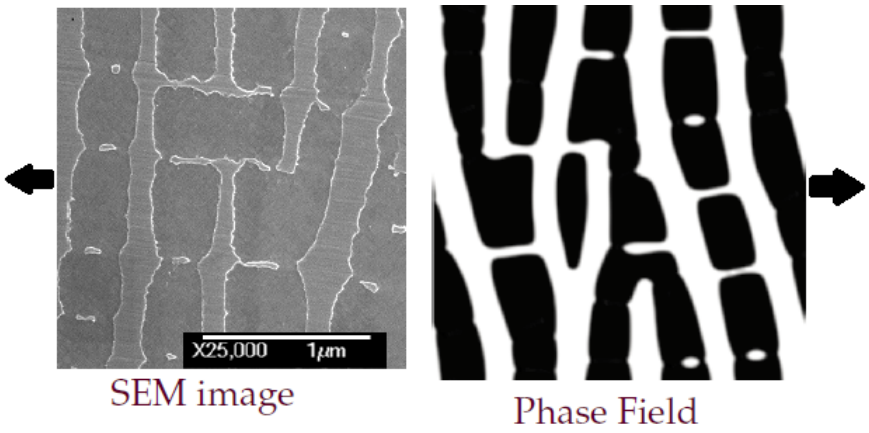

Figure 3.3: Comparison between an SEM observation of rafting in an $\langle 001 \rangle$ oriented Ni-based single crystal superalloy (MC2 alloy) with 2D phase-field simulation. The external load is applied along the horizontal direction.

In the Fig.3.3, γ' is the darker phase and γ is the lighter regions. A phase-field simulation of an actual creep experiment might not be feasible in terms of computational cost because of the long durations required to reach the steady state regime. Moreover, the time taken for the phase-field creep simulations are dependent on several factors such as CPU specifications and simulation set-up and therefore should not be co-related with the actual time of the creep experiment. Here, the acceleration of the creep-damage simulation is primarily dependent on the rate controlling process of damage evolution. Hence, the rate of damage evolution in the CDPF model should be realistic in order to mimic the actual evolution of damage. Moreover, it has to predict every microstructural state in the creep curve. To this end, the damage parameters are obtained from

an experimentally verified macroscopic damage model [95, 4]. Nevertheless, the advantage of the present CDPF model is that the rate of damage evolution is naturally slow and realistic enough to allow the microstructure to adapt to the changes caused by the modifications in the elastic energy.

It is known that the coarsening under the combined influence of stress and high-temperature ($T > 800°C$) is directional [13]. The orientation of rafts depends on the sign and magnitude of the lattice misfit between the phases [104]. The dislocations reduce the internal stresses and the cuboidal shaped precipitates coalesce together and form a plate-like structure that is perpendicular to the load axis in tension when the natural lattice misfit is negative (N-type), parallel otherwise (P-type)[34]. In all the phase-field simulations, the load applied is positive and in the horizontal direction resulting in a N-type raft (as the lattice misfit is negative) during the primary creep stage.

Fig.3.4 shows the isothermal coarsening under high-temperature and no external applied load. As the simulation progresses, the cuboidal microstructure becomes more rounded. Further coarsening leads to a incoherent state similar to a topologically inverted microstructure. This result is similar to the microstructural predictions by Goerler et al [29].

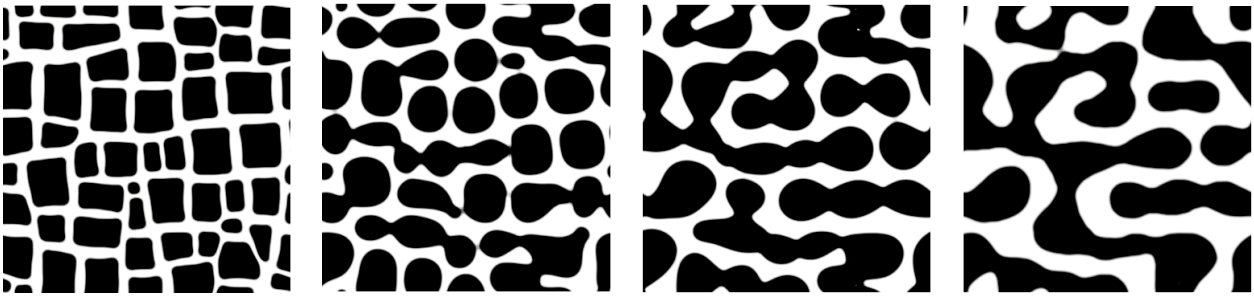

(a) Cuboidal (b) Rounded edges (c) Coarsened (d) Incoherent state

Figure 3.4: Coarsening under the influence of high-temperature and no external stress. $\gamma^{'}$ phase is shown in black color and γ phase in white transparency

Comparison of Phase-Field Models

The first task of the present study is to scrutinize the phase-field models based on their accuracy in predicting microstructural degradations during the various creep stages. For that, it is

also necessary to quantify the topological state of the simulated microstructures. The multi phase-field calculations are continued for longer durations to see if the model was capable of predicting the loss of coherence in the microstructure. Fig. 3.5 shows the results from the two different phase-field models, viz. with and without damage, using the same starting microstructure obtained for 1000°C. The applied stress for both the cases is 200 MPa. The top row in Fig. 3.5 are the simulations from the multi phase-field model while the bottom row shows the simulations with the damage formulation. The directional coarsening of the $\gamma^{'}$ precipitates, under the influence of applied stress, is observed in both the models. However, the loss of coherence of the microstructure is predicted only in the creep-damage phase-field simulations. The CDPF simulation shows a destabilized $\gamma/\gamma^{'}$ microstructure at the transition between the secondary and tertiary creep stages. Epishin et al. [24] investigated the kinetics of topological inversion during creep of the superalloy SRR99 at 980°C/200 MPa. Since, the volume fraction of $\gamma^{'}$ phase is the close to 70% at 1000°C, the phase-field damage simulations using 1000°C/200 MPa can be compared with the experimental observations of Epishin et al. The topological inversion observed in MC544 specimens during creep at 1050°C and 150 MPa from Caron et al. [25] will be compared with the phase-field simulations.

Fig. 3.5 shows the results from two different phase-field models using the same starting microstructure obtained for 1000°C. The applied stress for both the cases is 200 MPa. The top row in Fig. 3.5 are the simulations from the multi phase-field model while bottom row shows the simulations with the damage formulation. The applied stress for both the cases is 100 MPa. The directional coarsening of $\gamma^{'}$ precipitates, under the influence of applied stress, is observed in both the models; however, the loss of coherence of the the microstructure is predicted only in the creep-damage phase-field simulations. CDPF simulations shows a destabilized $\gamma/\gamma^{'}$ microstructure at the transition between the secondary and tertiary creep stages. It is also noticed that the evolution of damage is highly non-linear, as observed experimentally. As the applied stress increases, the damage value at rupture decreases indicating an accelerated damage kinetics in the material. However, the applied stress does not have a direct influence on the kinetics of damage evolution as the

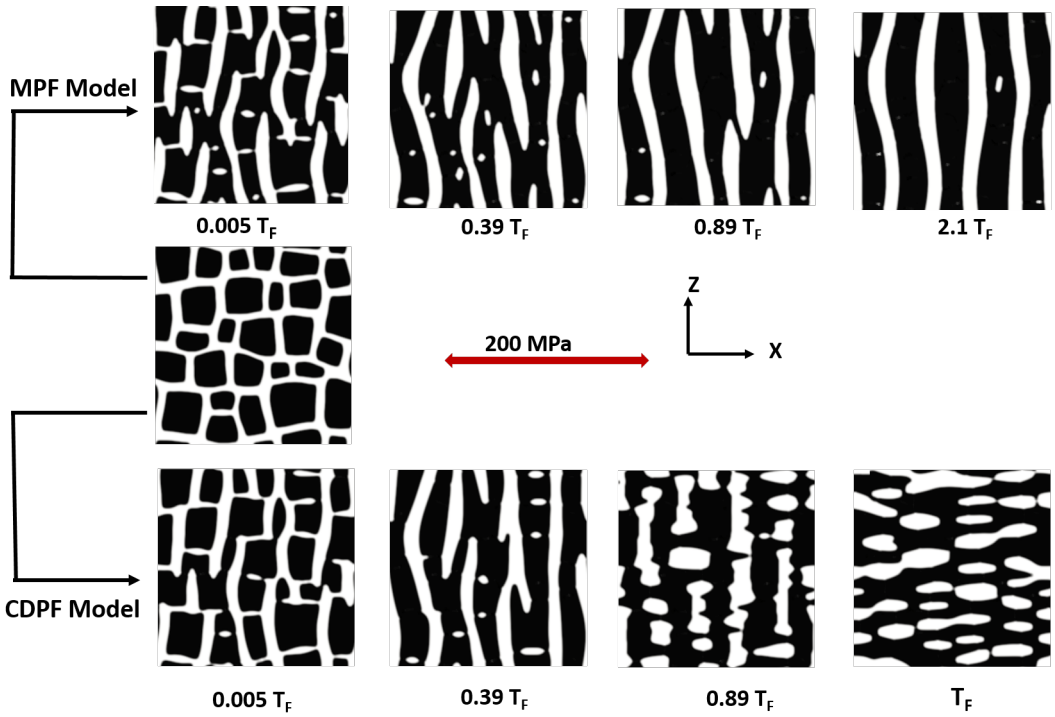

Figure 3.5: Comparison of simulations from multi phase-field model and creep-damage phase-field model for 1000°C/200 MPa. The load is applied along the x-direction and T_F is the time to rupture for the CDPF model. Reprinted with permission from [1]

k is not stress dependent in the classical Rabotnov-Kachanov type damage mechanics.

There are many characterization techniques by which SEM images can be morphologicaly quantified for its topological state. For instance, Fredholm and Strudel ([23]) and Caron et al. ([25]) used a connectivity number (also known as connexity number, N_c) per unit area in order to track the evolution of microstructure morphologies. This method involves the counting of phase terminations and triple points. Epishin et al. characterized the topological state of the microstructure by the ratio of area densities of γ and $\gamma^{'}$ terminations [24]. All these techniques involves manual image analysis. Such calculations, for minimizing statical errors, are required to be carried out on SEM images with length scale of the order of several micrometers. The present phase-field simulations were, however, on much smaller length scale with smaller area fractions. Such a simulated microstructure has less number of $\gamma^{'}$ precipitates compared to the SEM analysis. Hence, the above characterization techniques need to be modified in order to minimize the statistical errors

associated with smaller area fractions. In this study, the method of calculating termination densities was chosen and modified for characterizing the continuity of the phases. The number of γ terminations of the continuous phase is always assumed to be 1. The termination densities of $\gamma^{'}$ and γ phases, $\rho^{'}$ and ρ, were determined as the ratio of number of $\gamma^{'}$ and γ terminations over the area of the simulation box. Here, the simulation box has an area of 6.5536 μm^2. Finally, topological state is characterized by the termination density ratio ratio, $R = \rho/\rho^{'}$, plotted over a normalized phase-field timestep. When R is less than unity, it is understood that γ is the continous phase. When R takes the value between 0.5 and 1, the phases can be considered topologically equivalent like a rafted microstructure. When R is greater than 1, it marks the onset of topological inversion exemplified with the gradual loss of coherence of $\gamma^{'}$ phase. Further, with higher values of R, this technique suggest a fully enveloped $\gamma^{'}$ phase.

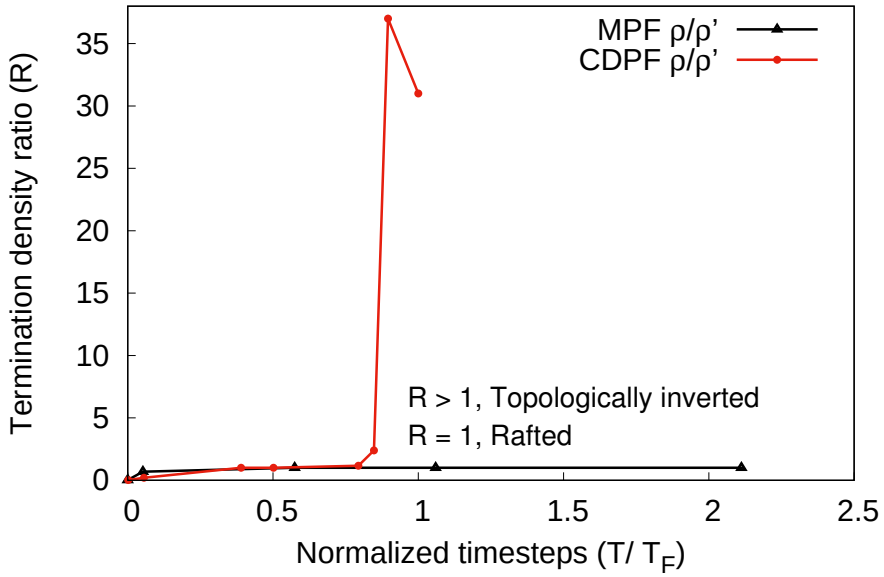

Figure 3.6: Comparison of Termination density ratios of MPF and CDPF models in 1000°C/ 200MPa with 69 % $\gamma^{'}$ volume fraction. Reprinted with permission from [1]

The topological state characterization for 1000°C/ 200MPa is shown in Fig. 3.6. Here, the

timesteps are normalized using the time to failure in CDPF model (T_F). From Fig. 3.6, it is strongly evident that both the models predicts the transition from cuboidal microstructure ($R \approx 0$) to the formation of a topologically equivalent microstructure ($R = 1$), i.e, rafting. The MPF model, however, does not predict the inversion of microstructure as the rafted microstructure remains in the rafted state. For 1000°C/ 200MPa, the CDPF model predicts the enveloping of $\gamma^{'}$ phase ($R >> 1$) and thus quantifies the topological inversion of microstructure. From this study, the MPF model is clearly deemed unfit for the prediction of microstructure at the end of secondary stage and in tertiary creep stage. Hence, for the rest of the study, the simulations will be performed using the CDPF model.

Predicting Topological Inversion

The acceleration of the creep-damage simulation is primarily dependent on the rate controlling process of damage evolution. Hence, the rate of damage evolution in the CDPF model should be realistic to mimic the actual evolution of damage. Moreover, it has to predict every microstructural state in the creep curve. To this end, the damage parameters are obtained from an experimentally-verified macroscopic damage model [95, 4]. Nevertheless, the advantage of the present CDPF model is that the rate of damage evolution is naturally slow and realistic enough to allow the microstructure to adapt to the changes caused by the modifications in the elastic energy.

The evolution of damage is highly non-linear, as observed experimentally. As the applied stress increases, the damage value at rupture decreases indicating accelerated damage kinetics in the material [105]. The kinetics of damage evolution in Ni-based single crystal superalloys based on the Rabotnov-Kachanov formulation is shown in Fig. 3.7. However, in the present study, the applied stress does not have a direct influence on the kinetics of damage evolution as seen Fig. 3. Also, the present damage model is not suited for non-isothermal conditions. In order to better predict and understand the damage kinetics, the present damage formulation needs to be modified in a way that the parameter k is stress dependent. This will be discussed in the later sections.

The multi phase-field model, used here, has proved to be adept in simulating the nucleation and growth during long-term aging resulting in the formation of cuboidal shaped microstructures

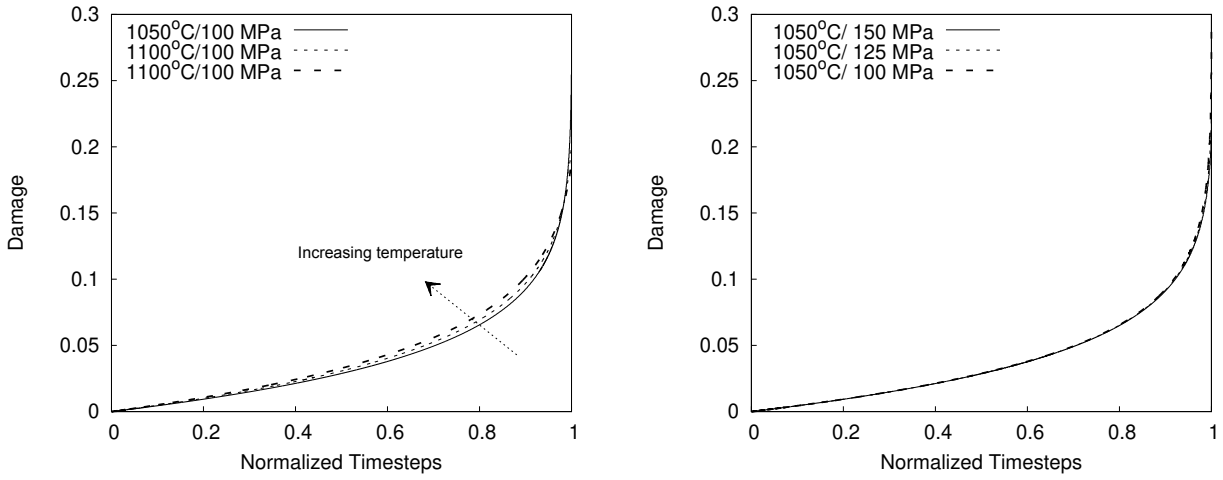

(a) Effect of temperature (b) Effect of stress

Figure 3.7: Kinetics of damage evolution in Ni-based single crystal superalloys based on Rabotnov-Kachanov damage formulation: (a) Effect of temperature, (b) Effect of stress

[29, 96]. Now, a creep loading is applied on the previously obtained cuboidal microstructures presented in Fig.3.1. It was observed that the multi-phase field simulations without the damage formulation is adequate in predicting rafting in the primary and secondary creep stages of Ni-based single crystal superalloys and are consistent with the SEM observations as shown in Fig.3.3. However, the first objective here is to scrutinize the present phase-field models based on their accuracy in predicting microstructural degradations during the various creep stages. For that, it is necessary to quantify the topological state of the simulated microstructures.

The results from the multi phase-field model and the creep-damage phase-field model will be compared using simulated microstructures taken at several chosen timesteps following the creep curve. The multi phase-field calculations are continued for long durations in order to see if the model was capable of predicting the loss of coherence in the microstructure. Also, for clarity of comparison, all the simulation timesteps are normalized by the rupture timestep of the corresponding creep-damage phase-field simulations (T_F).

The value of T_F from each simulation is calibrated using the creep curve from a macroscopic crystal plasticity framework with a coupled plasticity-damage formulation. That is, every point on

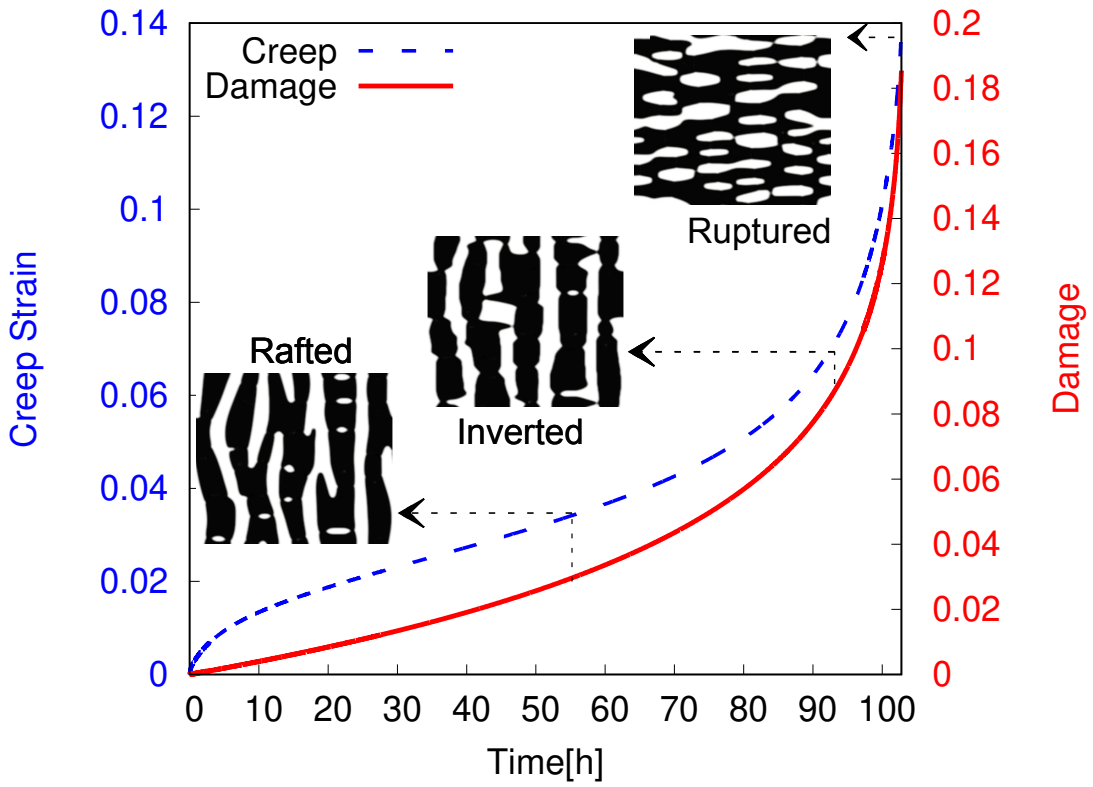

Figure 3.8: Macroscopic crystal plasticity creep curve with the CDPF damage evolution for 1000°C/ 200 MPa. CDPF microstructures at various points on the creep and damage curves are embedded inside. Reprinted with permission from [1]

the macroscopic creep curve corresponds to a macroscopic damage variable. As the creep-damage phase-field model is based on the parameters obtained from the macroscopic model, the phase-field damage variable, M_D, and the corresponding microstructure can be mapped directly on to the creep curve, as shown in Fig. 3.8. The dotted arrows indicates the microstructure at a point on the creep curve while the line arrows indicates the corresponding point on the damage curve. The macroscopic creep curve is plotted against creep strain and time to failure in hours whereas the damage evolution curve is plotted against M_D and the normalized phase-field timesteps.

The CDPF simulations does not directly predict an end point for the creep simulations. The final timestep (T_F) of CDPF simulation is therefore found by correlating the phase-field and the macroscopic damage variables. As every point on the macroscopic creep curve corresponds to a macroscopic damage variable, the macroscopic damage value at the time of rupture is noted and marked as the end point of CDPF simulations. Here, the macroscopic creep curve is plotted against creep strain and time to failure in hours whereas CDPF damage evolution curve is plotted against M_D and a normalized phase-field timestep (T/T_F), as presented in Figs. 3.8, 3.9, and 3.10.

The experimental studies on the effect of volume fraction on topological inversion revealed phase inversion for superalloys with $\gamma^{'}$ volume fractions higher than 50% [25]. Here, the effect of volume fraction on topological inversion is numerically investigated using the creep-damage phase-field model for volume fractions ranging from 28.6% to 69%. The simulated microstructures for each case is presented in Figs. 3.8, 3.9 and 3.10. Clearly, topological inversion is evident in all the cases except 1150°C/100 MPa with volume fraction 41.2% and 1200°C/50 MPa with volume fraction 28.6%. This is also quanitified using the evolution of topological density ratios plotted in Fig. 3.11. Further, it is noticed that the microstructures were not fully rafted in 1150°C/100 MPa and 1200°C/50 MPa. In reality, a low $\gamma^{'}$ volume fraction microstructure paves an easy route for the dislocations in the γ channels to terminate at the surface resulting in shorter lifetime.

The ruptured specimens (1000°C/ 200 MPa, 1050°C/ 150 MPa) having $\gamma^{'}$ volume fraction of 60% or more was found to have an unique arrangement of dispersed γ phase parallel to the direction of applied load. This rupture behaviour is quantified using the evolution of termination density

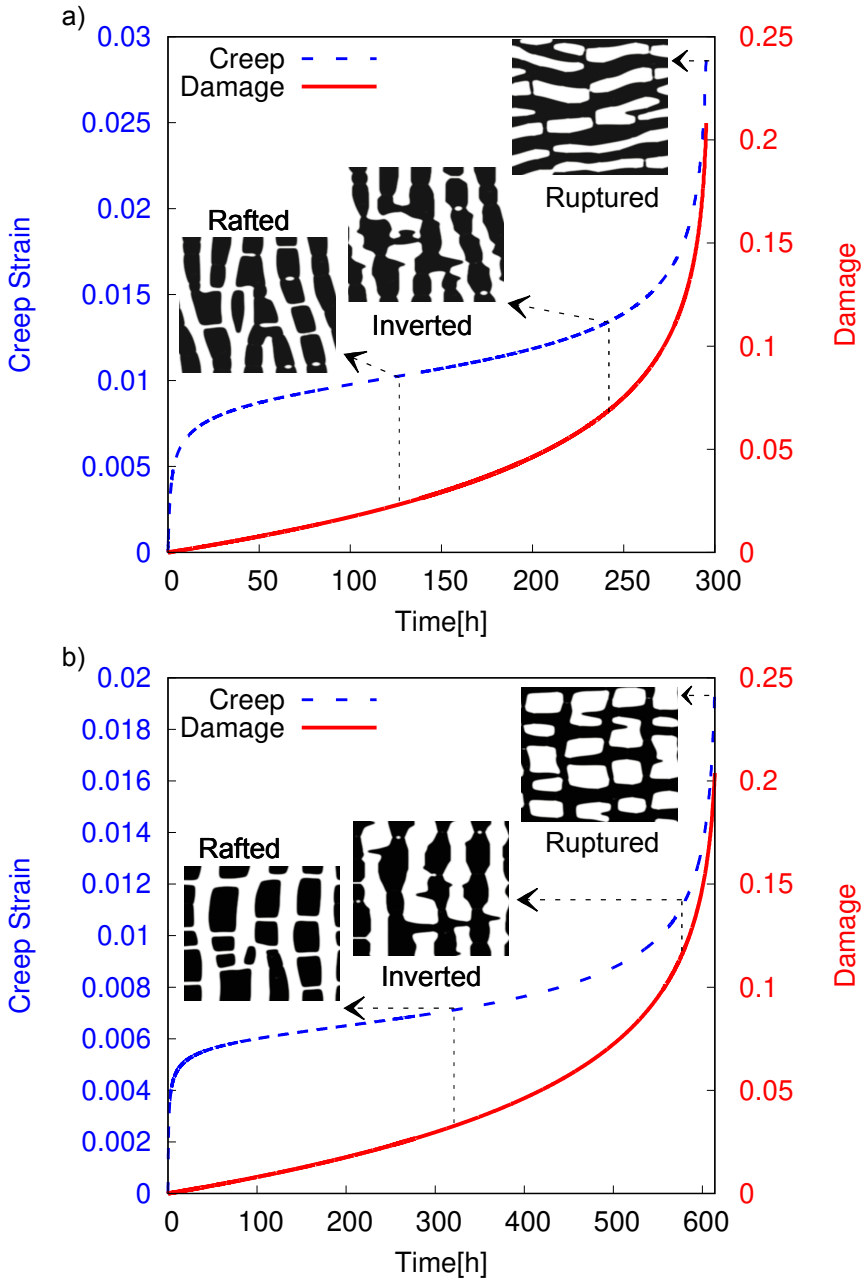

Figure 3.9: Macroscopic crystal plasticity creep curve with the CDPF damage evolution for (a) 1050°C/ 150 MPa, (b) 1100°C/ 100 MPa. CDPF microstructures at various points on the creep and damage curves are embedded inside. Reprinted with permission from [1]

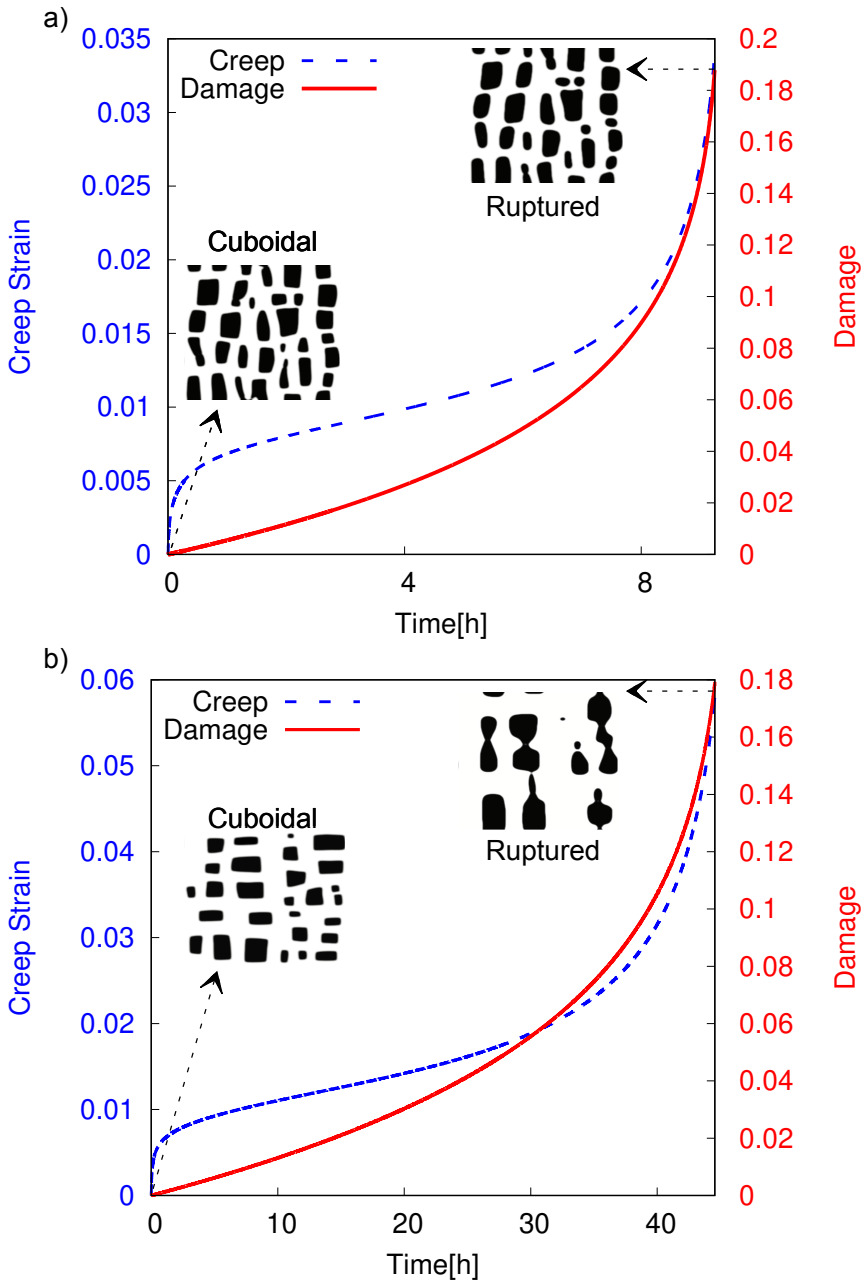

Figure 3.10: Macroscopic crystal plasticity creep curve with the CDPF damage evolution for (a) c)1150°C/ 100 MPa, (b) 1200°C/ 50 MPa. CDPF microstructures at various points on the creep and damage curves are embedded inside. Reprinted with permission from [1]

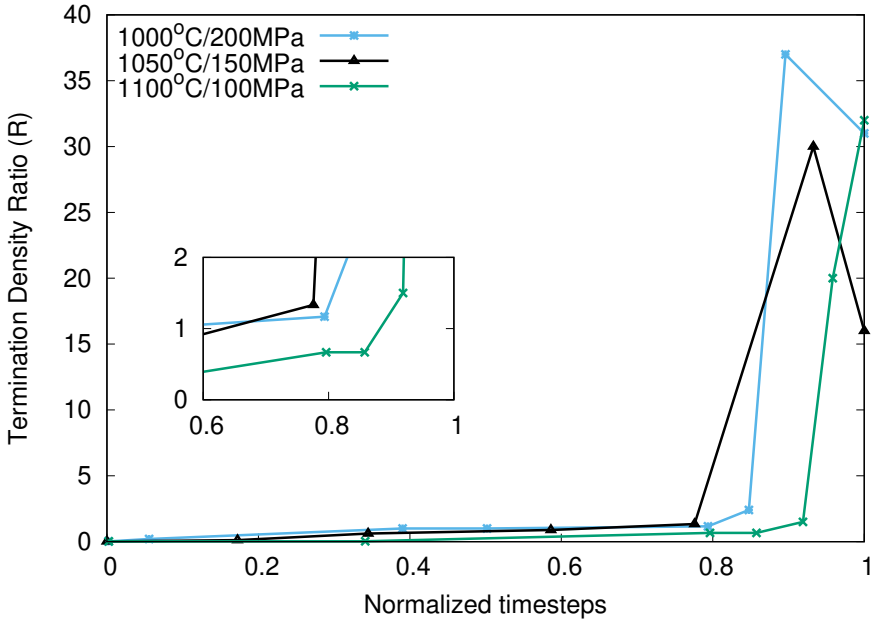

Figure 3.11: A plot of termination density ratios revealing the topological inversion in high-temperature/low stress creep. Topological inversion is marked with R greater than unity. Reprinted with permission from [1]

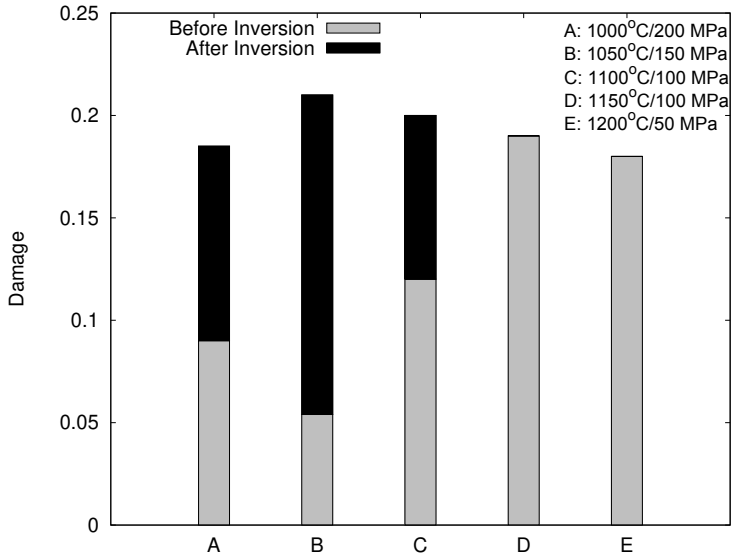

Figure 3.12: Range of M_D values for different temperature/stress conditions. Reprinted with permission from [1]

ratios presented in Fig. 3.11. Further, the range of M_D values for different conditions is illustrated in Fig. 3.12. The termination density ratio, R, of simulations with $\gamma^{'}$ volume fraction greater than 50% increases from 1 to a higher value during accelerated creep. However, for conditions with volume fraction 60% or more, there is a drop in the value of R after reaching a maximum value. This is due to anhilation of terminations in the highly dispersed γ phase, N, leading to a parallel-type coalescence of γ phase before the rupture. This trend in the termination density ratio was earlier observed in the experimental study of Epishin et al. [24]. However, there were no other experimental verification of such kind of ruptured microstructures with an anomalous microstructure other than the study conducted by Murakumo et al [106].

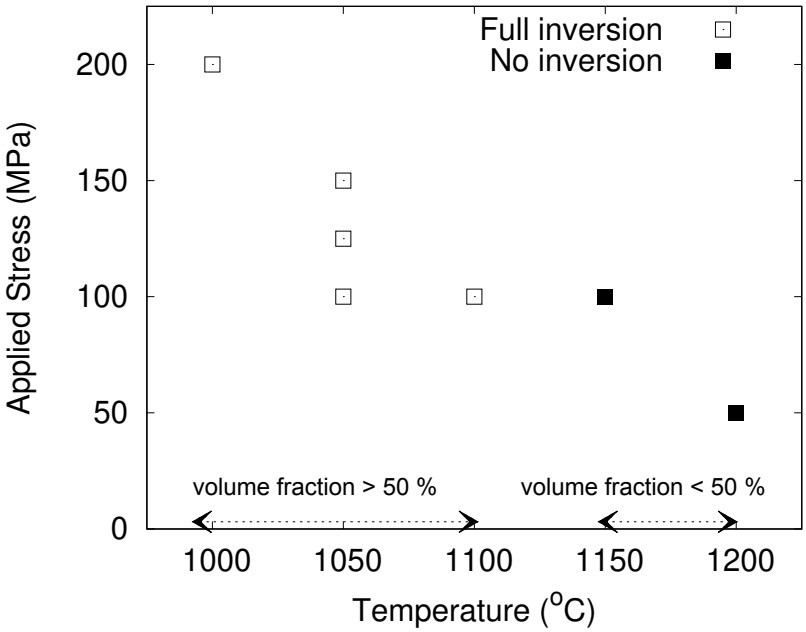

Figure 3.13: Outcome of high-temperature/low-stress creep conditions. Reprinted with permission from [1]

When $\gamma^{'}$ phase has a higher lattice parameter, the $\gamma/\gamma^{'}$ microstructure is said to have a positive misfit. On the application of a tensile load, the directional coalescence of the dispersed $\gamma^{'}$ phase happens parallel to the directional of applied load (P-type rafting). The anomalous microstructure

of the ruptured specimens with dispersed γ phase getting aligned along the loading direction could be explained on similar lines. Here in this case, before rupture, the microstructure is fully topologically inverted with the reversal of role between the γ and $\gamma^{'}$ phase. As the lattice parameter of the dispersed phase (γ) is higher than the matrix phase ($\gamma^{'}$), this is type of microstructure is similar to the P-type rafting of the dispersed phase. This behaviour is in fact in agreement with what was observed in TMS-75 alloy with 80$\%$ $\gamma^{'}$ and 20 $\%$ dispersed γ phases [106]. However, this aspect of microstructural evolution just before rupture is an issue that needs to be addressed more rigorously. Several experimental studies, especially for the class of alloys that exhibit topological inversion, needs to be performed to fully optimize the right $\gamma^{'}$ volume fraction for maximizing the lifetime.

3.4 Summary

The study aimed to better predict the microstructural evolution of Ni-based single crystal superalloys during a high-temperature/low-stress creep experiment using a newly proposed *Creep-Damage Phase-Field Model* that takes into account microstructural degradation, such as topological inversion. The present study involved formulating a microstructural damage density function based on the understanding that the initiation of the tertiary creep stage might be due to the destabilization of the $\gamma/\gamma^{'}$ interfacial dislocation network leading to the massive shearing of $\gamma^{'}$ rafts concomitantly resulting in topological inversion. In fact, the genesis of thought stems from the recent findings that the tertiary creep in Ni-based single crystal superalloys initiated before the expected increase in the volume fraction of pores. Subsequently, we proposed a generalized elasticity formulation in phase-field which is capable of predicting microstructural degradations during high-temperature/low-stress creep experiments. We adopted a simplistic mechanistic approach of considering microstructural degradations through explicitly modeling the precipitate softening alone and, thereby, implicitly accounting for plasticity dependent mechanisms in the tertiary creep. Here, the focus is on isolating the effect of voids from the current analysis and explain why it is also essential to consider microstructural degradation, if not critical, as an important damaging mechanism in the present material. The predicted microstructures and behavior traits in Ni-based single-crystal superalloys agreed with several experimental observations available in the literature.

In this context, for the first time, the complete microstructural evolution, including the topological inversion, is simulated using a phase-field model. Further, the phase-field simulated microstructures at various stages of the creep test were matched into the corresponding macroscopic crystal plasticity creep curves.

Several high-temperature/stress conditions were investigated to study the effect of volume fraction and damage kinetics of the topological inversion. The multi phase-field model, even though usually adept at predicting the aging and directional coarsening under the influence of external loads observed, failed to capture the loss of coherence of the microstructure during the secondary and tertiary creep stages. It was, therefore, deemed unfit for the prediction of complete microstructural evolution during high-temperature/ low-stress creep. The creep-damage phase-field model, formulated using a damage mechanics approach by considering the microstructural degradation as damage, on the other hand, was able to predict well rafting and topological inversion. The topological state of microstructures was quantified using the ratio of termination densities of the γ and the $\gamma^{'}$ phase.

The study also predicts that the topological inversion occurs only when the volume fraction of the $\gamma^{'}$ phase is above 50% as illustrated in Fig. 3.13. For superalloys having volume fraction close to 50% and above, the onset of topological inversion was found at the transition from secondary creep stage to the tertiary creep stage. Thus, the initiation of the tertiary creep stage is found to be also associated with the destabilization of the coherent $\gamma/\gamma^{'}$ microstructure. The ruptured specimens having $\gamma^{'}$ volume fraction of 60% or more was found to have the dispersed γ phase getting aligned parallel to the direction of applied load viz. P-type rafting. In general, fully inverted microstructures were observed in the tertiary creep stage for alloys with volume fraction 50% and above. This is in agreement with the experimental results of Caron et al [25]. For 1150°C/100 MPa with a $\gamma^{'}$ volume fraction of 41.2% and for 1200°C/50 MPa having a volume fraction of 28.6%, no rafting nor topological inversion was observed.

4. EFFECT OF MICROSTRUCTURE ON THE MACROSCALE PROPERTIES *

4.1 Background

In Ni-based single crystal superalloys, the macroscopic properties are intertwined with their complex bi-phased $\gamma/\gamma^{'}$ microstructure. This chapter aims to better understand the coupled effect of lattice misfit and microstructural state on the macro-scale performance by utilizing a faithful representation of the microstructure, via a phase-field model, as a starting point for the micromechanical model embedded in a finite-element crystal plasticity framework.

Mackay et al. [107] showed on a single-crystal Ni-Al-Mo-Ta alloy that rafted microstructures have smaller yield (at 0.2%) and rupture stresses in tension for temperatures ranging from 930°C to 1040°CC. The same qualitative results were obtained by Pessah-Simonetti et al. on the first generation Ni-based single crystal superalloy MC2 for a 650-950°C range [108]. The same temperature range was also investigated by Espié [109] to determine the effect of the microstructure on the monotonic and cyclic behavior for the AM1 alloy. If 650°C revealed no effect because of the shearing of the γ' particles independently of their shape, 950°C showed modifications. Espié tested the mechanical response of creep-obtained and cyclic-obtained (=2%) rafted microstructures to monotonic strain-controlled tensile tests at 9. 10-4 s^{-1}. Both rafted microstructures revealed smaller hardening at 2% than the cuboidal one. Contrary to Espié, who found no difference between creep-obtained and cyclic-obtained rafts in terms of softening, Gaubert [110] noticed that rafts obtained by cycling hardening lead to a more considerable softening compared to rafts obtained by creep. The difference might be due to the fact that Espié used samples aged at 950°C while Gaubert's were aged at 1050°C which means there is a significant difference in the $\gamma^{'}$ volume fractions and γ channel widths. Therefore, is it the widening of the γ channels or the

*Portions of this section are reprinted or adapted from two journal articles [3, 2]

modification of the lattice misfit or perhaps a mix of these two factors responsible for the above mentioned discrepancy in the softening behavior? The softening observed in the monotonic and cyclic mechanical responses for creep-rafted and cyclic-rafted microstructures is often interpreted as a consequence of the decrease in the Orowan stress, i.e., an increase of the γ channel widths. However, relaxation tests at 1050°C/$\epsilon_t = 1.2\%$ performed on an initially undeformed and on a creep-rafted (1050°C/150 MPa for 72h and 0.6$\%$ deformation) microstructure showed that the asymptotic value, i.e. the remaining internal stress, is 1.6 times higher for the initially undeformed specimen (120 MPa vs. 75 MPs) whereas the two tests started at the same stress magnitude [33]. One should expect that a deformed specimen would lead to a higher value of the internal stresses. If the difference in the γ channel widths (110 nm for undeformed vs 300 nm for rafted) is used to explain the smaller internal stress value of the rafted specimen, then it is important to note that the decrease in the Orowan stress should only be around 35 MPa at 1050°C. It is clear from these experiments that something else is at stake and that the difference in the lattice misfit is something that should be considered in the numerical calculations. Moreover, interpreting the changes in mechanical behavior with just the Orowan stress might be erroneous and deserves more detailed studies. Such studies would provide a better understanding on how internal stresses evolve and, therefore, on the evolution of the hardening variables employed in constitutive modeling, which could, for instance, allow for better predictions of size effects [111] that was attributed to surface relaxation effects on the lattice misfit during experiments on micro-pillars [112].

Micro-mechanical modeling is a way to answer to the overarching question asked in the previous paragraph. However, with the exception of the work by le Graverend and Harikrishnan [2], most micro-mechanical finite element simulations were performed with only one $\gamma^{'}$ particle or idealized $\gamma^{'}$ precipitate shapes [113, 114, 115]. This does not provide full confidence on the results knowing that the shape of the $\gamma^{'}$ precipitates depends on the value of the natural lattice misfit [41] and that precipitates will have different shapes between dendrite and interdendrite regions due to micro-segregations [116]. Therefore, it seems a dead end to study the effect of lattice misfit for certain microstructural states without having faithful representations of intricate $\gamma/\gamma^{'}$ microstructures

in all their details to account for realistic internal stress and strain distributions. The best approach to address this issue would be coupled phase-field crystal-plasticity models [117, 63, 118]. However, if such models are able to well predict rafting and to simulate macroscopic responses in certain conditions, they consider $\gamma^{'}$ as either elastic or deforming elastically due to a very large critical resolved shear stress, which seems in contradiction with what was experimentally observed [119]. In addition, these studies do not control equilibrium concentrations in the presence of plasticity, which is essential in the computation of the chemical free energy density, and consider constant misfit strains.

A much more reliable and straight forward approach for short thermo-mechanical loadings, i.e, loading conditions that do not trigger microstructure evolutions, would be to improve the formulation to the recent multi-scale approach employed by le Graverend and Harikrishnan [2], namely perform macro-scale finite-element calculations on realistic statistical volume elements (SVEs) obtained by phase-field simulations. On the one hand, this approach leverages the advantages of both phase-field and finite-element crystal plasticity models and, on the other hand, gives the flexibility to build and calibrate a robust micromechanical model connecting the two. Furthermore, averaging or homogenization-based approaches [120, 4] are sensitive to the volume fraction of the precipitates, but not to the shape differences in $\gamma^{'}$ precipitates owing to different lattice misfits considered in this study. The study will, therefore, use realistic 3D phase-field microstructures (cuboidal and rafted) with the experimentally consistent $\gamma^{'}$ volume fractions as well as shapes and distributions of the $\gamma^{'}$ precipitates at the envisioned temperature/stress conditions to simulate strain-controlled tensile tests up to 2% total strain and strain-controlled cyclic tests with $\Delta\epsilon_t = 2\%$ both at a strain rate of E-03 s^{-1}. This approach of utilizing phase-field SVEs in the finite-element crystal plasticity model has one major drawback: only short duration tests can be performed while the microstructure is essentially non-evolving. However, this drawback is not a limitation to the objective of the present study, which is to perform microstructure and lattice misfit sensitive micromechanical studies using monotonic and cyclic tests. This chapter aims to bring forth the importance of considering the effect of misfit strains in order to better understand the effect of microstructural state

on the macro-scale performance of Ni-based single-crystal superalloys.

It is important to hereby point out that a large range of natural lattice misfits, viz. from -0.2% to -0.5% , is investigated to be relevant with the large modifications of the lattice misfit during heat treatments, as shown in [121], and help the design of materials with improved performance. Thus, the changes in the natural lattice misfits are neither due to different chemical compositions nor temperature variations. Unlike [2], the present phase-field informed micro-mechanical model built into a crystal plasticity framework is sensitive to lattice misfit strain, the details of which are explained in detail in Chapter 2. Furthermore, it should be to emphasized that the lattice misfit values (natural and constrained) will be considered constant during the calibration and the FE simulations even though it is probably incorrect when such simulations last for a long time (>1300s). It is the reason why the FE simulations performed in this study are for short tests: 20s for the monotonic loading conditions. Considering that the lattice misfit does not evolve during short tests is twofold: 1) there is not enough time to trigger microstructural evolutions as well as to allow the $\gamma/\gamma^{'}$ interfacial dislocations rearranging to form a network and 2) the simulated thermo-mechanical loadings do not include softening. For fast thermo-mechanical loading, there is not enough time for the $\gamma/\gamma^{'}$ interfacial dislocations to rearrange into dislocation networks in order to accommodate the misfit.

4.2 Finite-Element Crystal Plasticity on Phase-Field Microstructures

A micromechanical model with a lattice-misfit-dependent isotropic hardening that takes a unique description depending on the phase: an Eshelby tensor (sphere or penny) for the precipitates ($\gamma^{'}$ phase) and a continuous medium for the matrix (γ phase) is proposed. Finite-element simulations of strain-controlled monotonic tensile were performed on a set of realistic 3D phase-field microstructures (cuboidal states and directionally coarsened rafted states) defined by their natural (undeformed) or constrained (deformed) lattice misfits and the width of the γ matrix channels. As the magnitude of the natural lattice misfit gets larger for the cuboidal microstructural states, the tensile test simulations predict smaller macroscopic yield stress and strain hardening as well as smaller stress triaxiality at the microstructure level. The model also predicts that having a more

pronounced rafted microstructure yields a higher stress triaxiality at the microscale. These insights allow to better understand the experimental studies that investigated the effect of microstructural states on the mechanical response during monotonic loading.

The cuboidal microstructures (which is a result of stress-free aging heat-treatment) and rafted microstructures (which is obtained from applying an external load on the cuboidal microstructures) are exported as SVEs into a finite-element crystal plasticity framework. For this, a three-dimensional simulation set-up of size 96x96x96 with a grid spacing of 30 nm is used for the phase-field simulations. While the grid spacing is set based on the necessary spatial resolution of interface (120nm) and precipitates (500 nm), the domain size is mainly limited by the computational resources. For a good-tradeoff between computational costs of 3D phase-field simulations with reliable statistics for the precipitate coarsening, we arrived at the present simulation box of size 96^3 and grid-spacing 30nm with an interface width of 4 grid points. Note that the width of the experimentally-observed $\gamma/\gamma^{'}$ interface is of the order of 100 nm when it is several microns for phase field simulations. Hence, it is also a limiting scenario when it involves exporting the voxel-data of phase-field into an FE mesh. So, the FE mesh (see Fig. 4.1) entirely depends on the grid resolution of the phase-field which came out to have 884,736 C3D8 elements in total, i.e. 912,673 nodes. The total number of degrees of freedom is 2,738,025 (sparse matrix size of 130,902,948).

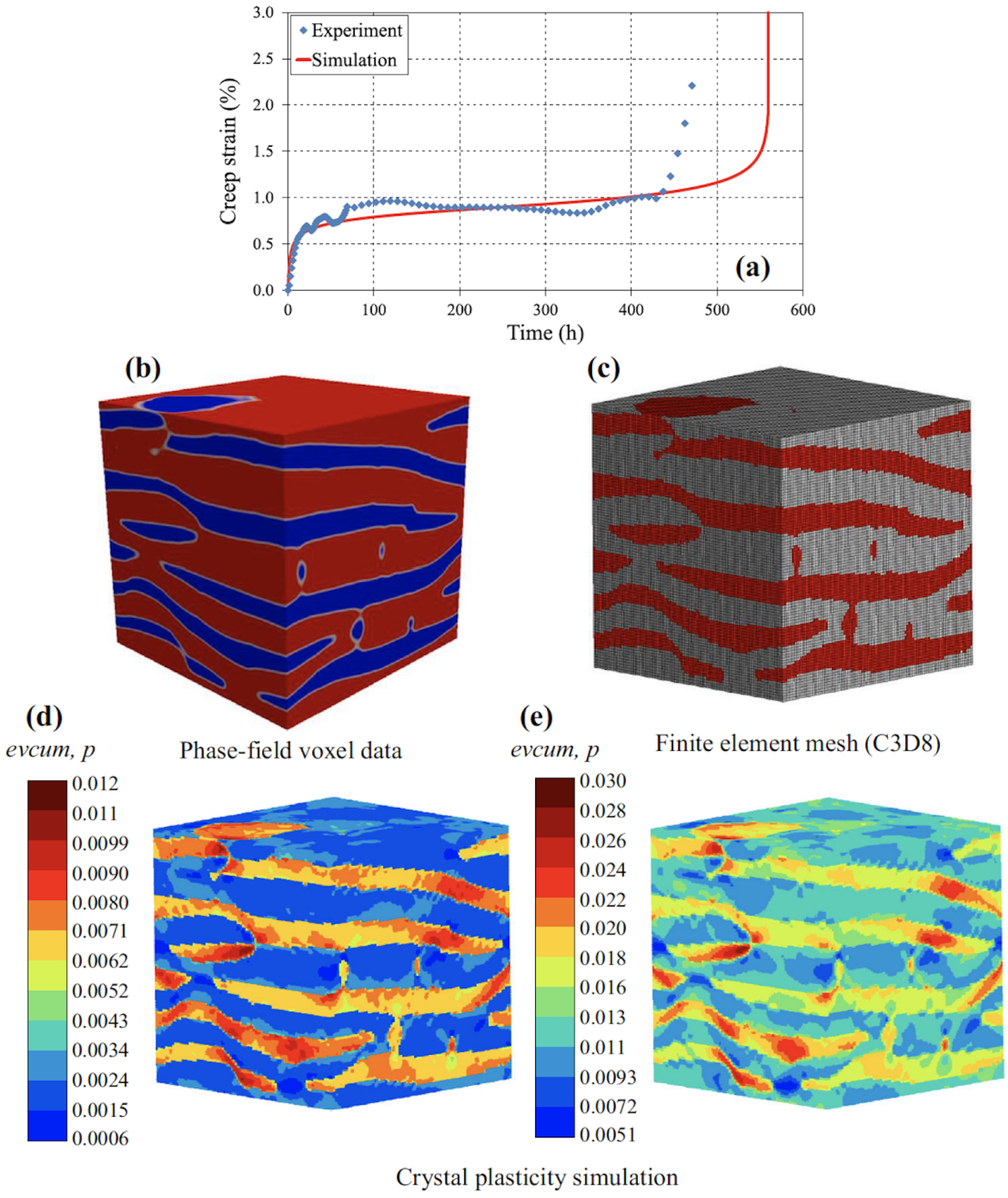

Figure 4.1: (a) Crystal plasticity simulation of a 1050°C/140 MPa creep test. (b) Phase-field voxel data for a fully rafted microstructure obtained by simulating a creep test at 1050°C/140 MPa. (c) SVE containing the finite element mesh obtained using the voxel data shown in (b). Accumulated plastic strain field at (d) t = 9.75 s and (e) t = 20 s for a fully rafted microstructure having a natural lattice misfit equal to 0.3%. Reprinted with permission from [2]

The aging conditions were simulated from explicit seeding of spherical nuclei using a quasi-random placement of nucleation sites and periodic boundary conditions that are maintained throughout the simulations. The simulation box used should be large enough to accommodate up to two orders of magnitude increase in the size of precipitates. When the precipitates reach the correct volume fraction (experimentally verified) for the given temperature conditions, one could only notice precipitate coarsening with fixed volume fraction. The aging simulation for initial cuboidal microstructures is continued until the side length of the precipitates reaches around 450-500nm.

	Elastic Constants (γ)			Elastic Constants (γ')			Elastic Constants(MC2)		
Temperature	C_{11}	C_{12}	C_{44}	C_{11}	C_{12}	C_{44}	C_{11}	C_{12}	C_{44}
(° C)	(GPa)	(GPa)	(GPa)	(GPa)	(GPa)	(GPa)	(GPa)	(GPa)	(GPa)
1050	154.1	102.1	63.8	154.6	98.6	68.6	153.8	100	69.2

Table 4.1: Stiffness components of the MC2 alloy and its phases at 1050°C

Phase	n	k	C_v	r_0	Q	b	C	D
γ	4.5	200	1	20	2	68	38000	500
γ'	4.5	900	0.8	65	5	68	10000	2000

Table 4.2: Material parameters of the crystal plasticity model presented in section 2.2.1 at 1050°C

For taking this accumulated plasticity in the activated slip planes and in order to estimate the amount of plasticity in each slip plane. a 1D simulation using a CP model (having microstructure sensitive variables and damage parameters) was performed on a node using Z-sim This information will serve as the input for carrying out the regular "strain-controlled tensile tests" on FE crystal plasticity for the rafted SVE realizations. So the rafted configurations essential means they were in the creep-regime and hence accumulated plasticity on each activated slip-system should be considered before conducting the 'strain –controlled tensile tests' on the finite element crystal

plasticity framework. Obviously, this is not needed for conducting 'strain –controlled tensile tests' on cuboidal microstructures as they are stress-free as received microstructures in the true sense.

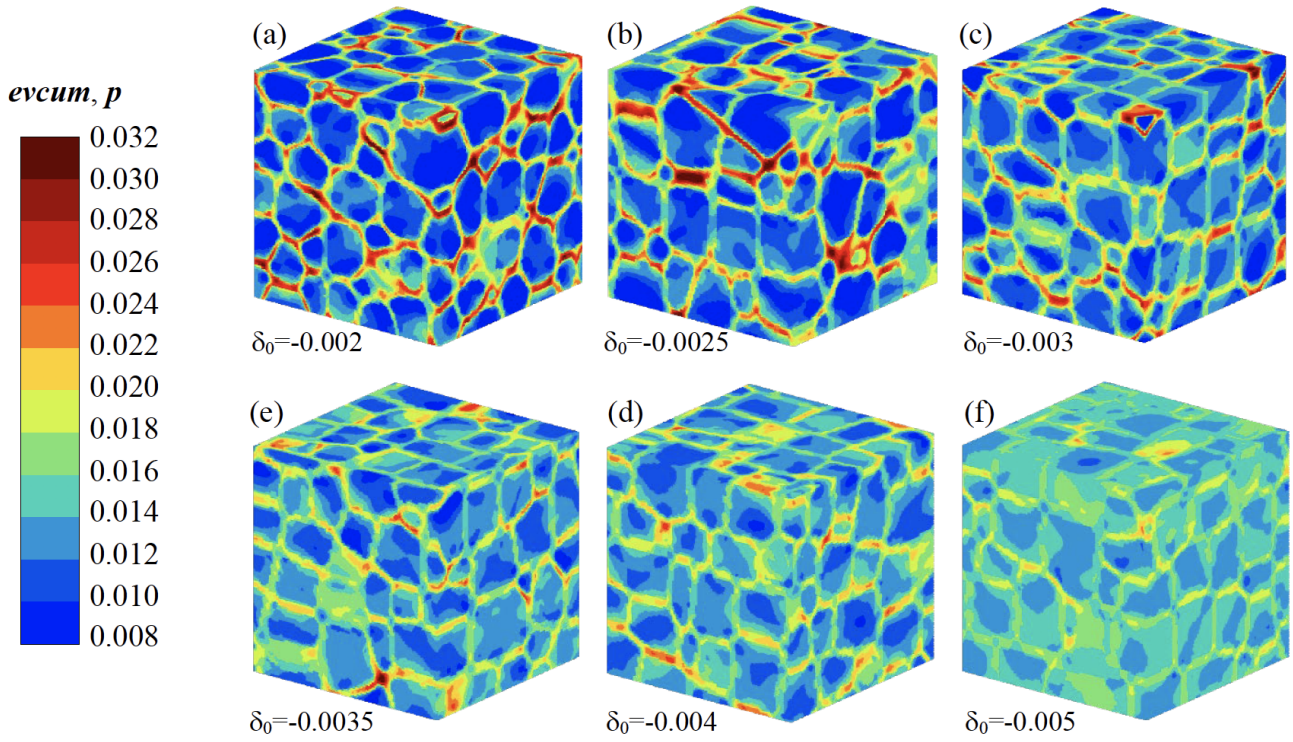

Figure 4.2: Accumulated plastic strain distribution at 2% total deformation after a monotonic tensile loading at 1050°C and $\dot{\epsilon} = 10^{-3}s^{-1}$ for the six natural lattice misfit configurations derived from phase-field. Reprinted with permission from [3]

To demonstrate the effect of precipitate shape on the macroscale response, six different natural lattice misfits, δ = -0.002,-0.0025, -0.003,-0.0035, -0.004, -0.005, to arrive at four differently shaped starting microstructures were utilized. Please note that natural lattice misfit is dependent on temperature and alloying elements. Here, even though the isothermal simulation temperature is kept constant at 1050°C, we are mimicking the effect of having different heat-treatments resulting in different natural lattice misfits. However, in all the phase-field simulations presented here, the elastic anisotropy is kept constant.

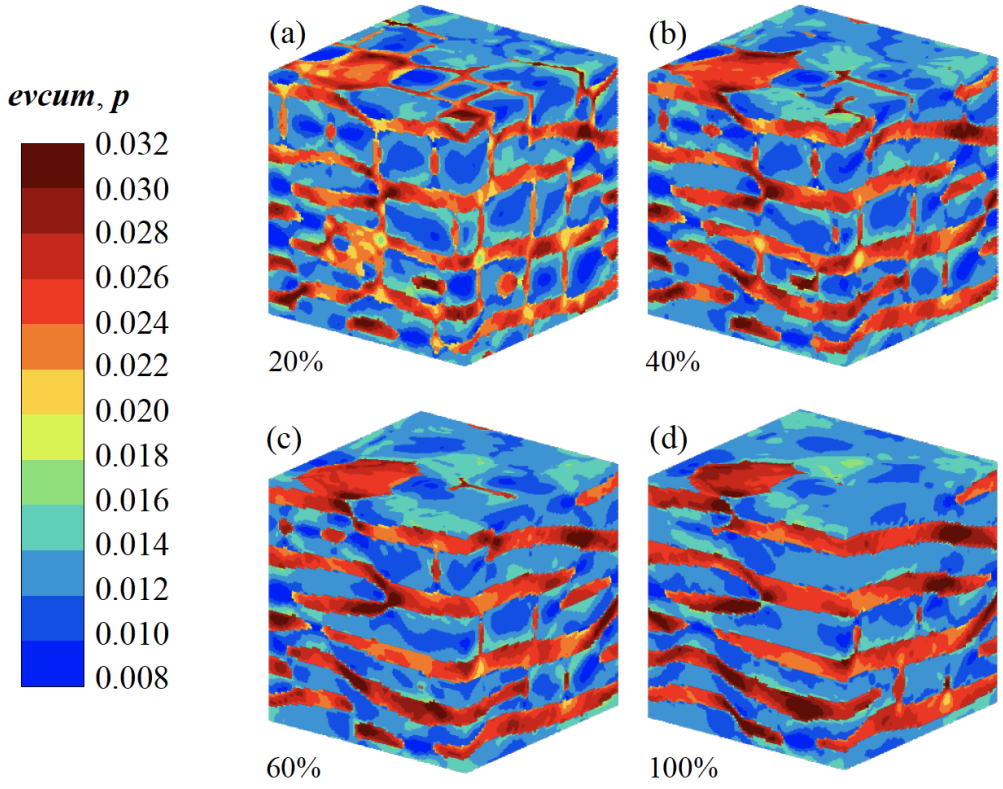

Figure 4.3: Accumulated plastic strain distribution at 2% total deformation for the four rafting realizations. Reprinted with permission from [3]

Comparing Figs. 4.2 and 4.3, it can be observed that the γ channels are a lot more deformed for the rafted configurations than the cuboidal one. This shows the effect of the pre-deformation due to creep that was used as an initial condition for the monotonic tensile test in rafting realizations. Fig. 4.2 shows the accumulated plastic strain distribution in the SVEs with different natural lattice misfit at 2% macroscopic total deformation, i.e., after 20 seconds. One can notice the spread of plastic deformation to the γ' phase increasing with the lattice misfit value. It is due to smaller isotropic hardening for larger lattice misfits leading to earlier deformation of the γ' phase. Furthermore, Fig. 4.2 shows that the horizontal channels are those with the highest accumulated plastic strain. This is consistent with what was obtained by Muller et al. [114] who did FE simulations with a viscoplastic model on a γ' precipitate with an idealized shape. Gao et al. [122] with DDD simulations at

room temperature for 800 MPa tensile loading also predicted higher average resolved shear stress in the horizontal channels for δ_0=-0.5%.

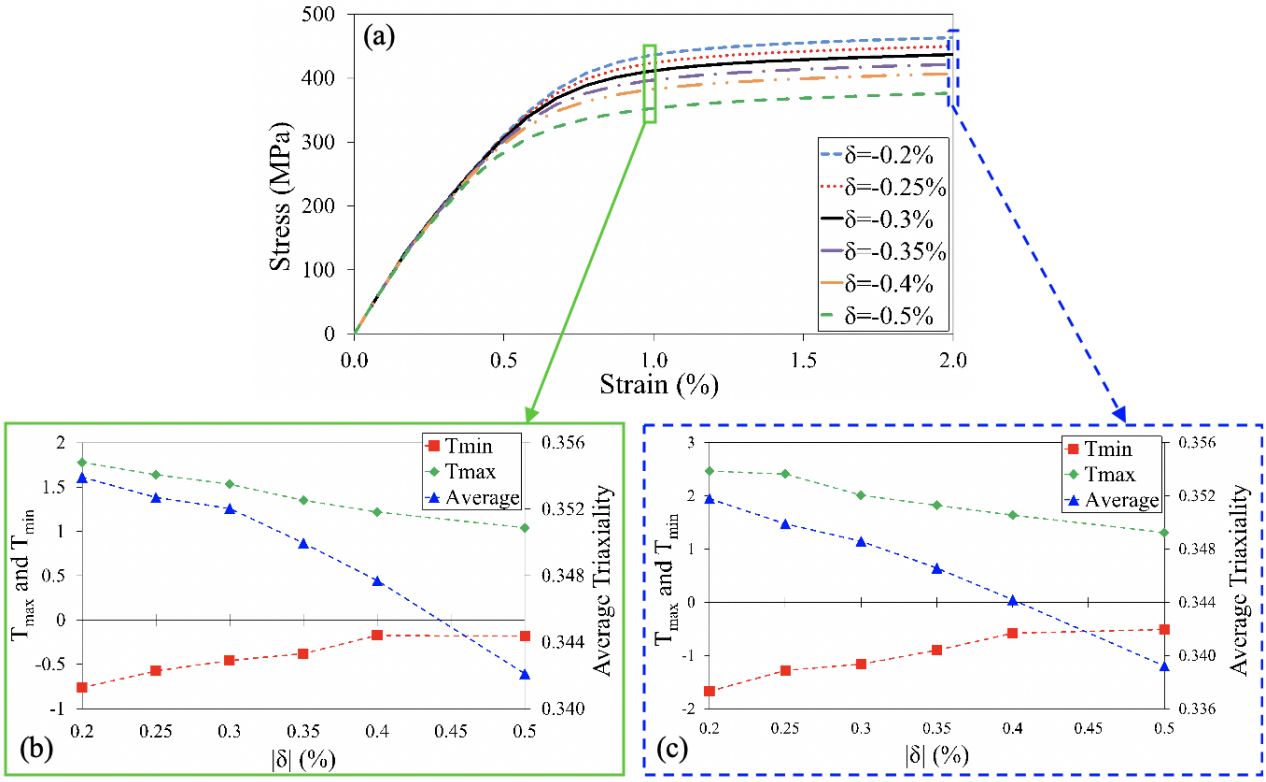

Figure 4.4: Monotonic tensile test simulations at 1050°C and $\dot{\epsilon} = 10^{-3}s^{-1}$ up to 2% for the four rafting stages extracted from phase-field SVEs:at 1% (b) and at 2% (c) the maximum, the minimum and the averaged triaxiality values are provided for each natural lattice misfit. Reprinted with permission from [3]

Figure 4.4 also shows the value of the minimum, maximum, and average triaxialities at 9.75s (Fig. 4.4 (b) and at 20s (Fig. 4.4 (c)). The average stress triaxiality in the volume decreases with the increase of the natural lattice misfit. Besides stress intensity, stress triaxiality is the most critical factor that controls the initiation of ductile damage [123]: the lowest the triaxiality is, the more ductile the mechanical response [124]. This trend, therefore, indicates that a specimen with a -0.5% lattice misfit should be more ductile. However, it is worth pointing out that Chen et al.

[125] showed that the elongation at rupture for a creep test at 1100°C/140 MPa is higher for the material specimen that previously had a heat treatment producing a larger lattice misfit. Therefore, the qualitative numerical result obtained at the microscale with a monotonic tensile test up to 2% total deformation seems to be consistent with the macroscopic experimental results.

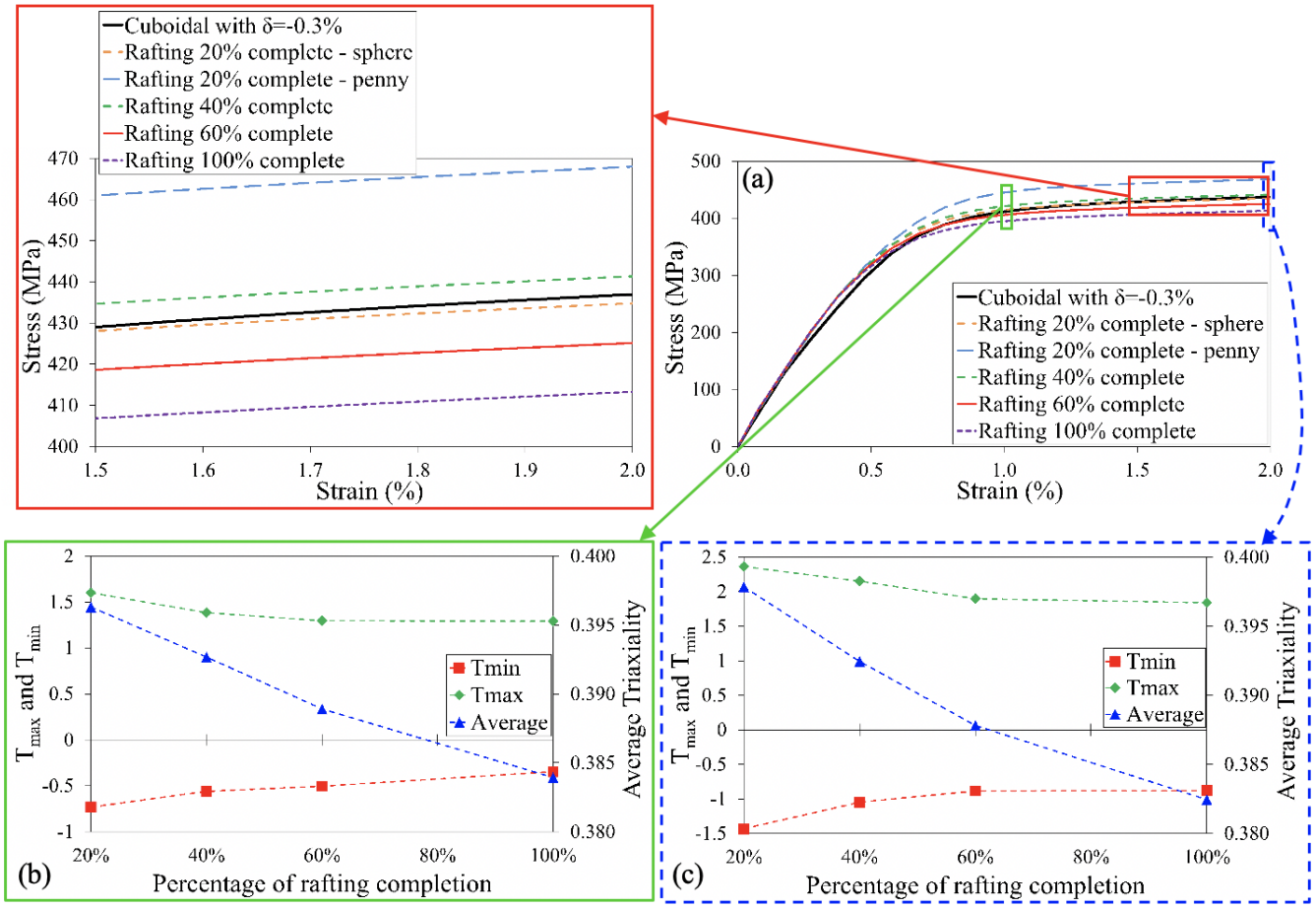

Figure 4.5: Monotonic tensile test simulations at 1050°C and $\dot{\epsilon} = 10^{-3}s^{-1}$ up to 2% for the four rafting stages extracted from phase-field SVEs. The maximum, the minimum and the averaged triaxiality values are provided for each natural lattice misfit at 1% (b) and at 2% (c) macroscopic total deformation. For the 20% -complete rafting stage, two versions of the Eshelby tensor were tried out: one that still consider that the precipitates are like spheres and the other one that the precipitates are already acting like pennies. Reprinted with permission from [3]

The same investigation was performed for different stages of rafting (see Figs. 4.5 and 4.3). To

be consistent with the initial rafted microstructures in phase-field creep simulations, the values of the internal state variables were estimated for each slip system and were used as an initial input to run the tensile test simulations on the rafted configurations. For that, a creep test at 1050°C/140 MPa was simulated on a node using Z-sim with a crystal plasticity model having a damage formulation and microstructure-sensitive variables [80]. For a 20% complete rafting, two simulations were performed: one considering the γ' precipitates as spheres and the second considering the γ' precipitates as pennies. The penny description brings softening to the mechanical response of rafted microstructures. If it is not obvious for 20% completion that corresponds to precipitates whose shapes are closer to spheres than pennies, it is for 60 and 100% completion. Indeed, the material was initially hardened by the creep test at 1050°C/140 MPa, which can be noticed by a larger yield stress. It is consistent with the results from Pessah-Simonetti et al. [108] who showed that a rafted microstructure (200h at 1050°C/80 MPa) is 140 MPa softer than an initially undeformed specimen at 2% for a strain-controlled tensile test at 950°C/1.1 E-04 s^{-1} on the MC2 alloy whereas the simulations in Figure 6 predict that the fully rafted microstructure is only 24 MPa softer than the cuboidal one. It is therefore important to point out that rafts have more effect on the mechanical behavior at 950°C than at 1050°C as well as for slower plastic strain rates, as shown by Gaubert [110] who investigated the effect of rafts obtained via creep at 1050°C/150 MPa for 72h on the mechanical behavior at 950 and 1050°C and for two plastic strain rates: 10^{-3} and 10^{-5} s^{-1}. Gaubert found a softening magnitude of the same order that the one obtained in Figure 6. Unfortunately, there is no data available on the effect of various rafting stages on the mechanical behavior, which would highly benefit the microstructure-lattice misfit uncoupling and, therefore, the modeling effort to better predictions of microstructure-gradient configurations. Fig. 4.5 also highlights that the triaxialities decrease with the percentage of rafting completion, which would mean that rafting brings more ductility. A result in contradiction with Pessah-Simonetti et al. [108] who found an average ductility of 11.6% for the aged samples while it was 16% for the unaged samples. However, the decrease in the ductility was attributed to the precipitation of μ-phase particles, known to quickly form at 1050°C [126]. Since the simulations do not capture the precipitation

of intermetallic phases, it would suggest that rafted microstructures are more ductile that cuboidal ones.

4.3 Summary

A phase-field-informed micromechanical model in a FE crystal plasticity framework was developed to study the effect of the lattice misfit (natural and constrained) of a $\langle 001 \rangle$-oriented Ni-based single crystal superalloy on the stress/strain distribution and the microstructure stress triaxiality during strain-controlled monotonic and cyclic tests at 1050°C/10-3 s^{-1}. 3D phase-field simulations were carried out for different lattice misfits to arrive at cuboidal and rafted microstructures. The different realizations of realistic phase-field microstructures were then exported as SVEs into a FE crystal plasticity framework. A new formulation for the isotropic hardening made the micromechanical model sensitive to the lattice misfit using a sphere- and a penny-type Eshelby tensor for the $\gamma^{'}$ precipitates when it is cuboidal and rafted, respectively. At the microstructure level and for the monotonic tensile test, the model predicted:

- smaller strain hardening for microstructures with larger natural lattice misfits;
- smaller stress triaxiality for microstructures with larger natural lattice misfit and more pronounced rafted states.

5. EFFECT OF CRYSTALLOGRAPHIC ORIENTATION

5.1 Background

Ni-based single crystal superalloys possess a strong processing-microstructure-property relationship that is a a function of the crystallographic orientation. During the grain selection process for manufacturing single-crystalline superalloys, the $\langle 001 \rangle$ direction is chosen as the preferred crystallographic growth direction as it provides the easiest and cost-effective solidification process along with a fairly good combination of properties when designed along with cuboidal $\gamma^{'}$ precipitates having a size of 450-500 nm [33] and volume fraction of 60-70$\%$[127, 33, 45, 44]. Controlling the single crystal orientation in a low modulus $\langle 001 \rangle$ direction and maintaining it parallel to the centrifugally loaded blade axis also minimizes the thermal stresses and improves the thermal fatigue resistance [128]. However, in reality, the intricate internal cooling channels and the strain grain formation near the single crystal seed region [129] result in casting inaccuracies leading to slight deviations from perfect [001]-orientations [40]. Furthermore, attaining a perfect parallel alignment of the blade axis with the centrifugal load is not always practically possible [45]. Even though misorientations up to 15° for certain applications[130] are within the permissible level, since each blade has a varying degree of misorientation, the mismatch between loading and crystallographic axes leads to a significant scatter in properties resulting in a mistuned-bladed assembly inside the aircraft engine [31, 32].

At the microstructural level, the pattern and orientation of γ' precipitates in the cuboidal state are different for each crystallographic orientation. During high-temperature/low-stress creep, the γ' precipitates directionally coarsen. The platelet-like rafts [35] in $\langle 001 \rangle$, the 45 degree rod-like rafts [35, 36, 37] in $\langle 011 \rangle$, and the irregular rafts [33, 38, 131] in $\langle 111 \rangle$ clearly suggests the sensitivity of microstructure evolution with respect to crystallographic orientations and their direct effect on the mechanical properties [37].

The elastic/viscoplastic behavior of the $\gamma/\gamma^{'}$ microstructure is highly sensitive towards the mis-

orientation. Experimental studies in the past showed that there was a significant deterioration of mechanical properties in DD6 single crystal superalloys when the misorientation exceeds about 10° [39, 40]. Sass et al. reported that even a small misorientation from the $[001]$-$[011]$ boundary of the stereographic triangle promotes extensive: single-slip on $\{111\}$ $<112>$ systems or coplanar-slip on $\{111\}$ $<110>$ systems resulting in higher primary creep strain and creep rates [41]. They also reported that the creep properties resulting due to small misorientations from $[001]$ and $[011]$ depends strongly on the direction of deviation[41], $i.e.$, the specimens with orientations near $[001]$-$[011]$ were found to have better creep strength compared to those with orientations closer to the $[001]$-$[\bar{1}11]$ or $[011]$-$[\bar{1}11]$ boundaries of the standard stereographic triangle [41, 42]. Moreover, the orientations near the $[011]$-$[111]$ boundary exhibited very short creep lives [33, 41]. Another experimental study [43] reported that orientations closer to the $\langle 100\rangle$-$\langle 111\rangle$ boundary display high primary creep, high ductility, and low rupture life. In short, even a slight crystallographic misorientation or misalignment of load axis can cause significant deviations from the expected microstructural evolution in Ni-based single crystal superalloys. As the stability of the microstructure dictates the structural integrity of the blades, it is vital to consider misorientations and quantify their effect on the creep performance. Though there have been many experimental studies on the effect of crystallographic orientations [33, 37, 44], very little has been studied on the effect of misorientations on the microstructural evolution in Ni-based SX superalloys[41, 45]. Hence, it is of prime importance to study the effect of misorientations on the microstructural evolution and quantify the strong microstructure-property relation with regards to the crystallographic misorientations in Ni-based SX superalloys.

Many studies were carried out in the past to understand the effect of crystallographic orientation on mechanical behavior of single crystal superalloys [132]. Lukas et al. [133] studied its effect on creep at 950°C on the CMSX-4 and found that the creep resistance decreases according to the following order $\langle 111\rangle$, $\langle 001\rangle$, and $\langle 011\rangle$. However, in the case of compressive creep, the order is different; as in, $\langle 001\rangle$ have a better resistant than $\langle 111\rangle$. Mackay et al. obtained the same trend at 765°C [134]. For low-temperature/high-stress creep conditions, a primary mis-

orientation of the $\langle 001 \rangle$ improved the creep lifespan much more than a secondary misorientation that allows getting closer to the $[011]$-$[\bar{1}11]$ boundaries of the standard stereographic triangle [135, 136]. Many researchers verified the same dependence of the creep lifetime with the crystallographic orientation for higher temperatures (see [137, 138, 139]. Nonetheless, the effect of crystallographic orientation on lifetime is more pronounced at low temperatures (750-850°C) than at high temperatures (>900°C) [45, 140]. It is, however, important to point out that the above results are dependent on the γ' size. Caron et al. found that a precipitate size of 450 nm, known to yield an optimum creep life for <001>-orientation, drastically reduces the stress-rupture life in the case of $\langle 111 \rangle$-oriented specimens: 36h instead of 1138h at 760°/750 MPa [33]. On the other hand, γ' precipitates with 230 nm significantly improved the strength of $\langle 111 \rangle$-oriented specimens: 1203h instead of 412h. Besides, it is interesting to point out that modifications of the anisotropy, known as Taylor rotation [141], which is the associated rotation of the lattice during creep testing [142, 143, 144, 145, 146].

Preparing single-crystalline superalloy specimens with various levels of precise misorientations and quantifying the degree of misorientations and co-relating it with the resulting microstructural evolution during the prolonged creep experiments is undoubtedly a daunting task. Therefore, there is a natural inclination towards theoretical and numerical modeling to understand microstructural evolution as a function of crystallographic orientation. The phase-field method, which is proved to be versatile on predicting the microstructural evolution in a plethora of complex alloy systems [30, 65, 68, 147, 148], has never been extended to study the effect of crystallographic orientations on γ' rafting in Ni-based single crystal superalloys. Despite knowing that orientations away from the main crystallographic directions have lesser creep strength, not many studies are dedicated to understanding the microstructural effects of misorientation [41]. Though there have been attempts in the past to study fragments of this topic using mesoscale phase-field models [35] and crystal plasticity models [142, 149], the scope has always been limited to a specific orientation with not much comprehensive reporting on the microstructural effects of misorientations. As there is a dearth of information on predicting microstructure based on a specific crystal-orientation as well

as experimental data for calibrating macro-scale crystal plasticity models, we tried to address this deficit by extending the present phase-field models[2, 1] to a generalized-crystallographic-sensitive phase-field model which could provide the complete microstructural evolution at any given point on the stereographic triangle.

In this work, for the first time, a crystallographic-sensitive phase-field method is developed to study the effect of crystalline orientations on the evolution of precipitate and channel morphology during aging and high-temperature/low-stress tensile creep. The study using realistic 3D phase-field simulations delves into elucidating the microstructural evolution and their stability as a function of misorientations away from the main three crystallographic directions as well as along the boundaries of the standard stereographic triangle. Furthermore, in order to compare the effects of different crystallographic orientations on the macroscale performance, 3D phase-field microstructural configurations were exported as statistical volume elements (SVE) into a finite-element(FE) crystal plasticity model. Strain-controlled tensile tests up to 2% strain at a strain rate of $\dot{\epsilon} = 10^{-3}s^{-1}$ were carried out in the 3D phase-field SVEs having cuboidal and rafted states with different crystallographic orientations. We believe the 3D phase-field informed FE crystal plasticity simulations presented here would as well instigate further studies and calibrations for modeling crystallographic reorientation, anisotropy, and lattice rotations that were not considered in this study.

5.2 Crystallographic-Sensitive Phase-Field Model

A three-dimensional simulation set-up of size 96^3 with a grid spacing of 30nm is used for the phase-field simulations. The elastic inhomogeniety, anisotropy and natural lattice misfit between the phases establishes the shape of the $\gamma^{'}$ precipitates during the heat treatment. A rotation matrix (R) for the sequence of three euler angles (ϕ, θ, ψ) rotation about each of the three principle axis, first along x axis, then along y axis, and finally along the z-axis as $R = R_z(\phi)R_y(\theta)R_x(\psi)$.

$$\underline{\underline{\boldsymbol{R}}} = \begin{bmatrix} c_\phi c_\theta & c_\phi s_\theta s_\psi - c_\psi s_\phi & s_\phi s_\psi + c_\phi c_\psi s_\theta \\ c_\theta s_\phi & c_\phi c_\psi + s_\phi s_\theta s_\psi & c_\psi s_\phi s_\theta - c_\phi s_\psi \\ -s_\theta & c_\theta s_\psi & c_\theta c_\psi \end{bmatrix}$$

$$f^{Elastic} = \frac{1}{2}\left\{ \sum_{\alpha=1}^{N} \phi_\alpha \left(\varepsilon_\alpha^{ij} - \varepsilon_\alpha^{*ij} \right) R_{ij} C_\alpha^{ijkl} R_{kl}^T \left(\varepsilon_\alpha^{kl} - \varepsilon_\alpha^{*kl} \right) \right\} \tag{5.2.1}$$

Once the Euler angles for a particular orientation are known, the corresponding rotation matrix, $\underline{\underline{\boldsymbol{R}}}$, to rotate the stiffness and Eigen strain matrices. The elastic driving forces will be modified as given in 5.2.1. Due to symmetry, there are usually more than one set of Euler angles describing the same crystal orientation. As explained by Gert Nolze in [150], a seemingly unique orientation definition represents only one of 24 possible but equivalent descriptions of the same orientation. Therefore, for each crystal orientation that is defined here by a set of Euler angles, there can be 23 additional sets of Euler angles present [151]. The 3D phase-field simulations for various perfect orientations and misorientations were simulated and then exported as SVEs into the finite-element crystal plasticity framework. To assess the macroscopic performance of various orientations, strain-controlled tensile tests were performed using the model on these realistic microstructures. The perfect orientations and misorientations investigated is indicated in the Fig.5.1. The material parameters for the phase-field model are given in the Table 5.1 below.

	Elastic Constants (γ)			Elastic Constants (γ')			Al concentration	
Temperature	C_{11}	C_{12}	C_{44}	C_{11}	C_{12}	C_{44}		
(° C)	(GPa)	(GPa)	(GPa)	(GPa)	(GPa)	(GPa)	γ Phase	γ' Phase
1050	202.3	149.8	91.1	234.1	177.2	93.7	21.1	25

Table 5.1: Phase-field parameters for Ni-based SX superalloys at 1050°C

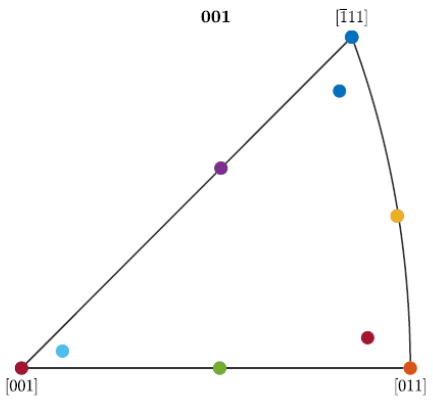

Figure 5.1: Stereographic triangle showing the cases that are investigated

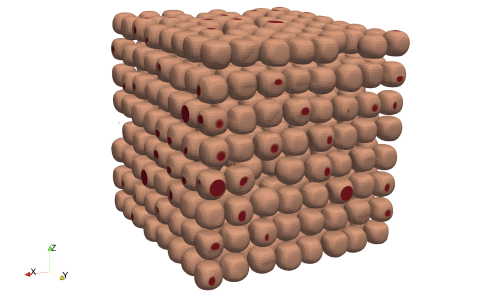

(a) Precipitation

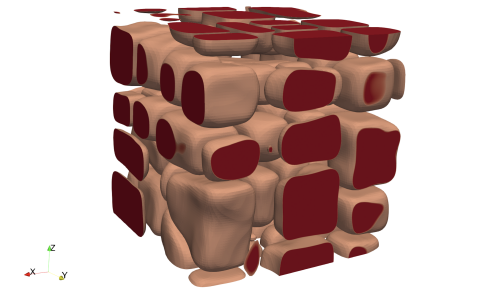

(b) Cuboidal state

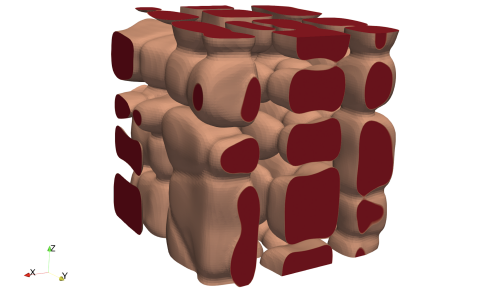

(c) Rafting stage

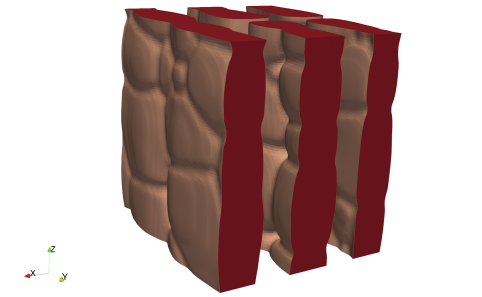

(d) Fully rafted microstructure

Figure 5.2: Complete microstructural evolution predicted for <001> for 1050°C. The γ phase is transparent. (a) precipitation stage (b) γ' became cuboidal after stress-free aging at at 1050°C (c) γ' rafting after being crept at 1050°C/140 MPa. Load is applied along X direction. (d) fully rafted microstructure

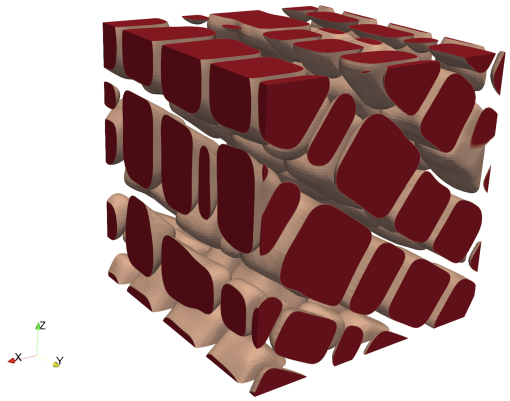

(a) Rafting stage

(b) Fully rafted microstructure

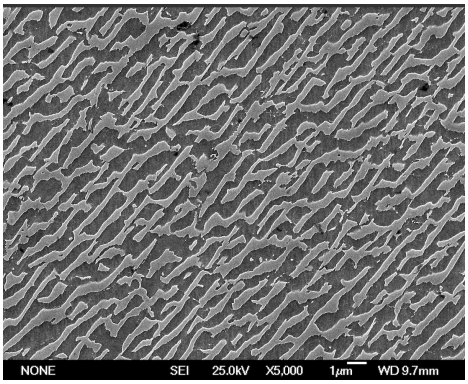

(c) SEM [011]-orientation

Figure 5.3: Microstructural evolution predicted for <011> at 1050°C. Creep loading at 1050°C/140 MPa is applied along X direction. (c) CMSX-4 crept at 1050°C/180MPa (after 65 hours into the creep)

For the first time, a crystallographic-sensitive phase-field method is attempted to study the effect of crystalline orientations on the evolution of precipitate and channel morphology during aging and high-temperature/low-stress tensile/compressive creep. The study using realistic 3D phase-field simulations delves into elucidating the microstructural evolution and their stability as a function of orientations and 15° misorientations away from the main three crystallographic directions as well as along the boundaries of the standard stereographic triangle. Furthermore, in order to compare the effects of different crystallographic orientations on the macroscale performance,

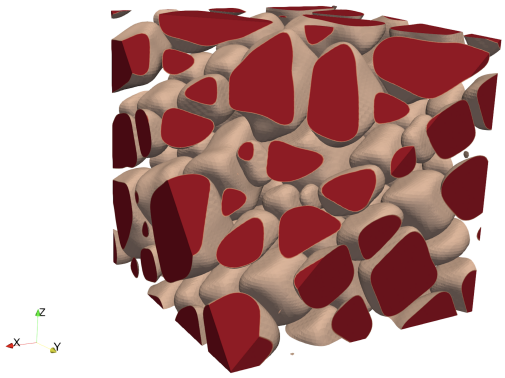

(a) Rafting stage

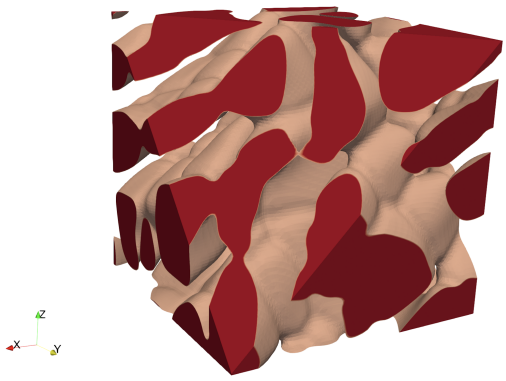

(b) Fully rafted microstructure

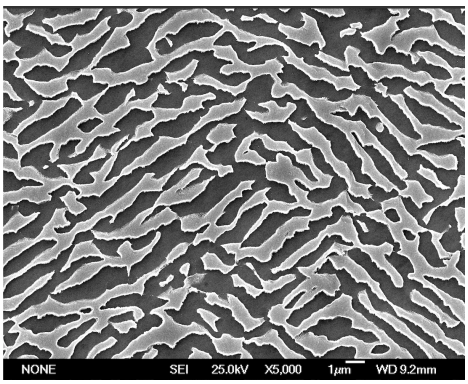

(c) SEM [111]-orientation

Figure 5.4: Complete microstructural evolution predicted for <111> at 1050°C. The γ phase is transparent. The 3D simulation box is sliced in the $\{111\}$ plane. Creep loading at 1050°C/140 MPa is applied along X direction. (c) SEM image is of CMSX-4 crept at 1100°C/140MPa (taken after 42 hours into the creep)

3D phase-field microstructural configurations were exported as statistical volume elements (SVE) into a finite-element(FE) crystal plasticity model. Strain-controlled tensile tests up to 2% strain at a strain rate of $\dot{\epsilon} = 10^{-3}s^{-1}$ were carried out in the 3D phase-field SVEs having cuboidal and rafted states with different crystallographic orientations.

The four stages in the microstructural evolution of a $<001>$ -oriented phase-field simulation of Ni-based single crystal superalloys is shown in Fig. 5.2. Here, aging simulation(no external stress) is stopped once the cuboidal precipitates on an average has side length of about 450-500nm. It is then followed by high-temperature creep (140 MPa applied along X-axis). Since, the applied stress is positive and lattice misfit is negative (-0.003), there is N-type rafting. For $<001>$-orientations, the euler angles are taken to be [0,0,0]. In the case of $<011>$-oriented superalloys, the euler angles were set to be [0,45,0] and for $<111>$, the euler angles were chosen to be [149, 54.74,45].

The phase-field model will be scrutinized with the SEM images of the cuboidal and rafted microstructures in $<001>$, $<011>$, $<111>$ crystal orientations. Fig. 5.3(e), shows the SEM image of a $<011>$-oriented CMSX-4 superalloy observed from $\{001\}$-plane after exposed to 65 hours at 1050°C/180MPa. The observation was made at from a sample extracted from the dendritic arm of the superalloy. The $\gamma^{'}$ precipitates have directionally coarsened 45-degree to the loading axis. In $<011>$-oriented superalloys, after the aging phase-field simulations, the cuboidal $\gamma^{'}$ precipitates were formed at angle of 45-degree (see Fig. 5.3(b)). Also, the formation of 45-degree tilted rod-like rafts can be observed during high-temperature/low-stress creep(see Fig. 5.3(d)) and is strikingly similar to what was found experimentally in Fig. 5.3(e).

Fig. 5.4(e), shows the SEM image of a $<111>$-oriented CMSX-4 superalloy observed from $\{011\}$-plane after exposed to 42 hours at 1110°C/140MPa. This observation was also made using a sample extracted from the dendritic region. The phase-field simulation of $<111>$-orientated superalloys at 1050°C/140 MPa closely resembles the SEM observation. The plate-like rafts in $<001>$, the 45 degree rod-like rafts in $<011>$, and the irregular coarsening in $<111>$ as seen in As seen in Figs. 5.2, 5.3 and 5.4 clearly suggest the sensitivity of microstructural evolution with respect to crystallographic orientations. The $[001]$, $[011]$, and $[111]$-oriented microstructures obtained

by phase-field simulations (under aging and creep conditions) agreed well with the experimental characterizations.

The number of slip systems is the same for both octahedral and cubic slip systems. For <011>, there are 4 octahedral slip systems and 4 cubic slip systems that were activated. However, the 4 cubic slips has a Schmid factor smaller that of the octahedral slips which lead to an activation that is sooner than that for <001>, thereby, resulting in very effective dislocation hardening.

The phase-field microstructures are then exported to FE Crystal Plasticity framework for performing macroscopic strain-controlled tensile tests. (see Fig. 5.5 and Fig. 5.6). The results predict that, in general, cuboidal microstructures have more yield strength compared to the rafted ones. This result is consistent, as it is know experimentally that rafting is a damaging process. Further, it was shown that <001>oriented microstructures have higher yield strength compared to <011> and <111>.

Further, misoriented microstructures in the <001>-<011>, <001>-<111> and <011>-<111> boundaries were simulated and compared against each other. It was found that the misoriented microstructure in the <001>-<011> boundary showed higher yield strength than <001>-<111> and <011>-<111> boundaries (see Fig. 5.6).

5.3 A Viscoplastic Crystal Plasticity Model with 3D Description for Rafting

During isothermal creep conditions with constant γ' volume fraction, the directional coarsening of the γ' precipitates in the vertical direction means a reduction of the precipitate width in the horizontal direction and an associated widening of the vertical γ channels. From the 3D phase-field results presented so far, it is now clear that rafting progresses differently in different orientations. The three dimensionality of the rafting phenomenon is clear in <011> and <111> directions.

Most of the constitutive models accounting for rafting on the mechanical behavior make use of a scalar parameter to describe the width of the γ channels, except Tinga et al. [152] who introduced a vector and by Desmorat et al. [38] who introduced a tensor. However, the previous attempts at describing the rafting using constitutive models [152] and tensorial descriptions [38] did not consider the evolution of γ channels in all three directions. Understandably, there does not exist

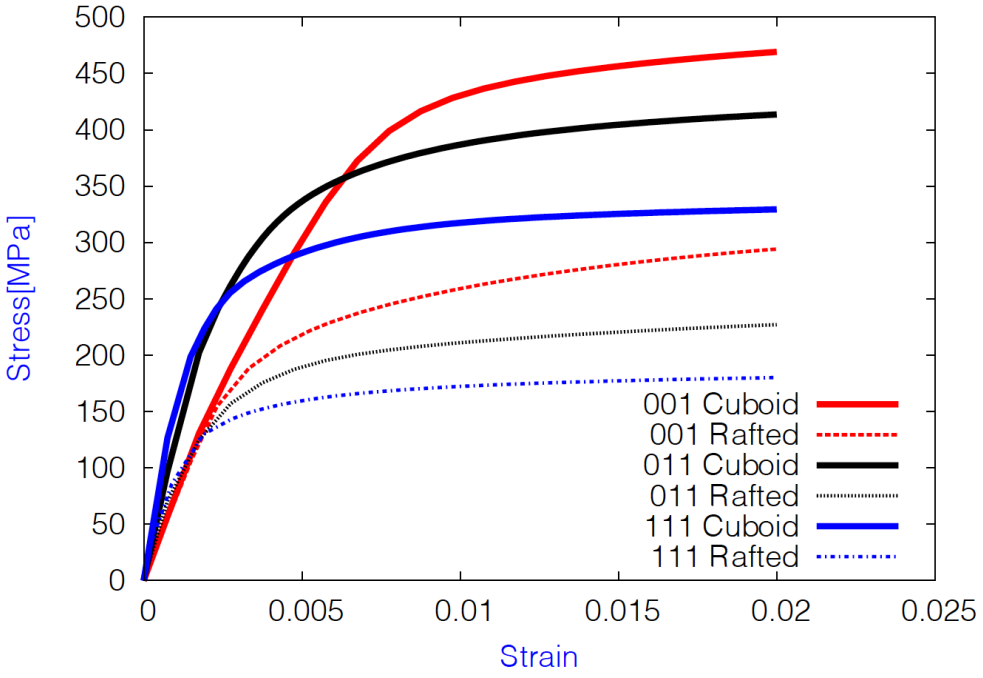

(a) Monotonic tensile tests at 10^{-3} $s^{-1}/1050°C$ for perfect orientations

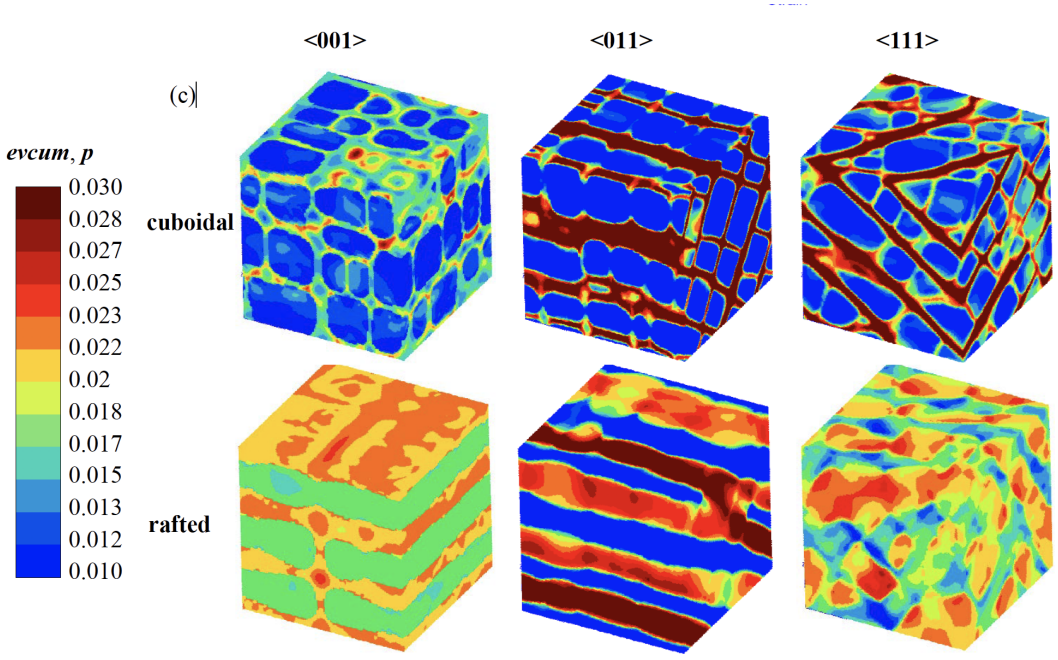

(b) The accumulated plastic strain distributions at 2%

Figure 5.5: Results from the strain-controlled tensile tests using the phase-field informed FE crystal plasticity framework. (a) Monotonic tensile test results for cuboidal and rafted cases for the perfect orientations. (b) Plastic strain distribution in the γ and γ' phases

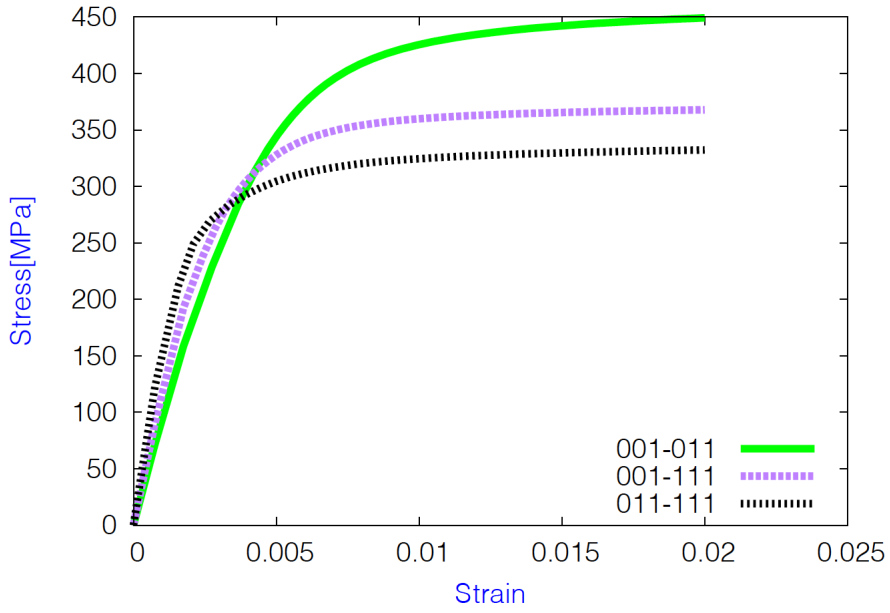

Figure 5.6: Monotonic tensile tests at $10^{-3}s^{-1}$/1050°C for misoriented for cuboidal microstructures

an in situ method that could be utilized to perform continuous tracking of the gamma channels. For instance, even though, X-ray and neutron diffraction techniques provides information such as γ' volume fraction [104], the constrained lattice misfit [153, 154], and the Young's modulus of the separate phases [155], it is, however, not possible to utilize any of these techniques for a proper continuous tracking of the channel width.

Tinga et al. [152] formulated their vectorial expression as a function of the diagonal components of the deviatoric stress tensor and the von Mises stress. The deviatoric stress components define the relative growth in the three directions. Tinga's formulation is, therefore, not valid for monotonic and cyclic loading conditions. Desmorat et al. [38] proposed a tensorial model similar to [4] in which a sum of an homothetic or LSW-type growth term due to the temperature, a mechanical coarsening term that is related to the spherical growth, and a directional coarsening term depending on a proportionality factor and on mean plastic strain direction. Even though Desmorat's model is based on a thermodynamic framework and is able to predict the overall evolution of the γ channels in the three directions and for different crystallographic orientation, the model predic-

tions in some scenarios do not seem physical, such as the piecewise evolution of the channels. Moreover, the model is restrained to just negative lattice misfits. Therefore, an advanced model is proposed with realistic physics-based calibrations using the 3D phase-field microstructures for different crystallographic orientations and stress levels. The present models using a phenomenological vectorial expression aims at modeling the evolution of the channels in the three directions and for any crystallographic orientations during both tensile and compressive creep. This formulation will build on the one developed by le Graverend et al. [4] and will, therefore, takes into account isothermal and non-isothermal modifications of the microstructural state.

Model Formulation and Results

le Graverend et al. [4] developed a microstructure-sensitive crystal plasticity framework with octahedral slip systems. This model is now extended to account for cubic slip systems, i.e., $\{001\}$ $<011>$ systems, to simulate crystallographic orientations away from the perfect $<001>$-direction. This constitutive model has a finite strain setting as in [74, 75, 76]. Again this model follows a micro-macro approach, meaning the relationships defining the elasticity are described at the macroscale whereas the viscoplastic constitutive equations operate within the microscale i.e., at the slip systems, more details of which can be found in [156, 4].

There are three possible factors controlling the γ channel width and that is considered in the rafting model:

- Homothetic growth of γ' precipitates due to high temperature conditions, which leads to a spheroidization of the precipitates and an isotropic coarsening. The homothetic growth is often modelled by the theory of volume-diffusion-controlled coarsening developed by Lifshitz and Slyozov [97] as well as by Wagner [98], known as the LSW theory,

- Directional coarsening of γ' precipitates due to dislocation motions inside channels which move preferentially in vertical or horizontal channels depending on the loading direction and the sign of the misfit [157],

- Dissolution/precipitation of γ' precipitates during non-isothermal loadings. The resulting

fine ' precipitates that are formed in the channels interfere with the propagation of dislocations, which was observed in [158, 159] during creep-fatigue loading at 1050°C.

Taking the above into consideration, the vectorial formulation for rafting is given as:

$$\underline{\dot{\boldsymbol{\omega}}} = \omega_0 \dot{\omega_T}\left(1 + \chi(\omega_D \underline{\boldsymbol{\omega}}_M) + \omega_I\right) + \omega_0 \omega_T \left(\chi\left[\dot{\omega}_D \underline{\boldsymbol{\omega}}_M + \omega_D \underline{\dot{\boldsymbol{\omega}}}_M\right] + \dot{\omega}_I\right) \tag{5.3.1}$$

Here, $\omega_D = \omega_D(T)$ takes into consideration the effect of diffusion while $\omega_I = \omega_I(T)$ is a function that describes the evolution of γ channels due to isotropic coarsening. χ accounts for the differences in kinetics when the channels are closing. For instance, in compression, the kinetics of evolution of channel closing is slower. To know if a channel is suppose to close depends on whether the channel is in tension or compression and depends on the sign of the natural lattice misfit. The function given by $\omega_T = \omega_T(T)$ describes the relative width of γ channel as a function of temperature. $\underline{\boldsymbol{\omega}}_M = \underline{\boldsymbol{\omega}}_M\left(\underline{\boldsymbol{P}}_v, T\right)$ is a function describing the effect of mechanical loading on the channel width and also depends on the accumulated plastic strain in each direction as given by:

$$\underline{\dot{\boldsymbol{\omega}}}_M = \frac{\left(\frac{\underline{\dot{\boldsymbol{P}}}_v}{n_M}\right)\underline{\boldsymbol{P}}_v^{\frac{1}{n_M}-1}\left(1 + asinh(v_0\underline{\boldsymbol{\zeta}})\right) - \underline{\dot{\boldsymbol{\zeta}}} v_0 \underline{\boldsymbol{P}}_v^{\frac{1}{n_M}}\left(1 + \left(v_0\underline{\boldsymbol{\zeta}}\right)^2\right)^{-0.5}}{\left(1 + asinh(v_0\underline{\boldsymbol{\zeta}})\right)^2} \tag{5.3.2}$$

Here, $\underline{\boldsymbol{\zeta}}$ is an internal state variable which imparts a strain rate sensitivity: if the plastic strain rate is higher in a direction, then $\underline{\boldsymbol{\zeta}}$ along that direction would be large and prevents $\underline{\boldsymbol{\omega}}_M$ in that particular direction to have large values.

$$\underline{\dot{\boldsymbol{\zeta}}} = \left(\frac{\underline{\dot{\boldsymbol{P}}}_v^2}{\zeta_0} - \underline{\boldsymbol{\zeta}}\right)\underline{\dot{\boldsymbol{P}}}_v - \left(\frac{\underline{\boldsymbol{\zeta}}}{M}\right)^m \tag{5.3.3}$$

In the above equation, m, ζ_0 and M are temperature dependent material parameters. In this formulation, it is important to note that the definition of the accumulated plastic strain (usually a scalar) has been redefined as a vector as shown below:

$$\dot{\underline{\boldsymbol{P}}}_v = \begin{pmatrix} \sqrt{\frac{2}{3}\sum_{i=1}^{3}\left(\dot{\epsilon}_{1i}^{p_{rotated}}\right)^2} \\ \sqrt{\frac{2}{3}\sum_{i=1}^{3}\left(\dot{\epsilon}_{2i}^{p_{rotated}}\right)^2} \\ \sqrt{\frac{2}{3}\sum_{i=1}^{3}\left(\dot{\epsilon}_{3i}^{p_{rotated}}\right)^2} \end{pmatrix} \tag{5.3.4}$$

Therefore, $\underline{\boldsymbol{P}}_v$ expresses the accumulated plastic strain in each direction of the crystal or as per the "Natural Anisotropy Basis", as defined by Desmorat et al. [38]. Further, it is the reason why Euler angles description is used in the rotation matrix $\underline{\underline{\boldsymbol{R}}}$ in $\underline{\underline{\boldsymbol{\epsilon}}}^{p_{rotated}} = \underline{\underline{\boldsymbol{R}}}(\phi,\theta,\psi)\underline{\underline{\boldsymbol{\epsilon}}}^{p}\underline{\underline{\boldsymbol{R}}}^{T}(\phi,\theta,\psi)$. The 3D rafting model implemented in the viscoplastic crystal plasticity model gave good agreement of the channel width evolution with what was found using phase-field simulations (see Fig.5.7).

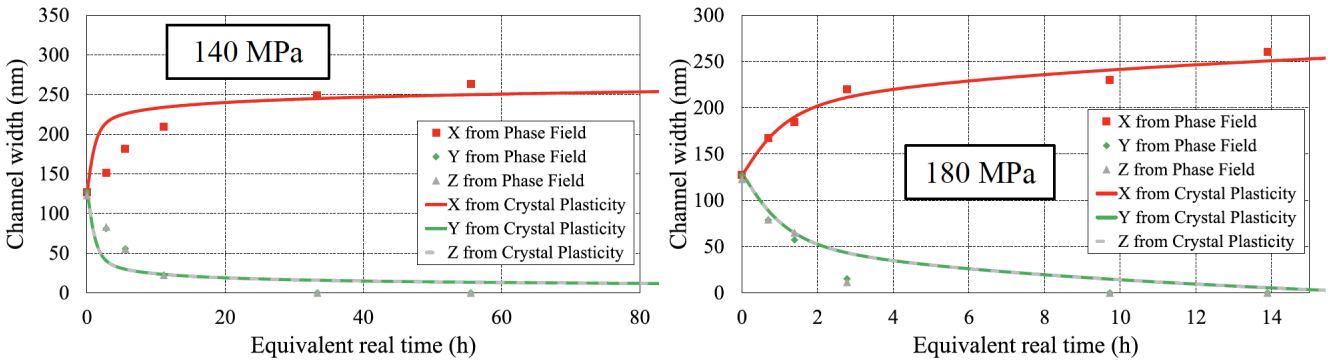

Figure 5.7: Evolution of the channel width using the 3D rafting model and comparison with the channel widths obtained by phase field simulations.

The model was also tested on an asymmetric notched specimen for 1050C/F=410N, i.e., 138 MPa. Fig. 5.9 shows the key fields at the end of the simulation, i.e., at failure. This result should be compared with what was experimentally obtained in [4]. On comparing Figs. 5.8 and 5.9, it is clear that the simulation results are consistent with what was found from the experiment performed by le Graverend et al. [4], thereby, validating the present model formulation. The same approach will

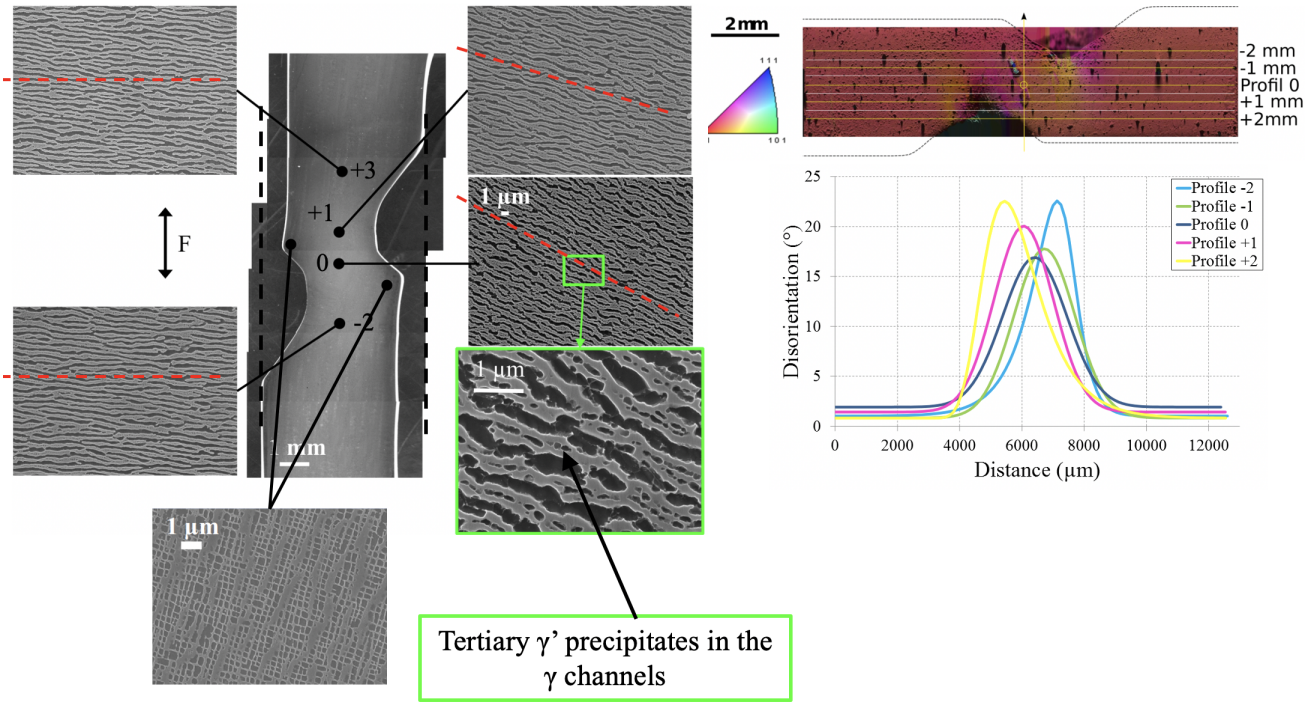

Figure 5.8: Experimental result showing the lattice rotations (adapted from [4])

be followed for different crystallographic orientations and could be extended for studying lattice rotations.

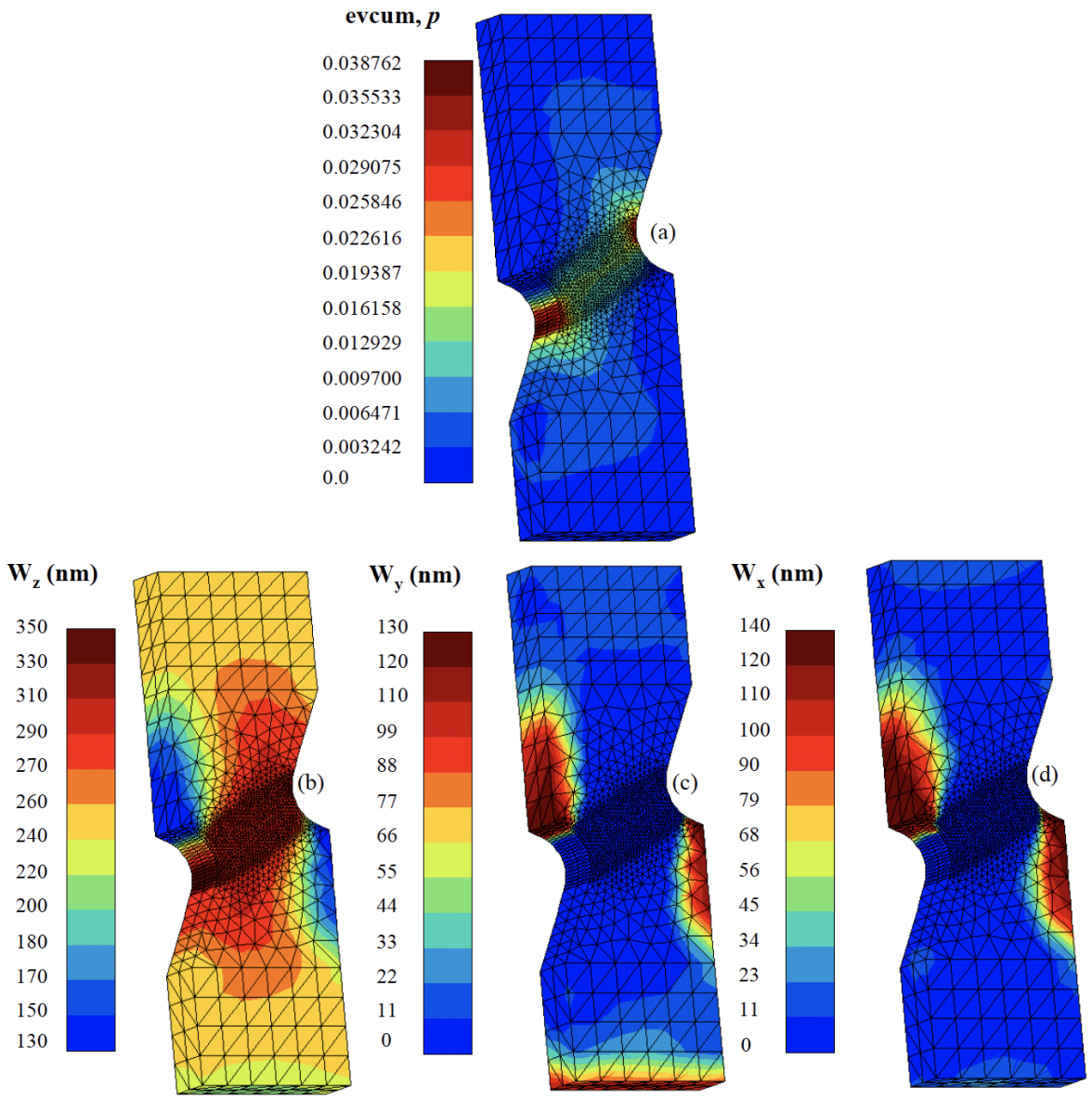

Figure 5.9: FEM simulations for the viscoplastic crystal plasticity model showing channel width evolution in three directions

5.4 Summary

While it is true that much of the attractive high-temperature properties of these Ni-based single crystal superalloys boils down to the coherent bi-phased γ/γ' microstructure and the stability of their interfacial dislocation network, the strong processing-microstructure-property relation with

regards to the crystallographic orientation plays an important role in the performance of the single-crystal turbine blades. To that end, a crystallographic-sensitive phase-field model was implemented and validated to predict the microstructural evolution in perfectly-oriented and misoriented single crystal superalloys. Later, these 3D microstructures from realistic phase-field simulations were exported to macroscale models finite-element crystal plasticity model to perform virtual strain-controlled tensile tests. The tensile tests results were then compared with different orientations. It was found that the misoriented microstructures in the <001>-<011> boundary showed higher yield strength than <001>-<111> and <011>-<111> boundaries. Also, for all the cases, cuboidal microstructure realizations predicted higher yield strength compared to the corresponding rafted ones.

A 3D rafting model was developed and calibrated using phase-field simulations. The model can predict the γ channel evolution during positive and negative creep. The model was able to predict the channel width for any crystallographic orientations due to a crystallographic-oriented accumulated plastic strain vector. The model was implemented to perform 3D crystal plasticity finite-element simulations and gave promising results that can ultimately be coupled with lattice rotations.

6. EFFECT OF MULTIAXIALITY

6.1 Introduction

A vast majority of the engineering components used for high-temperature applications contain cut-sections, holes, notches, and cooling channels. These geometrical features create regions of stress concentrations, making them most critical to the durability of the component. Due to the thermal gradients and complex cooling channels, the turbine blades, while in operation, experience complex stress states that are not homogenous throughout the single-crystal blade. During creep, the multiaxial stresses generated from the cut-outs and circular cooling channels redistribute in the material. Moreover, there has been evidence to show that even uniaxial creep conditions trigger lattice rotations, which ultimately impacts the kinetics and magnitude of rafting. Therefore, the microstructural instability associated with multiaxial stress states needs to be well-understood before coming up with numerical recipes for the damage modeling and life-prediction of Ni-based single crystal superalloys. Conducting a uniform state of triaxial stress requires a complex experimental setup. However, this problem could also be tackled through straightforward laboratory experiments by axial tensile loading a circumferentially notched specimen[160]. The notch promotes stress concentration and changes the stress state from uniaxial to multiaxial [161]. Further, by varying notch geometries, different multiaxial stress states can be carefully invoked in the laboratory specimens. Previous studies in the literature suggest that a notch could either have a weakening effect or a strengthening effect depending on the notch geometry and loading conditions. Studies on multiaxial creep deformation of single crystal superalloys previously demonstrated an order of magnitude increase in the lifetime of single crystal superalloys but at an intermediate temperature and high stresses [162]. However, creep testing at very low temperatures and very high stresses reduces the effect of notch sensitivity. Therefore, three different types of notches at four different stress conditions (160 MPa, 180 MPa, 200 MPa, 230 MPa) at 1050°C will be investigated here. The active slip systems mainly govern the anisotropy of creep behavior, which is also a function

of crystallographic orientation, loading conditions, and alloy composition. Conventionally, single-crystal specimens having simple symmetric orientations such as [001] and [111] are stable [163] and exhibits no orientation change after creep exposure while complex orientations or multiaxial stresses can result in large lattice rotations. Ardakani et al. [164] reported significant lattice rotations in [011] orientations while negligible lattice rotations in [111] and [001] oriented notch-free specimens. Basoalto et al. [162] on their double notched creep experiments at intermediate temperatures and high-stresses found a large change in orientation of about 20° varying across the specimen section. Therefore, it is interesting to understand how multiaxial stress states trigger lattice rotations during high-temperature/low-stress creep. The outcome of this study would lead to a better understanding of the degree of crystallographic orientations/lattice rotations contributing to anisotropic creep deformation.

6.2 High-Temperature Creep Experiments on Notched MC2 Single Crystal Superalloys

High-Temperature/low-stress creep experiments were performed on the first-generation MC2 single crystal superalloys. The nominal composition is listed in Table 6.1.

	Cr	Co	Mo	W	Al	Ti	Ta	Re	Hf	Ni
MC2	8.0	5.0	2.0	7.8	5.0	1.5	6.1	-	-	Bal

Table 6.1: Chemical composition (in weight %) of MC2 single crystal superalloy

Depending on the specifics of geometry and material, a notched circular specimen under uniaxial loading condition creates multiaxial stress states near the root region and a localized triaxial stress state within the notch region. All the creep tests presented here were tested at 1050°C.

Previous multiaxial experimental studies utilized double notch Bridgman creep specimens [162, 165]. The advantage of such a design is that one of the notches that is still intact after the creep rupture can be utilized for better microstructural characterizations. However, the two notches should not be placed close enough in order to avoid the stress fields from interfering with

each other. Testing such large specimens from commercial MC2 rods is also not economically viable, given the number of multiple creep tests with varying notch geometries and conditions were to be tested. Further, it is also essential to minimize the machining related surface roughness associated with intricate double notch designs. In the present study, for better compatibility with the creep bench design, a more conventional cylindrical single notch specimens were utilized instead.

The notched cylindrical specimens were machined according to the Bridgman's equation as given below:

$$T = \frac{1}{3} + ln\left(1 + \frac{a}{2R}\right) \tag{6.2.1}$$

In the above equation, T is the triaxiality factor, a is the minimum cross-section radius, and R is the notch radius. Using this criteria, several specimens having three different triaxialities, viz. 0.5, 0.84, and 1.0 were designed.

As there is a heterogeneous strain distribution at different parts of the specimen similar to what was documented and recommended in [165], total engineering strain $\left(\frac{\Delta L}{L_0}\right)$ of the specimens will be plotted against the elapsed time. Here, L_0 is the original gauge length of the specimen.

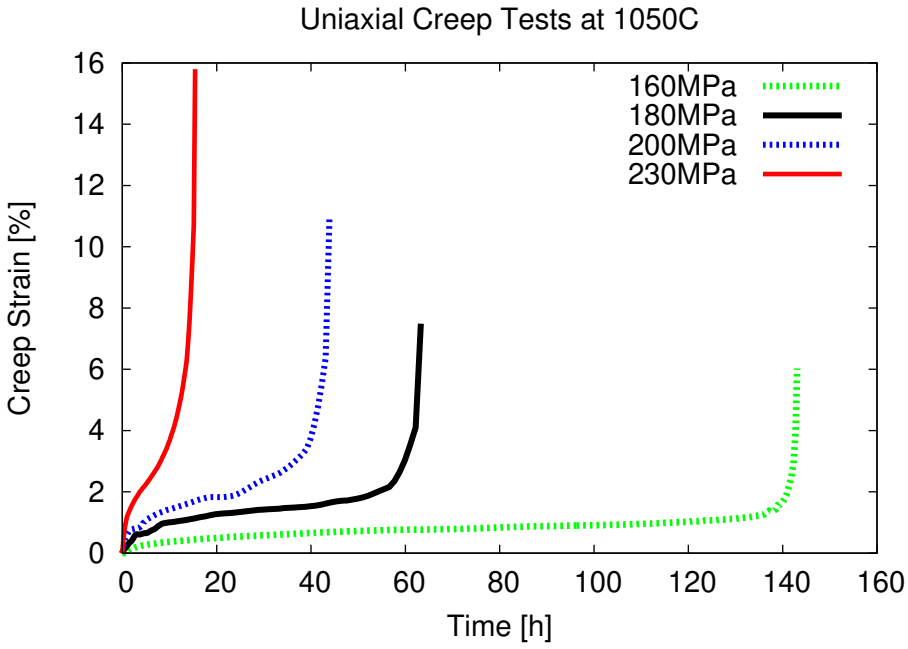

Figure 6.1: Creep data of uniaxial MC2 specimens extracted from [5] for four different stress conditions at 1050°C

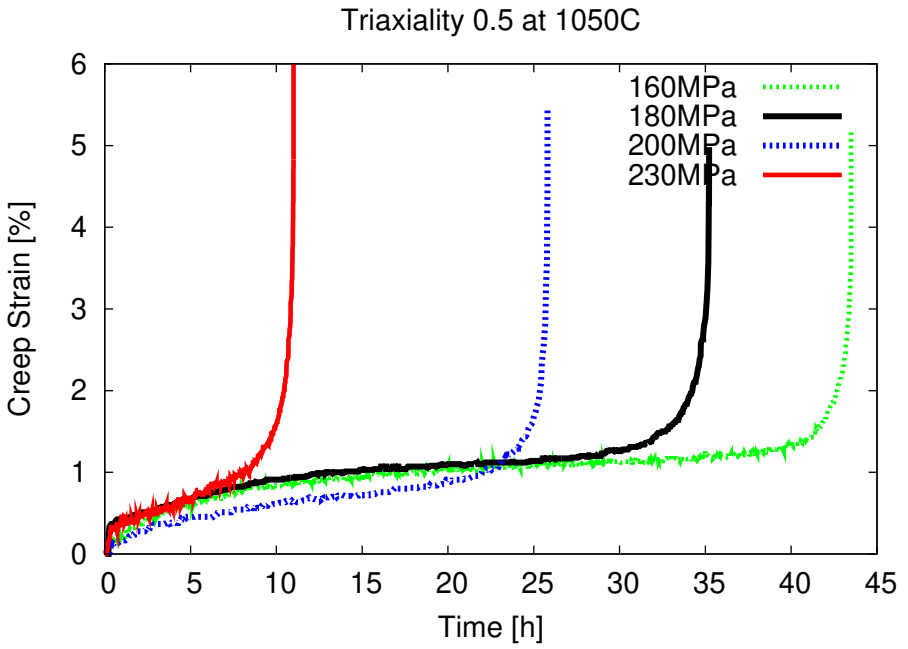

Figure 6.2: Creep data of notched MC2 specimens with a triaxiality of 0.5. At 1050°C, four specimens were tested at four different stress conditions

6.3 Experimental Results

The uniaxial creep data (see Fig. 6.1) was extracted from the studies conducted by le Graverend [5, 4] on [001]-oriented MC2 single crystal superalloys. The previous studies on the first generation superalloy MC2 suggest that for a uniaxial creep (conducted at 1050°C for stress conditions between 160MPa to 200MPa) suggests a constant and minimum steady strain rate for the secondary creep stage. Among the uniaxial creep tests presented here, the longest lifetime of 218 hours was recorded for the specimen crept at 1050°C/160MPa. The creep lifetime decreased drastically from 143 hours to 63 hours when the stress was increased from 160MPa to 180MPa. The specimen tested at 1050°C/230MPa failed after 15 hours marking the shortest creep life among the notch-free specimens. The highest rupture strain of about 16% was recorded for the same specimen crept at 1050°C/230MPa. le Graverend and co-workers [166] found that the lifetime of MC2 specimens is also limited by the presence of topologically close-packed phases (TCP) and pores.

The fracture surface of the notched specimens were observed under scanning electron microscope(SEM). Fig. 6.3 shows SEM micrographs of fracture surfaces of the specimen having a triaxiality of 0.84 exposed at 1050°C/160MPa. Fracture morphologies, on inspection, resemble typical ductile fracture.

	T=0.3			**T=0.5**	**T=0.84**			**T=1**
Conditions	t_r	rupture	t_r	rupture	t_r	rupture	t_r	rupture
(° C/MPa)	(h)	$\varepsilon(\%)$	(h)	$\varepsilon(\%)$	(h)	$\varepsilon(\%)$	(h)	$\varepsilon(\%)$
1050/230	15.4	15.8	11.0	6.0	16.2	3.22	11.9	3.27
1050/200	43.9	10.9	25.8	5.47	77.1	2.73	66.4	3.44
1050/180	63.3	7.49	35.2	4.98	105	3.14	209	1.68
1050/160	143.1	6.03	43.5	5.18	269.5	3.28	-	-

Table 6.2: Uniaxial and multiaxial creep data for all the investigated conditions. Time to rupture is denoted as t_r

The creep data from notched specimens with a triaxiality of 0.5 is presented in Fig. 6.2. The

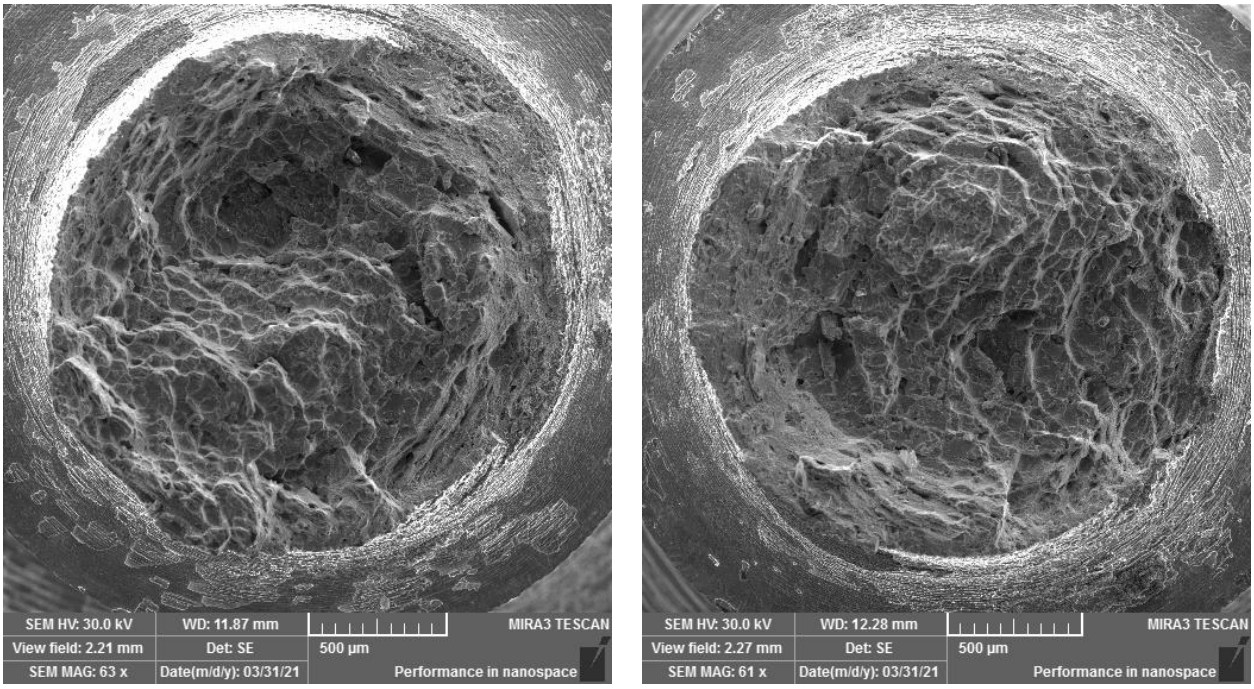

(a) Top rupture surface

(b) Bottom rupture surface

Figure 6.3: SEM micrograph showing the fracture surface of the specimen that ruptured after high-temperature creep loading. The micrographs shows top and bottom surfaces of notched specimen having a triaxiality of 0.84 exposed at 1050°C/160MPa for 269.5 hours.

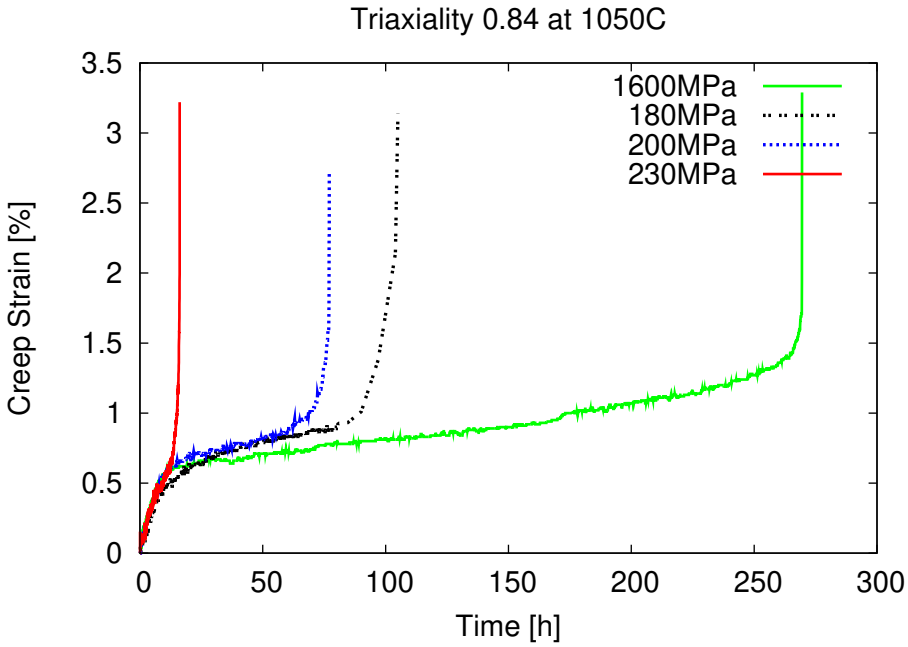

Figure 6.4: Creep data of notched MC2 specimens with a triaxiality of 0.84. At 1050°C, four specimens were tested at four different stress conditions

highest lifetime of 43 hours was recorded for the lowest stress condition, which is 160 MPa. The specimen tested at 230 MPa gave the highest rupture strain but lasted for only 11 hours. The highest to lowest creep lifetime trend seems similar to what was observed with the uniaxial specimens. However, one could observe a reduction in the creep lifetime in the notched specimens with T=0.5 for all the four stress conditions. Therefore, a distinctive notch weakening effect needs to be further investigated using microstructural characterizations and crystal plasticity studies.

A significant notch-strengthening effect can be observed in the creep data obtained from notched specimens with a triaxiality of 0.84. See Fig. 6.4 and Table 6.2 to compare the creep lifetime and rupture strains. Immediately after loading, an elastic/plastic stress distribution is established; as time progresses, the creep and damage formation cause stress redistribution in the notch[160]. Alternatively, in other words, the stress and rate of deformation are the highest initially and relax over time as steady-state is reached. Simultaneously, the plastically deformed regions in the notch root get constrained by an elastic core due to which the strain-controlled creep relaxation phenomenon

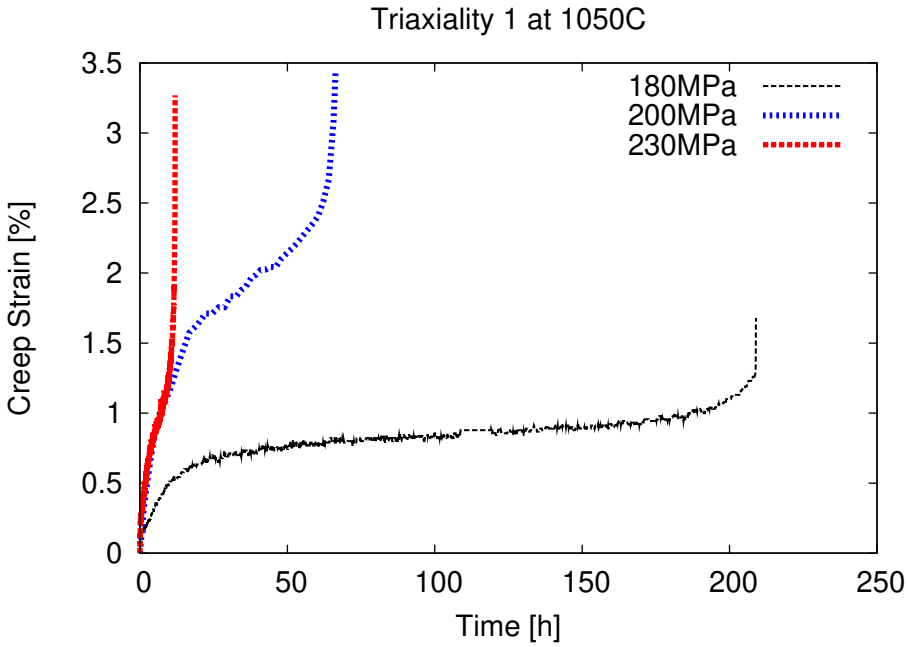

Figure 6.5: Creep data of notched MC2 specimens with a triaxiality of 1.0. At 1050°C, three different specimens were tested at 180MPa, 200MPa and 230MPa

will dominate the subsequent plastic flow[167].

In polycrystal alloys, it was found that the increased strain rates during tertiary creep will cause the axial stresses to redistribute[168]. However, this could not be true in the case of steep tertiary creep observed in MC2 superalloys and could explain why there was no notch-strengthening effect in the case of 1050°C/230MPa for specimens with triaxiality 1. According to Hayhurst et al. [168], magnitudes of the effective stresses and the magnitude of the multi-axial stress-state which causes damage determines the degree of stress redistribution. Therefore, the magnitude of rupture strain depends on the degree of stress redistribution that is governed by the sensitivity of the notch.

The notch-strengthening may be due to the constraint effect of the notch where some regions in the creeping notched specimen constrain each other leading to stress redistribution[161]. However, it is interesting to note from Fig. 6.6 that for among all the specimens tested at 1050°C/230MPa, there is little to no notch-strengthening. However, for lower stress conditions (1050°C/180MPa and 1050°C/160MPa), a notch-strengthening effect was observed for both specimens with triaxialities

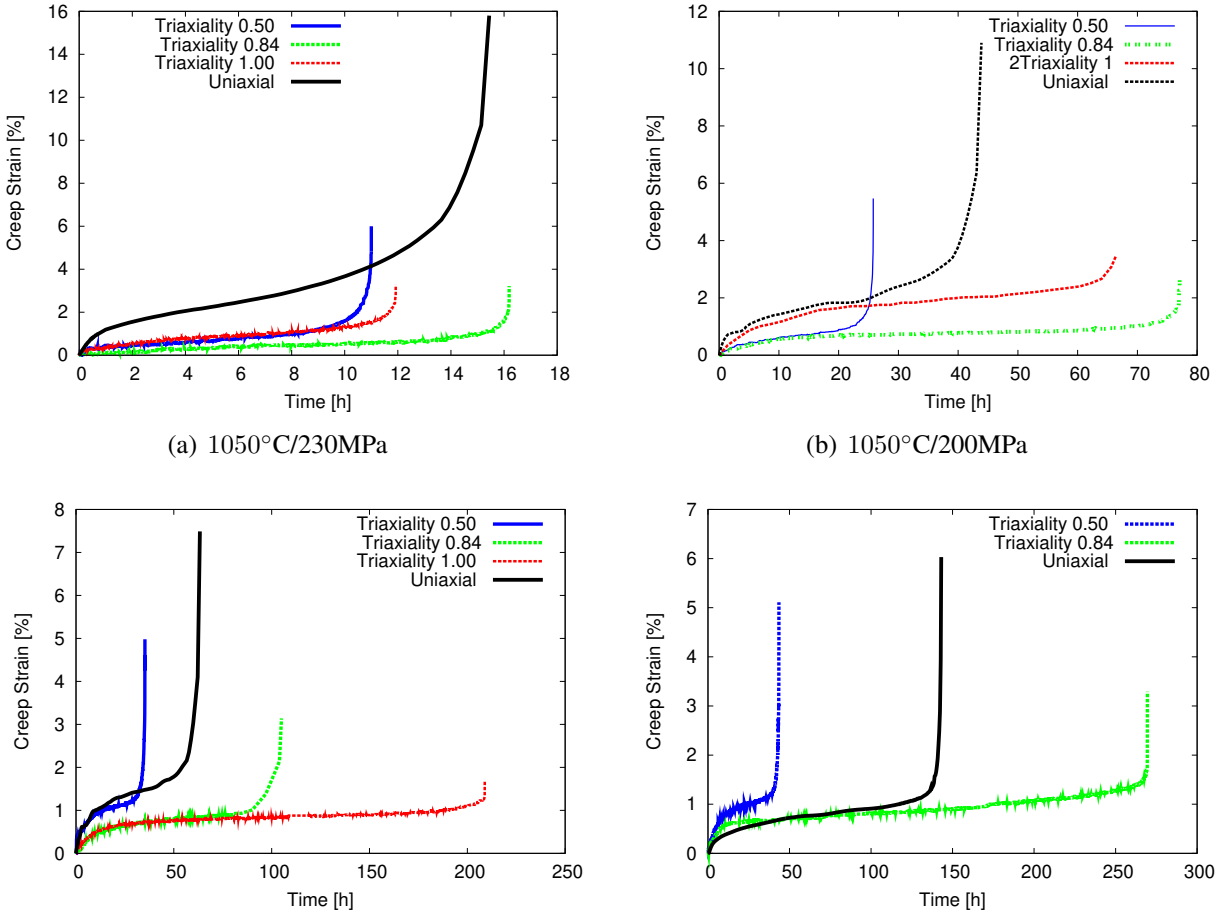

(a) 1050°C/230MPa

(b) 1050°C/200MPa

(c) 1050°C/180MPa

(d) 1050°C/160MPa

Figure 6.6: Comparison of uniaxial and multiaxial creep data investigated at 1050°C for (a) 230MPa, (b) 200MPa, (c) 180MPa, and (d) 160MPa

0.84 and 1.0 (see Fig. 6.6). Note that for T=1 specimen at 1050°C/160MPa, a notch-strengthening was observed (results not reported here). This comparison also sheds light on the sensitivity of the loading conditions for the notch strengthening/weakening effect. This can be further explained only by post-mortem EBSD analysis of the specimens to gauge the effect of lattice rotations on the creep damage in the notched specimens. It is to be noted that the stress redistribution may be less prominent at higher stresses but the shearing due to the notch-geometry could be possible leading to larger lattice rotations, especially for specimens with high triaxialities.

6.4 Summary

Several creep experiments were conducted on notched MC2 specimens to understand the effect of stress triaxiality on the creep lifetime of single-crystal superalloys. Specimens were crept at 1050°C for various stress conditions: 160MPa, 180MPa, 200MPa, and 230MPa. The results from notched tests were compared with notch-free specimens. All the specimens failed in the middle of the notch. A significant notch-strengthening effect was observed for specimens with triaxiality 0.84 for all stress conditions investigated here. For triaxiality 1, 1050°C/160MPa (not reported), 1050°C/180MPa and 1050°C/200MPa showed notch-strengthening effect. Additional creep tests needs to be performed to fully understand the effect of high triaxialities. A well-pronounced notch-weakening effect was observed for triaxiality 0.5. The stress redistribution mechanisms can be explained better using finite-element crystal plasticity simulations. What remains to be investigated is how the lattice rotations or initial misorientations in the specimen affects the creep lifetime of notched specimens. Only from detailed EBSD analysis, the effect of lattice rotations on creep deformation can be well explained.

7. CONCLUSIONS AND FUTURE WORK

7.1 Conclusions

Microstructural instabilities in Ni-based single crystal superalloys have been studied for many years. However, no general theory or framework can be applied to predict their material behavior irrespective of the given operating condition. From a practical standpoint, the high safety tolerance of these materials in structural applications such as turbine blades stems from the fact that the damage mechanics and mechanical behavior prediction of these materials are far from taken into confidence. This study aims at opening multiple perspectives of synergistic theoretical formulation, leveraging constitutive and microstructure-sensitive thermodynamic modeling and fundamental laboratory experiments together to answer some of the most pressing research questions related to the microstructural instabilities and their consequences. On the outset, the aim was to fill the gaps in the fundamental understanding of single-crystal superalloys and bring a few missing pieces in the literature together in order to explore the possibilities of coupling multiple numerical methods to build a robust scale-briding computational framework.

The work began with establishing a better prediction technique of the microstructural evolution of Ni-based single crystal superalloys during a high-temperature/low-stress creep experiment. An extension to the multi phase-field model was proposed that considers microstructural degradation, such as topological inversion, as damage. As a result, a Creep-Damage Phase-Field model was developed, which predicted, for the first time, topological inversion of the $\gamma/\gamma^{'}$ microstructure towards the end of the secondary creep stage. This study also explained why it is essential to consider microstructural degradation and not just pores, if not critical, as an important damaging mechanism in Ni-based single crystal superalloys. The predicted microstructures and behavior traits in Ni-based single-crystal superalloys agreed with several experimental observations available in the literature. Further, the phase-field simulated microstructures at various stages of the creep test were matched into the corresponding macroscopic crystal plasticity creep curves. Some

other significant outcomes from objective 1 are as follows:

- Several high-temperature/stress conditions were investigated to study the effect of volume fraction and damage kinetics of the topological inversion. The topological state of microstructures was quantified using the ratio of termination densities of the γ and the $\gamma^{'}$ phase.

- The study also predicts that the topological inversion occurs only when the volume fraction of the $\gamma^{'}$ phase is above 50%. For superalloys having volume fraction close to 50% and above, the onset of topological inversion was found at the transition from secondary creep stage to the tertiary creep stage. Thus, the tertiary creep stage initiation is also associated with the destabilization of the coherent $\gamma/\gamma^{'}$ microstructure. In general, fully inverted microstructures were observed in the tertiary creep stage for alloys with volume fraction 50% and above. This is in agreement with the experimental results. For 1150°C/100 MPa with a $\gamma^{'}$ volume fraction of 41.2% and for 1200°C/50 MPa having a volume fraction of 28.6%, no rafting nor topological inversion was observed.

The next step was to leverage the possibility of having realistic microstructures to perform micromechanical studies. Unfortunately, every single micromechanical model ignores the sensitivity of the complex $\gamma/\gamma^{'}$ microstructure. Most of the averaging or homogenization-based approaches are sensitive to the volume fraction of the $\gamma^{'}$ phase, but not to the shape differences in $\gamma^{'}$ precipitates owing to different natural lattice misfits. Or in other words, the existing models ignores the effect of microstructural states. In Chapter 4, this overarching problem was resolved using 3D phase-field microstructures as a starting point for the macroscale models. A novel technique of exporting the voxel data from the 3D phase-field simulations as SVEs into a finite-element crystal plasticity framework was put forth. For the first time, an attempt was made to perform a micromechanics-based FE crystal plasticity model using the realistic 3D phase-field geometries instead of idealized or homogenized RVE/SVEs. Building up on this computational tool, a micromechanics based crystal plasticity model was further refined to account for the natural and constrained lattice misfits. A new formulation for the isotropic hardening made the micro-mechanical model sensitive to

the lattice misfit using a sphere- and a penny-type Eshelby tensor for the $\gamma^{'}$ precipitates when it is cuboidal and rafted, respectively. At the microstructure level and for the monotonic tensile test, the model predicted:

- smaller strain hardening for microstructures with larger natural lattice misfits;
- smaller stress triaxiality for microstructures with larger natural lattice misfit and more pronounced rafted states.

The phase-field models were extended to understand the effect of crystallographic orientations on the macroscale performance of superalloys. The $[001]$, $[011]$, and $[111]$-oriented microstructures obtained by phase-field simulations (under aging and creep conditions) agreed well with the experimental characterizations. For the first time, a phase-field model also predicted the microstructures for small misorientations away from the main crystallographic directions. The 3D phase-field microstructures with realizations of various perfect orientations and misorientations, were exported as statistical volume elements (SVEs) into a finite-element (FE) crystal plasticity model for assessing their macroscale performance. These 3D phase-field simulations also enabled the possibility of estimating the channel-width evolution in different directions for various crystallographic-orientations. A 3D rafting model was developed and calibrated using phase-field simulations. The model was able to predict the γ channel evolutions during positive and negative creep. The model has predicted the evolution of channel widths for any crystallographic orientations using a crystallographic-oriented accumulated plastic strain vector. The model was implemented to perform 3D crystal plasticity finite-element simulations and gave promising results that can ultimately be coupled with lattice rotations.

In many high-temperature applications, the structural components experience prolonged exposure to thermomechanical loads and the multiaxial stress states resulting from the mode of loading or sharp geometrical changes, which ultimately causes local stress concentrations for damage to nucleate. In Chapter 6, high-temperature/low-stress creep experiments are performed to gauge the effect of stress triaxiality on the creep performance of single-crystal superalloys. Four notched

samples with different triaxialities were tested using the high-temperature creep bench. Notched specimens were tested at 1050°C for different stress levels (160 MPa, 180 MPa, 200 MPa, 230 MPa) to gauge the effect of stress triaxiality (T=1, 0.84, 0.5, and uniaxial) on the creep performance of the MC2 superalloy. The results from notched tests were compared with notch-free specimens. A significant notch-strengthening effect was observed for specimens with triaxiality 0.84 for all stress conditions investigated in this dissertation.

7.2 Future Research Directions: Computational Modeling Standpoint

1. Conventional creep models developed based on the uniaxial creep data, and corresponding crystal deformation mechanisms cannot be extended straightforwardly to account for multiaxial creep deformation. For modeling anisotropic creep behavior, both octahedral and cubic slip systems should be taken into consideration. Finite-Element crystal plasticity simulations can be performed better to understand the phenomenon of stress redistribution in notched specimens.

2. The developed creep-damage framework can be extended to account for tension/compression asymmetry as well as multi-axial and creep-fatigue loading conditions in order to understand microstructural evolutions in more realistic configurations.

3. Phase-fields models could also be extended to have plastic driving forces in their formulation. Phase-field Dislocation Dynamics models can be another extension of this work where the plastic driving forces for the microstructural evolution are directly coming from the dislocation activity within the material.

4. The effect of dendrites on the mechanical loading could also be studied using a lattice-misfit-dependent micromechanical approach allowing to better understand phenomena, such as size effect.

5. To study the growth of voids in porous viscoplastic single-crystal superalloys, an existing high-temperature DDD framework (with coupled dislocation glide and vacancy diffusion

assisted climb formulation) could be extended to incorporate strain hardening (known as 2.5D constitutive relations) and in a computational cell that can handle slip discontinuities in the form of embedded voids in the geometry. The 2.5D rules and the periodic boundary conditions in this framework are a promising way to capture the bulk three-dimensional response of the material.

7.3 Future Research Directions: Physics Perspectives

1. Post-mortem EBSD analysis can be carried out to gauge the effect of lattice rotations on creep damage in notched specimens.

2. The microstructural evolution and creep performance during non-isothermal multi-axial conditions could be studied to better understand the effect of notch and temperature surge on the performance of turbine blades made of single crystal superalloys.

REFERENCES

[1] R. Harikrishnan, J.-B. le Graverend, A creep-damage phase-field model: Predicting topological inversion in ni-based single crystal superalloys, Materials & Design 160 (2018) 405–416.

[2] J.-B. le Graverend, R. Harikrishnan, Finite-element crystal plasticity on phase-field microstructures: Predicting mechanical response variations in ni-based single-crystal superalloys, JOM 71 (8) (2019) 2600–2611.

[3] J.-B. le Graverend, R. Harikrishnan, A lattice-misfit-dependent micromechanical approach in ni-based single crystal superalloys, International Journal of Mechanical Sciences 195 (2021) 106229.

[4] J.-B. le Graverend, J. Cormier, F. Gallerneau, P. Villechaise, S. Kruch, J. Mendez, A microstructure-sensitive constitutive modeling of the inelastic behavior of single crystal nickel-based superalloys at very high temperature, International Journal of Plasticity 59 (2014) 55–83.

[5] J.-B. Le Graverend, Étude et modélisation des effets d'incursion à très haute température sur le comportement mécanique d'un superalliage monocristallin pour aubes de turbine, Ph.D. thesis (2013).

[6] M. Durand-Charre, The microstructure of superalloys, CRC press, 1998.

[7] R. C. Reed, The superalloys: fundamentals and applications, Cambridge university press, 2008.

[8] M. Nathal, J. Diaz, R. Miner, High temperature creep behavior of single crystal gammpraime and gamm laloys, MRS Online Proceedings Library Archive 133 (1988).

[9] J.-B. Le Graverend, A lattice-misfit-dependent damage model for non-linear damage accumulations under monotonous creep in single crystal superalloys, Metallurgical and Materials

Transactions A 49 (9) (2018) 4126–4133.

[10] Y. Wang, D. Banerjee, C. Su, A. Khachaturyan, Field kinetic model and computer simulation of precipitation of l1 2 ordered intermetallics from fcc solid solution, Acta materialia 46 (9) (1998) 2983–3001.

[11] F. R. Nabarro, Rafting in superalloys, Metallurgical and Materials transactions A 27 (3) (1996) 513–530.

[12] M. Nazmy, A. Epishin, T. Link, M. Staubli, A review of degradation in single crystal nickel based superalloys, Energy Materials 1 (4) (2006) 263–268.

[13] M. Kamaraj, Rafting in single crystal nickel-base superalloys—an overview, Sadhana 28 (1-2) (2003) 115–128.

[14] S. Hu, L. Chen, A phase-field model for evolving microstructures with strong elastic inhomogeneity, Acta materialia 49 (11) (2001) 1879–1890.

[15] H. Nishimori, A. Onuki, Pattern formation in phase-separating alloys with cubic symmetry, Physical Review B 42 (1) (1990) 980.

[16] M. Cottura, Y. Le Bouar, B. Appolaire, A. Finel, Role of elastic inhomogeneity in the development of cuboidal microstructures in ni-based superalloys, Acta Materialia 94 (2015) 15–25.

[17] P. Caron, O. Lavigne, Recent studies at onera on superalloys for single crystal turbine blades, AerospaceLab (3) (2011) p–1.

[18] R. Hashizume, A. Yoshinari, T. Kiyono, Y. Murata, M. Morinaga, Development of ni-based single crystal superalloys for power-generation gas turbines, Superalloys 2004 (2004) 53–62.

[19] J. Zhang, T. , Y. Koizumi, T. Kobayashi, H. Harada, Strengthening by γ/γ interfacial dislocation networks in tms-162—toward a fifth-generation single-crystal superalloy, Metallurgical and Materials Transactions A 35 (6) (2004) 1911–1914.

[20] M. Probst-Hein, A. Dlouhy, G. Eggeler, Dislocation interactions in γ-channels between γ-particles of superalloy single crystals, Materials Science and Engineering: A 319 (2001) 379–382.

[21] L. Carroll, Q. Feng, T. Pollock, Interfacial dislocation networks and creep in directional coarsened ru-containing nickel-base single-crystal superalloys, Metallurgical and Materials Transactions A 39 (6) (2008) 1290–1307.

[22] X. Tan, J. Liu, T. Jin, Z. Hu, H. Hong, B. Choi, I. Kim, C. Jo, Effect of ruthenium on high-temperature creep rupture life of a single crystal nickel-based superalloy, Materials Science and Engineering: A 528 (29) (2011) 8381–8388.

[23] A. Fredholm, J.-L. Strudel, High temperature creep mechanisms in single crystals of some high performance nickel base superalloys, in: High Temperature Alloys, Springer, 1987, pp. 9–18.

[24] A. Epishin, T. Link, U. Brückner, P. Portella, Kinetics of the topological inversion of the γ/γ-microstructure during creep of a nickel-based superalloy, Acta Materialia 49 (19) (2001) 4017–4023.

[25] P. Caron, C. Ramusat, F. Diologent, Influence of the γ fraction on the γ/γ topological inversion during high temperature creep of single crystal superalloys, Superalloys 2008 (2008) 159–167.

[26] D. MacLachlan, G. Gunturi, D. Knowles, Modelling the uniaxial creep anisotropy of nickel base single crystal superalloys cmsx-4 and rr2000 at 1023 k using a slip system based finite element approach, Computational materials science 25 (1) (2002) 129–141.

[27] D. W. MacLachlan, L. W. Wright, S. Gunturi, D. M. Knowles, Constitutive modelling of anisotropic creep deformation in single crystal blade alloys srr99 and cmsx-4, International Journal of Plasticity 17 (4) (2001) 441–467.

[28] N. Zhou, C. Shen, M. Mills, Y. Wang, Large-scale three-dimensional phase field simulation of γ-rafting and creep deformation, Philosophical Magazine 90 (1-4) (2010) 405–436.

[29] J. Goerler, I. Lopez-Galilea, L. M. Roncery, O. Shchyglo, W. Theisen, I. Steinbach, Topological phase inversion after long-term thermal exposure of nickel-base superalloys: Experiment and phase-field simulation, Acta Materialia 124 (2017) 151–158.

[30] M. Gururajan, T. Abinandanan, Phase inversion in two-phase solid systems driven by an elastic modulus mismatch, Philosophical Magazine 87 (33) (2007) 5279–5288.

[31] R. Rajasekharan, E. Petrov, Uncertainty and global sensitivity analysis of bladed disk statics with material anisotropy and root geometry variations, Engineering Reports (2019).

[32] R. Rajasekharan, E. Petrov, Analysis of deformation of mistuned bladed disks with friction and random crystal anisotropy orientation using gradient-based polynomial chaos expansion, Journal of Engineering for Gas Turbines and Power 141 (4) (2019) 041016.

[33] P. Caron, Y. Ohta, Y. Nakagawa, T. Khan, Superalloys 1988, The Minerals, Metals and Materials Society, Warrendale (1988) 215.

[34] T. Pollock, A. Argon, Directional coarsening in nickel-base single crystals with high volume fractions of coherent precipitates, Acta metallurgica et materialia 42 (6) (1994) 1859–1874.

[35] A. Gaubert, M. Jouiad, J. Cormier, Y. Le Bouar, J. Ghighi, Three-dimensional imaging and phase-field simulations of the microstructure evolution during creep tests of-oriented ni-based superalloys, Acta Materialia 84 (2015) 237–255.

[36] S. Yong, T. Sugui, Y. Huichen, S. Delong, L. Shuang, Microstructure evolution and its effect on creep behavior of single crystal ni-based superalloys with various orientations, Materials Science and Engineering: A 668 (2016) 243–254.

[37] V. Sass, M. Feller-Kniepmeier, Orientation dependence of dislocation structures and deformation mechanisms in creep deformed cmsx-4 single crystals, Materials Science and Engineering: A 245 (1) (1998) 19–28.

[38] R. Desmorat, A. Mattiello, J. Cormier, A tensorial thermodynamic framework to account for the γ'rafting in nickel-based single crystal superalloys, International Journal of Plasticity 95 (2017) 43–81.

[39] M. Huang, L. Zhuo, Z. Liu, X. Lu, Z. Shi, J. Li, J. Zhu, Misorientation related microstructure at the grain boundary in a nickel-based single crystal superalloy, Materials Science and Engineering: A 640 (2015) 394–401.

[40] J. Li, J. Zhao, S. Liu, M. Han, Effects of low angle boundaries on the mechanical properties of single crystal superalloy dd6, Superalloys (2008) 443–451.

[41] V. Sass, U. Glatzel, M. Feller-Kniepmeier, Anisotropic creep properties of the nickel-base superalloy cmsx-4, Acta materialia 44 (5) (1996) 1967–1977.

[42] J. Yu, J. Li, J. Zhao, M. Han, Z. Shi, S. Liu, H. Yuan, Orientation dependence of creep properties and deformation mechanism in dd6 single crystal superalloy at 760 c and 785 mpa, Materials Science and Engineering: A 560 (2013) 47–53.

[43] D. M. Shah, S. Vega, S. Woodard, A. D. Cetel, Primary creep in nickel-base superalloys, Superalloys (2004) 197–206.

[44] M. Segersäll, J. J. Moverare, D. Leidermark, K. Simonsson, Creep and stress relaxation anisotropy of a single-crystal superalloy, Metallurgical and Materials Transactions A 45 (5) (2014) 2532–2544.

[45] N. Matan, D. Cox, P. Carter, M. Rist, C. Rae, R. Reed, Creep of cmsx-4 superalloy single crystals: effects of misorientation and temperature, Acta materialia 47 (5) (1999) 1549–1563.

[46] D. Shah, D. Duhl, The effect of orientation, temperature and γ' size on the yield strength of a single crystal nickel base superalloy, in: M. Gell (Ed.), International Symposium on Superalloys, Champion, PA (USA), pp. 105–114.

[47] R. Miner, T. Gabb, J. Gayda, K. Hemker, Orientation and temperature dependence of some mechanical properties of the single-crystal nickel-base superalloy rené n4: Part iii. tension-compression anisotropy, Metallurgical Transactions A 17 (3) (1986) 507–512.

[48] R. Miner, R. Voigt, J. Gayda, T. Gabb, Orientation and temperature dependence of some mechanical properties of the nickel base single crystal alloy rené n4, part 1: Tensile behavior, Metallurgical Transactions A 17 (1986) 491.

[49] L. Wang, Y. Liu, J. Yu, Y. Xu, X. Sun, H. Guan, Z. Hu, Orientation and temperature dependence of yielding and deformation behavior of a nickel-base single crystal superalloy, Materials Science and Engineering: A 505 (1-2) (2009) 144–150.

[50] F. Heredia, D. Pope, The tension/compression flow asymmetry in a high ' volume fraction nickel base alloy, Acta Metallurgica 34 (2) (1986) 279 – 285.

[51] F. Heredia, D. Pope, The plastic flow of binary ni3al single crystals, Acta Metallurgica et Materialia 39 (8) (1991) 2027 – 2036.

[52] F. Hanriot, Comportement du superalliage monocristallin am1 sous sollicitations cycliques, Ph.D. thesis, Ecole Nationale Supérieure des Mines de Paris (France) (1993).

[53] J.-B. Le Graverend, F. Pettinari-Sturmel, J. Cormier, M. Hantcherli, P. Villechaise, J. Douin, Mechanical twinning in ni-based single crystal superalloys during multiaxial creep at 1050 c, Materials Science and Engineering: A 722 (2018) 76–87.

[54] A. Vattré, B. Fedelich, On the relationship between anisotropic yield strength and internal stresses in single crystal superalloys, Mechanics of Materials 43 (12) (2011) 930–951.

[55] R. Decker, J. Mihalisin, Coherency strains in gamma prime hardened nickel alloys, ASM TRANS QUART 62 (2) (1969) 481–489.

[56] J. Van Sluytman, T. Pollock, Optimal precipitate shapes in nickel-base γ–γ alloys, Acta Materialia 60 (4) (2012) 1771–1783.

[57] R. Ricks, A. Porter, R. Ecob, The growth of γ precipitates in nickel-base superalloys, Acta Metallurgica 31 (1) (1983) 43–53.

[58] J.-B. le Graverend, A lattice-misfit-dependent damage model for non-linear damage accumulations under monotonous creep in single crystal superalloys, Metallurgical and Materials Transactions A 1–8.

[59] U. Glatzel, M. Feller-Kniepmeier, Calculations of internal stresses in the γ/γ microstructure of a nickel-base superalloy with high volume fraction of γ-phase, Scripta metallurgica 23 (11) (1989) 1839–1844.

[60] L. D. Landau, On the theory of phase transitions. i., Zh. Eksp. Teor. Fiz. 11 (1937) 19.

[61] J. W. Cahn, J. E. Hilliard, Free energy of a nonuniform system. i. interfacial free energy, The Journal of chemical physics 28 (2) (1958) 258–267.

[62] S. M. Allen, J. W. Cahn, Ground state structures in ordered binary alloys with second neighbor interactions, Acta Metallurgica 20 (3) (1972) 423–433.

[63] A. Gaubert, Y. Le Bouar, A. Finel, Coupling phase field and viscoplasticity to study rafting in ni-based superalloys, Philosophical Magazine 90 (1-4) (2010) 375–404.

[64] G. Boussinot, Y. Le Bouar, A. Finel, Phase-field simulations with inhomogeneous elasticity: Comparison with an atomic-scale method and application to superalloys, Acta Materialia 58 (12) (2010) 4170–4181.

[65] I. Steinbach, F. Pezzolla, B. Nestler, M. Seeßelberg, R. Prieler, G. J. Schmitz, J. L. Rezende, A phase field concept for multiphase systems, Physica D: Nonlinear Phenomena 94 (3) (1996) 135–147.

[66] I. Steinbach, Phase-field models in materials science, Modelling and simulation in materials science and engineering 17 (7) (2009) 073001.

[67] I. Steinbach, Phase-field model for microstructure evolution at the mesoscopic scale, Annual Review of Materials Research 43 (2013) 89–107.

[68] S. B. Biner, Programming phase-field modeling, Programming Phase-Field Modeling, ISBN 978-3-319-41194-1. Springer International Publishing Switzerland, 2017 (2017).

[69] M. Tegeler, O. Shchyglo, R. D. Kamachali, A. Monas, I. Steinbach, G. Sutmann, Parallel multiphase field simulations with openphase, Computer Physics Communications 215 (2017) 173–187.

[70] I. Steinbach, O. Shchyglo, Phase-field modelling of microstructure evolution in solids: perspectives and challenges, Current opinion in solid state and materials science 15 (3) (2011) 87–92.

[71] J. W. Cahn, On spinodal decomposition, Acta metallurgica 9 (9) (1961) 795–801.

[72] R. Hill, Elastic properties of reinforced solids: some theoretical principles, Journal of the Mechanics and Physics of Solids 11 (5) (1963) 357–372.

[73] I. Steinbach, M. Apel, Multi phase field model for solid state transformation with elastic strain, Physica D: Nonlinear Phenomena 217 (2) (2006) 153–160.

[74] U. Kocks, The relation between polycrystal deformation and single-crystal deformation, Metallurgical and Materials Transactions B 1 (5) (1970) 1121–1143.

[75] J. Hutchinson, Elastic-plastic behaviour of polycrystalline metals and composites, Proceedings of the Royal Society of London. A. Mathematical and Physical Sciences 319 (1537) (1970) 247–272.

[76] R. J. Asaro, Micromechanics of crystals and polycrystals, Advances in applied mechanics 23 (1) (1983) 115.

[77] A. Pineau, A. A. Benzerga, T. Pardoen, Failure of metals i: Brittle and ductile fracture, Acta Materialia 107 (2016) 424–483.

[78] L. M. Kachanov, Time of the rupture process under creep conditions, izy akad, Nank SSR Otd Tech Nauk 8 (1958) 26–31.

[79] Y. Rabotnov, Creep rupture, 12 th int. congress of applied mechanics (1968).

[80] J.-L. Chaboche, Continuous damage mechanics—a tool to describe phenomena before crack initiation, Nuclear Engineering and Design 64 (2) (1981) 233–247.

[81] L. Kachanov, D. Krajcinovic, Introduction to continuum damage mechanics, Journal of Applied Mechanics 54 (1987) 481.

[82] J. Lemaitre, A course on damage mechanics, Springer Science & Business Media, 2012.

[83] J.-B. le Graverend, J. Adrien, J. Cormier, Ex-situ x-ray tomography characterization of porosity during high-temperature creep in a ni-based single-crystal superalloy: Toward understanding what is damage, Materials Science and Engineering: A 695 (2017) 367–378.

[84] J. Lemaitre, Evaluation of dissipation and damage in metals submitted to dynamic loading, Mechanical behavior of materials (1972) 540–549.

[85] J. Lemaitre, Coupled elasto-plasticity and damage constitutive equations, Computer methods in applied mechanics and engineering 51 (1-3) (1985) 31–49.

[86] L. Kachanov, Creep theory, Fizmatgiz, Moscow (1960).

[87] Y. Robotnov, Creep problems in structural mechanics (1969).

[88] M. Ashby, B. Dyson, Creep damage mechanics and micromechanisms, in: Fracture 84, Elsevier, 1984, pp. 3–30.

[89] Z. Zhu, H. Basoalto, N. Warnken, R. Reed, A model for the creep deformation behaviour of nickel-based single crystal superalloys, Acta Materialia 60 (12) (2012) 4888–4900.

[90] D. Hayhurst, Creep rupture under multi-axial states of stress, Journal of the Mechanics and Physics of Solids 20 (6) (1972) 381–382.

[91] J.-L. Chaboche, F. Gallerneau, An overview of the damage approach of durability modelling at elevated temperature, Fatigue & Fracture of Engineering Materials & Structures 24 (6) (2001) 405–418.

[92] J.-L. Chaboche, Description thermodinamique et phenomenologique de la viscoplasticite cyclique avec endommagement, Univ. Pierre et Marie Curie, 1978.

[93] J.-L. Chaboche, Une loi différentielle d'endommagement de fatigue avec cumulation non linéaire, Office Nationale d'Etudes et de Recherches Aérospatiales, 1974.

[94] M. Cottura, Y. Le Bouar, A. Finel, B. Appolaire, K. Ammar, S. Forest, A phase field model incorporating strain gradient viscoplasticity: application to rafting in ni-base superalloys, Journal of the Mechanics and Physics of Solids 60 (7) (2012) 1243–1256.

[95] J.-B. le Graverend, From continuum to quasi-continuum damage mechanics for fast evolving microstructures: Application to ni-based single crystal superalloys, Submitted to Mechanics of Materials.

[96] M. K. Rajendran, O. Shchyglo, I. Steinbach, Large scale 3-d phase-field simulation of coarsening in ni-base superalloys, in: MATEC Web of Conferences, Vol. 14, EDP Sciences, 2014, p. 11001.

[97] I. M. Lifshitz, V. V. Slyozov, The kinetics of precipitation from supersaturated solid solutions, Journal of physics and chemistry of solids 19 (1-2) (1961) 35–50.

[98] C. Wagner, Theory of precipitate change by redissolution, Z. Elektrochem. 65 (1961) 581–591.

[99] A. Ardell, R. Nicholson, The coarsening of γ'in ni-al alloys, Journal of Physics and Chemistry of Solids 27 (11-12) (1966) 1793–1794.

[100] D. Siebörger, H. Knake, U. Glatzel, Temperature dependence of the elastic moduli of the nickel-base superalloy cmsx-4 and its isolated phases, Materials Science and Engineering: A 298 (1) (2001) 26–33.

[101] L. Müller, T. Link, M. Feller-Kniepmeier, Temperature dependence of the thermal lattice mismatch in a single crystal nickel-base superalloy measured by neutron diffraction, Scripta metallurgica et materialia 26 (8) (1992) 1297–1302.

[102] M. Nathal, R. Mackay, R. Garlick, Temperature dependence of γ-γ'lattice mismatch in nickel-base superalloys, Materials Science and Engineering 75 (1-2) (1985) 195–205.

[103] S. Yoshitake, V. Narayan, H. Harada, H. Bhadeshia, D. Mackay, Estimation of the γ and γ'lattice parameters in nickel-base superalloys using neural network analysis, ISIJ international 38 (5) (1998) 495–502.

[104] J.-B. Le Graverend, L. Dirand, A. Jacques, J. Cormier, O. Ferry, T. Schenk, F. Gallerneau, S. Kruch, J. Mendez, In situ measurement of the γ/γ lattice mismatch evolution of a nickel-based single-crystal superalloy during non-isothermal very high-temperature creep experiments, Metallurgical and Materials Transactions A 43 (11) (2012) 3946–3951.

[105] J. Lemaitre, J.-L. Chaboche, Mechanics of solid materials, Cambridge university press, 1994.

[106] T. Murakumo, Y. Koizumi, K. Kobayashi, H. Harada, Creep strength of ni-base single-crystal superalloys on the γ/γ'tie-line, Superalloys (2004) 155–62.

[107] R. A. MacKay, L. J. Ebert, The development of γ-γ lamellar structures in a nickel-base superalloy during elevated temperature mechanical testing, Metallurgical Transactions A 16 (11) (1985) 1969–1982.

[108] M. Pessah, P. Caron, T. Khan, Effect of mu phase on the mechanical properties of a nickel-base single crystal superalloy, ONERA, TP (1992-153) (1992) 567–576.

[109] L. Espié, Etude expérimentale et modélisation numérique du comportement de monocristaux de superalliages (1996).

[110] A. Gaubert, Modélisation des effets de l'évolution microstructurale sur le comportement mécanique du superalliage monocristallin am1, Ph.D. thesis (2009).

[111] A. Srivastava, A. Needleman, Phenomenological modeling of the effect of specimen thickness on the creep response of ni-based superalloy single crystals, Acta materialia 61 (17) (2013) 6506–6516.

[112] K. Arora, K. Kishida, K. Tanaka, H. Inui, Effects of lattice misfit on plastic deformation behavior of single-crystalline micropillars of ni-based superalloys, Acta Materialia 138 (2017) 119–130.

[113] T. Pollock, A. Argon, Creep resistance of cmsx-3 nickel base superalloy single crystals, Acta Metallurgica et Materialia 40 (1) (1992) 1–30.

[114] L. Müller, U. Glatzel, M. Feller-Kniepmeier, Calculation of the internal stresses and strains in the microstructure of a single crystal nickel-base superalloy during creep, Acta metallurgica et materialia 41 (12) (1993) 3401–3411.

[115] T. Tinga, W. Brekelmans, M. Geers, Time-incremental creep–fatigue damage rule for single crystal ni-base superalloys, Materials Science and Engineering: A 508 (1-2) (2009) 200–208.

[116] R. Reed, D. Cox, C. Rae, Kinetics of rafting in a single crystal superalloy: effects of residual microsegregation, Materials Science and Technology 23 (8) (2007) 893–902.

[117] M. Cottura, B. Appolaire, A. Finel, Y. Le Bouar, Coupling the phase field method for diffusive transformations with dislocation density-based crystal plasticity: Application to ni-based superalloys, Journal of the Mechanics and Physics of Solids 94 (2016) 473–489.

[118] C. Wang, M. A. Ali, S. Gao, J. V. Goerler, I. Steinbach, Combined phase-field crystal plasticity simulation of p-and n-type rafting in co-based superalloys, Acta Materialia 175 (2019) 21–34.

[119] L. Dirand, A. Jacques, J. P. Chateau-Cornu, T. Schenk, O. Ferry, P. Bastie, Phase-specific high temperature creep behaviour of a pre-rafted ni-based superalloy studied by x-ray synchrotron diffraction, Philosophical Magazine 93 (10-12) (2013) 1384–1412.

[120] B. Fedelich, G. Künecke, A. Epishin, T. Link, P. Portella, Constitutive modelling of creep degradation due to rafting in single-crystalline ni-base superalloys, Materials Science and Engineering: A 510 (2009) 273–277.

[121] E. Wu, G. Sun, B. Chen, T. Pirling, D. J. Hughes, S. Wang, J. Zhang, A neutron diffraction study of lattice distortion, mismatch and misorientation in a single-crystal superalloy after different heat treatments, Acta materialia 61 (7) (2013) 2308–2319.

[122] S. Gao, M. Fivel, A. Ma, A. Hartmaier, Influence of misfit stresses on dislocation glide in single crystal superalloys: A three-dimensional discrete dislocation dynamics study, Journal of the Mechanics and Physics of Solids 76 (2015) 276–290.

[123] M. Brünig, O. Chyra, D. Albrecht, L. Driemeier, M. Alves, A ductile damage criterion at various stress triaxialities, International journal of plasticity 24 (10) (2008) 1731–1755.

[124] J. R. Rice, D. M. Tracey, On the ductile enlargement of voids in triaxial stress fields, Journal of the Mechanics and Physics of Solids 17 (3) (1969) 201–217.

[125] J.-Y. Chen, L.-M. Cao, M. Xue, L.-J. Liu, Microstructure and stress-rupture property of an experimental single crystal ni-base superalloy with different heat treatments, Rare Metals 33 (2) (2014) 144–148.

[126] C. Rae, M. Karunaratne, C. Small, R. Broomfield, C. Jones, R. Reed, Topologically close packed phases in an experimental rhenium-containing single crystal superalloy, Superalloys 2000 (2000) 767–776.

[127] T. Murakumo, T. Kobayashi, Y. Koizumi, H. Harada, Creep behaviour of Ni-base single-crystal superalloys with various γ' volume fraction, Acta Materialia 52 (12) (2004) 3737–3744.

[128] M. Ardakani, R. Ghosh, V. Brien, B. Shollock, M. McLean, Implications of dislocation micromechanisms for changes in orientation and shape of single crystal superalloys, Scripta materialia 39 (4-5) (1998) 465–472.

[129] X. Yang, P. Lee, N. D'Souza, Stray grain formation in the seed region of single-crystal turbine blades, JOM 57 (5) (2005) 40–44.

[130] A. Mattiello, Visco-plasticity and damage modeling of single crystal superalloys at high temperatures: a tensorial microstructure-sensitive approach, Ph.D. thesis, Paris Saclay (2018).

[131] Y. Li, L. Wang, G. Zhang, W. Zheng, D. Qi, K. Du, J. Zhang, L. Lou, Creep deformation related to γ phase cutting at high temperature of a [111] oriented nickel-base single crystal superalloy, Materials Science and Engineering: A 763 (2019) 138162.

[132] P. Poubanne, P. Caron, T. Khan, Characterization and modelling of the anisotropic mechanical behaviour of nickel-based single crystal superalloys for turbine blades, in: ICAS, Congress, 17 th, Stockholm, Sweden, 1990, pp. 1115–1121.

[133] P. Lukáš, J. Čadek, V. Šustek, L. Kunz, Creep of cmsx-4 single crystals of different orientations in tension and compression, Materials Science and Engineering: A 208 (2) (1996) 149 – 157.

[134] R. A. MacKay, R. D. Maier, The influence of orientation on the stress rupture properties of nickel-base superalloy single crystals, Metallurgical Transactions A 13 (10) (1982) 1747–1754.

[135] V. Sass, W. Schneider, H. Mughrabi, On the orientation dependence of the intermediate-temperature creep behaviour of a monocrystalline nickel-base superalloy, Scripta Metallurgica et Materialia 31 (7) (1994) 885 – 890.

[136] S. Zhang, D. Wang, J. Zhang, L. Lou, Orientation dependence of stress rupture properties of a ni-based single crystal superalloy at 760 c, Journal of Materials Science Technology 28 (3) (2012) 229 – 233.

[137] G. Han, J. Yu, Y. Sun, X. Sun, Z. Hu, Anisotropic stress rupture properties of the nickel-base single crystal superalloy srr99, Materials Science and Engineering: A 527 (21) (2010) 5383 – 5390.

[138] D. Chatterjee, N. Hazari, N. Das, R. Mitra, Microstructure and creep behavior of dms4-type nickel based superalloy single crystals with orientations near 001 and 011, Materials Science and Engineering: A 528 (2) (2010) 604 – 613.

[139] F. Gallerneau, Etude et modélisation de l'endommagement d'un superalliage monocristallin revêtu pour aube de turbine, Ph.D. thesis, Ecole National Superieur des Mines de Paris (1995).

[140] G. ming HAN, Y. hong YANG, J. jiang YU, X. feng SUN, Temperature dependence of anisotropic stress–rupture properties of nickel-based single crystal superalloy srr99, Transactions of Nonferrous Metals Society of China 21 (8) (2011) 1717 – 1721.

[141] G. I. Taylor, The distortion of crystals of aluminium under compression. part ii.—distortion by double slipping and changes in orientation of crystals axes during compression, Proceedings of the Royal Society of London. Series A, Containing Papers of a Mathematical and Physical Character 116 (773) (1927) 16–38.

[142] J. Ghighi, J. Cormier, E. Ostoja-Kuczynski, J. Mendez, G. Cailletaud, F. Azzouz, A microstructure sensitive approach for the prediction of the creep behaviour and life under complex loading paths, Technische Mechanik-European Journal of Engineering Mechanics 32 (2-5) (2012) 205–220.

[143] R. Ghosh, R. Curtis, M. McLean, Creep deformation of single crystal superalloys—modelling the crystallographic anisotropy, Acta Metallurgica et Materialia 38 (10) (1990) 1977 – 1992.

[144] M. Ardakani, R. Ghosh, V. Brien, B. Shollock, M. McLean, Implications of dislocation micromechanisms for changes in orientation and shape of single crystal superalloys, Scripta Materialia 39 (4) (1998) 465 – 472.

[145] K. Kakehi, Influence of secondary precipitates and crystallographic orientation on the strength of single crystals of a ni-based superalloy, Metallurgical and Materials Transactions A 30 (1999) 1249 – 1259.

[146] S. Gunturi, D. MacLachlan, D. Knowles, Anisotropic creep in cmsx-4 in orientations distant from <001>, Materials Science and Engineering: A 289 (1) (2000) 289 – 298.

[147] E. Alster, D. Montiel, K. Thornton, P. W. Voorhees, Simulating complex crystal structures using the phase-field crystal model, Physical Review Materials 1 (6) (2017) 060801.

[148] R. Indergand, A. Vidyasagar, N. Nadkarni, D. M. Kochmann, A phase-field approach to studying the temperature-dependent ferroelectric response of bulk polycrystalline pzt, Journal of the Mechanics and Physics of Solids (2020) 104098.

[149] B. Fedelich, A. Epishin, T. Link, H. Klingelhöffer, G. Künecke, P. D. Portella, Rafting during high temperature deformation in a single crystal superalloy: experiments and modeling, Superalloys 2012 (6) (2012) 491–500.

[150] G. Nolze, Euler angles and crystal symmetry, Crystal Research and Technology 50 (2) (2015) 188–201.

[151] H.-J. Bunge, Texture analysis in materials science: mathematical methods, Butterworths, 1982.

[152] T. Tinga, W. Brekelmans, M. Geers, Directional coarsening in nickel-base superalloys and its effect on the mechanical properties, Computational materials science 47 (2) (2009) 471–481.

[153] F. Diologent, P. Caron, T. d'Almeida, A. Jacques, P. Bastie, The γ/γ mismatch in ni based superalloys: In situ measurements during a creep test, Nuclear Instruments and Methods in Physics Research Section B: Beam Interactions with Materials and Atoms 200 (2003) 346–351.

[154] A. Jacques, F. Diologent, P. Bastie, In situ measurement of the lattice parameter mismatch of a nickel-base single-crystalline superalloy under variable stress, Materials Science and Engineering: A 387 (2004) 944–949.

[155] J. Coakley, D. Ma, M. Frost, D. Dye, D. N. Seidman, D. C. Dunand, H. J. Stone, Lattice strain evolution and load partitioning during creep of a ni-based superalloy single crystal with rafted γ microstructure, Acta Materialia 135 (2017) 77–87.

[156] J. Cormier, G. Cailletaud, Constitutive modeling of the creep behavior of single crystal superalloys under non-isothermal conditions inducing phase transformations, Materials Science and Engineering: A 527 (23) (2010) 6300–6312.

[157] M. Veron, Y. Brechet, F. Louchet, Strain induced directional coarsening in ni based superalloys, Scripta Materialia 34 (12) (1996).

[158] J.-B. Le Graverend, J. Cormier, M. Jouiad, F. Gallerneau, P. Paulmier, F. Hamon, Effect of fine γ precipitation on non-isothermal creep and creep-fatigue behaviour of nickel base superalloy mc2, Materials Science and Engineering: A 527 (20) (2010) 5295–5302.

[159] J.-B. Le Graverend, J. Cormier, F. Gallerneau, S. Kruch, J. Mendez, Strengthening behavior in non-isothermal monotonic and cyclic loading in a ni-based single crystal superalloy, International Journal of Fatigue 91 (2016) 257–263.

[160] D. Hayhurst, G. Webster, An overview on studies of stress state effects during creep of circumferentially notched bars, in: Techniques for multiaxial creep testing, Springer, 1986, pp. 137–175.

[161] P. Lukáš, P. Preclık, J. Čadek, Notch effects on creep behaviour of cmsx-4 superalloy single crystals, Materials Science and Engineering: A 298 (1-2) (2001) 84–89.

[162] H. Basoalto, R. Ghosh, M. Ardakani, B. Shollock, M. McLean, Multiaxial creep deformation of single crystal superalloys: modelling and validation, Superalloys 2000 (2000) 515–524.

[163] M. McLean, R. Ghosh, R. Curtis, U. Basu-Conlin, M. Winstone, Anisotropy of high temperature deformation of single crystal superalloys–constitutive law, modelling and validation, Superalloys 1992 (1992) 609–618.

[164] M. Ardakani, M. McLean, B. Shollock, Twin formation during creep in single crystals of nickel-based superalloys, Acta materialia 47 (9) (1999) 2593–2602.

[165] L. Cao, P. Thome, L. A. Jacome, C. Somsen, G. Cailletaud, G. Eggeler, On the influence of crystallography on creep of circular notched single crystal superalloy specimens, Materials Science and Engineering: A (2020) 139255.

[166] J.-B. Le Graverend, J. Cormier, S. Kruch, F. Gallerneau, J. Mendez, Microstructural parameters controlling high-temperature creep life of the nickel-base single-crystal superalloy mc2, Metallurgical and Materials Transactions A 43 (11) (2012) 3988–3997.

[167] C. Law, M. Blackburn, Notch-rupturf behavior of a nickel-base superalloy at intermediate temperatures, Superalloys 1980 (1980).

[168] D. Hayhurst, F. Leckie, C. Morrison, Creep rupture of notched bars, Proceedings of the Royal Society of London. A. Mathematical and Physical Sciences 360 (1701) (1978) 243–264.